THE UNIVERSITY OF CHICAGO

MEASUREMENT OF THE DALITZ PARAMETERS IN

$K_L \to \pi^+\pi^-\pi^0$ DECAYS.

A DISSERTATION SUBMITTED TO

THE FACULTY OF THE DIVISION OF THE PHYSICAL SCIENCES

IN CANDIDACY FOR THE DEGREE OF

DOCTOR OF PHILOSOPHY

DEPARTMENT OF PHYSICS

BY

MIGUEL A. BARRIO

CHICAGO, ILLINOIS

DECEMBER 2001

To Jeff, my family, and all my friends.

TABLE OF CONTENTS

LIST OF FIGURES

LIST OF TABLES

ABSTRACT

We measured the Dalitz parameters for the $K_L \to \pi^+\pi^-\pi^0$ decay using data from the KTeV 1997 run. We obtained the following values for the Dalitz parameters: $g = 0.7065 \pm 0.0077$, $h = 0.096 \pm 0.013$, and $k = 0.0216 \pm 0.0026$. The fit to the CP violating parameters j and f gave results that are consistent with zero. We also measured the radiative branching ratio $Br(K_L \to \pi^+\pi^-\pi^0\gamma \, , E_\gamma > 10 \ MeV) = (1.66 \pm 0.05) \times 10^{-4})$, which is in good agreement with theoretical predictions.

CHAPTER 1
INTRODUCTION

The study of neutral kaon decays into hadrons has been a constant subject of interest over the years. In the 1950's Pais, Gell-Mann [1] and others first speculated about kaons and the possibility that symmetry breaking weak interactions would allow particle and anti-particle to mix. In 1960, Weinberg [2] speculated about the possibility of testing the $\Delta I = 1/2$ isospin rule using $K^+ \to 3\pi$ decays. In 1963, Luers et al. [3] observed kaon decays to three pions for the first time. Since then, many measurements involving neutral kaons decaying to three-pion states have been performed.

The KTeV detector was designed to measure direct CP violation in kaon decays. This involves collecting large numbers of $\pi^+\pi^-$ and $\pi^0\pi^0$ kaon decay events. One of the detector's main attributes is its ability to reconstruct charged and neutral decay products with high precision. A large number of other kaon decay modes was also collected for calibration and cross-checks. After all selection cuts, our data sample has 1.6 million $K_L \to \pi^+\pi^-\pi^0$ events, more than three times that of the previous measurement. It is natural to use this sample to measure the $\pi^+\pi^-\pi^0$ cross-section parameters.

1.1   The Dalitz Parameters

The *Dalitz distribution* describes the probability of a final state momentum configuration in the K_L to $\pi^+\pi^-\pi^0$ decay; the *Dalitz parameters* are the coefficients of this distribution. There are three particles in the final state in the $K_L \to \pi^+\pi^-\pi^0$ decay. Since we have 4-momentum conservation and rotational symmetry constraints, the number of independent degrees of freedom is just two. The natural variables for describing the cross-section of a three particle decay are the momentum transfers in the center of mass frame

$$S_i = (P_K - P_i)^2 \quad (i = 1, 2, 3 \quad for \ \ \pi^+, \pi^-, \pi^0) \tag{1.1}$$

These are not independent, however, since their sum is

$$S_0 = \tfrac{1}{3}\sum_i S_i = \tfrac{1}{3}(m_K^2 + 2m_{\pi^+}^2 + m_{\pi^0}^2) \tag{1.2}$$

The Dalitz probability distribution is usually parametrized in terms of two independent Lorentz-invariant quantities X and Y , defined in terms of S_i and S_0 by

$$X = \frac{S_2 - S_1}{m_{\pi^+}^2} \ , \qquad\qquad Y = \frac{S_3 - S_0}{m_{\pi^+}^2} \ . \qquad\qquad (1.3)$$

In the center of mass frame, the variable X is proportional to the difference of kinetic energy between the charged pions. The variable Y is proportional to the square of the momentum of the neutral pion, and since we have momentum conservation, this means it is also proportional to the square of the invariant mass of the charged pion system. We can expand the Dalitz probability distribution in terms of X and Y as

$$|\mathcal{M}|^2 = 1 + gY + hY^2 + jX + kX^2 + fXY + ... \qquad\qquad (1.4)$$

This is the customary definition of the Dalitz parameters g, h, j, k, and f. Higher order terms are dropped in this expansion because they are considered to be small. In practice, h is roughly an order of magnitude smaller than g, and k is about an order of magnitude smaller than the h. A theoretical calculation of these parameters is extremely difficult, as strong interactions are involved. However, it is possible to derive relations between the cross-sections for different decay modes using Chiral Perturbation Theory.

1.2   Isospin Symmetries

The $\pi^+\pi^-\pi^0$ final state, as any pion state, can be decomposed into a superposition of states with definite total isospin I. Since the pion is an isospin triplet, the total isospin of the final 3π state can have a value between 0 and 3, and it is possible to construct properly symmetrized final states with definite isospin [4]. The result of this is that the Dalitz parameters for the three-pion decay amplitudes

$$\begin{aligned}
K^+ &\to \pi^+\pi^+\pi^- \\
K^+ &\to \pi^+\pi^0\pi^0 \\
K_L &\to \pi^+\pi^-\pi^0 \\
K_L &\to \pi^0\pi^0\pi^0
\end{aligned} \qquad\qquad (1.5)$$

can be related [5] [6]. In particular, it is possible to relate the Dalitz parameters for $K_L \to \pi^+\pi^-\pi^0$ and $K_L \to \pi^0\pi^0\pi^0$ decays. If we describe the Dalitz distribution for $K_L \to 3\pi$ decays by an equation of the form

$$|\mathcal{M}|^2 = 1 + aY + bY^2 + cX^2, \qquad\qquad (1.6)$$

where parameters for odd powers of X, which are CP violating, have been neglected. If some assumptions are made regarding certain final state strong interaction phases [5], then the quantity R, defined in terms of the parameters in Equation 1.6 by

$$R \equiv b + 3c - \frac{a^2}{4cos^2\beta}, \qquad\qquad (1.7)$$

is the same for both decay modes. Here a, b, and c are generic coefficients for each term in the X, Y variable expansion of the Dalitz function, and β is a final state strong interaction phase. In the case of the $\pi^+\pi^-\pi^0$ final state, Equation 1.7 becomes

$$R_{+-0} = h + 3k - \frac{g^2}{4cos^2\beta}. \tag{1.8}$$

Since the form of the Dalitz function for the $K_L \to \pi^0\pi^0\pi^0$ decay is

$$|\mathcal{M}|^2 = 1 + h_{000}\left(Y^2 + \frac{1}{3}X^2\right), \tag{1.9}$$

for these decays Equation 1.7 takes the form

$$R_{000} = 2h_{000}. \tag{1.10}$$

Isospin symmetry then tells us that $R_{+-0} = R_{000}$, or equivalently

$$h + 3k - \frac{g^2}{4cos^2\beta} = 2h_{000}. \tag{1.11}$$

Previous attempts at studying this relation [5] have assumed the strong interaction phase β to be zero, and the experimental values available at the time had confirmed this, within experimental error [5].

There is more to the strong interaction phases than the simple expression in Equation 1.7. Chiral Perturbation Theory has considered these decays, and some predictions have been made regarding the relationships between different decay modes. In particular, radiative effects play an important role here. It is not clear to us if the predicted quantities can be used to derive a prediction for $cos^2\beta$. This is ultimately something for the theorists to study. The work by D'Ambrosio et al. [6] points out that experimental results are needed if we are to compare the $K \to 3\pi$ strong phases predicted by Chiral Perturbation Theory with measured quantities.

1.2.1 Radiative contributions

Since we have a very clean $\pi^+\pi^-\pi^0$ sample, we decided to measure the relative branching ratio

$$Br(K_L \to \pi^+\pi^-\pi^0\gamma\,) = \frac{\Gamma(\pi^+\pi^-\pi^0\gamma\,)}{\Gamma(\pi^+\pi^-\pi^0\,)}. \tag{1.12}$$

This is an interesting measurement in itself, as it had never been experimentally observed. Using Chiral Perturbation Theory, higher order corrections to the QED contributions to this decay have been predicted [7]. Our measurement agrees quite well with the predicted values.

Corrections due to photon emission by the charged particles plays an important role in the measurement of the Dalitz parameters as well. This has been treated extensively in the literature [5]. The emission of a photon changes the available energy that the charged pions carry, thus changing their momentum distribution. This affects the Dalitz distribution, in particular the Y variable, which is proportional to the charged invariant mass of the $\pi^+\pi^-$ system. Our study of the radiative cross-section has made it possible to understand the radiative contributions in great detail, and to incorporate them in the Monte Carlo simulation. For this reason, we do not need to make a theory-based correction to our measured values.

1.3   Previous Measurements

Many experiments have tried to measure the Dalitz parameters, with varying degrees of success. As previously mentioned, the first experiment, by Lues et al. [3] used only 77 events, and could only measure the relative branching ratio of $\pi^+\pi^-\pi^0$ events to all K_L decays. Twenty of these experiments did not have enough data to do a full Dalitz plot fit, preventing their results from being used for averages (PDG-2000 [8], page 519). The four measurements used in the PDG-2000 average are the ones by Y. Cho et al. [9], R. Messner et al. [10], K.J. Peach et al. [11], and Angelopoulos et al. [12] (CPLEAR collaboration). It is important to point out that *none* of these experiments, except CPLEAR, were able to reconstruct the π^0 in the decay. Kinematic constraints where used instead. Reconstructing the π^0 allows us to eliminate a great deal of background and to better constrain the kinematics.

The result with the most statistics is the one by Angelopoulos et al., from the CPLEAR collaboration, with 500K events. Our final sample has 1.6 million events. However, a better measurement is contingent on the understanding our detector acceptance in great detail.

1.4   Motivation for this Experiment

The measurement of the Dalitz parameters allows us to probe the underlying relationships between various kaon decay modes into three pions. The KTeV detector is a very good tool for the study of kaon decays, and it has collected the largest sample of $K_L \to \pi^+\pi^-\pi^0$ decays to date. It is natural to use this sample to measure the $\pi^+\pi^-\pi^0$ Dalitz parameters. Additionally, KTeV can also measure the $K_L \to \pi^0\pi^0\pi^0$ decay mode. These two results could provide more information for the theoretical study of kaon physics [6]. Finally, the study of this sample has made it possible to measure the $\pi^+\pi^-\pi^0\gamma$ radiative form factors and branching ratio, which had not been observed previously. The understanding of this effect feeds back into the Dalitz measurement itself, resulting in a very interesting interplay of measurements.

1.5   Outline

In this thesis, we will first give a detailed description of the KTeV detector. In particular, we will concentrate on the two detector components most important to us: the charged tracking system, which tracks charged particles through the detector, and the Cesium-Iodide calorimeter, which measures the energy deposited by photons and other particles. We will then briefly describe data collection and handling. Sample selection will be discussed next, followed by the analysis cuts applied. A more detailed description of specific topics follows. We discuss the "Minimum Ionizing Particle" (MIP) energy cut, applied to charged pion clusters to reduce the probability of big hadronic showers in the calorimeter. In $\pi^+\pi^-\pi^0$ events it is possible to impose mass constraints to improve the reconstruction of the event. We will discuss how these are applied and the resulting improvement in resolution. We will also describe the measurement of the radiative cross-section of the $K_L \to \pi^+\pi^-\pi^0\gamma$ decay, and how this feeds back into the Dalitz analysis itself. The Dalitz parameter fitting comes next, followed by a discussion of the systematic uncertainties. Finally, we will draw conclusions from our measurement.

Hope you enjoy it!

CHAPTER 2
THE KTEV APPARATUS

The KTeV beamline and detector are formed by many complex systems. In this chapter we will describe these systems in some detail, concentrating on those systems that play an important role in our measurement.

2.1   The Beamline

The KTeV experiment utilizes a well defined and clean kaon beam. A lot of work went into designing the beamline to accomplish this [13, 14]. An 800 GeV proton beam is extracted from the Tevatron and steered to the KTeV target station. The Tevatron operates in one-minute cycles. It takes about 40 seconds to inject and accelerate protons in the main ring, followed by a 20 second long extraction of these high-energy protons, customarily referred to as the "spill". The spill is formed by "buckets" of protons, which are about 18.9 ns apart, and are less than 1 ns wide. This results in bursts of protons with a frequency of about 53 MHz.

The KTeV target is a narrow rod of Beryllium-Oxide, 3 mm wide and 30 cm in length (which is about 1.1 interaction lengths). The RMS size of the proton illumination on the target is about 250 μm in both the horizontal and vertical dimensions. The beam positioning is kept steady throughout the run using an *Autotune* program [15]. The proton beam and target are tilted at a downward angle of 4.8 mrad, relative to the downstream direction defined by the collimation system and the KTeV detector. This is done to increase the ratio of kaons to neutrons in the resulting beam.

All charged particles, including all residual protons from the beam, are swept away by magnets and dumped into copper and steel blocks. Special care is needed to sweep away muons, since some are negatively charged and bend in the opposite direction compared to protons. For this purpose, additional iron blocks were used, effectively preventing these muons from reaching the KTeV detector.

After sweeping away charged particles, the beam contains mostly photons and neutrons. The KTeV design requires two beams. These beams are defined by the collimation system shown in Figure 2.1. The first step is to tune the type and amount of particles in the beam. For this purpose, two "common absorbers" are placed in the beam path. The first one consists of 20 inches of Beryllium, which attenuates neutrons more than kaons due to the difference in their interaction cross-sections. The second one consists of 3 inches of lead, and converts photons and

absorbs the resulting electromagnetic showers. An additional "moveable absorber", an 18 inches long slab of Beryllium, is placed in the regenerator beam, and reduces the flux considerably. This is done to reduce the amount of hadronic interactions in the regenerator.

Beam collimation is the next step required to get a well-defined kaon beam. Two beams are used in the KTeV detector, one as a source of long-lived K_L , and the other as a source for the regenerator, which has the effect of producing the short-lived K_S . It was designed to produce beams with a sharply defined profile and minimum "halo" from scattered kaons. The "primary collimator", located 20 m downstream of the target, serves to reduce the particle flux on the "defining collimator", which is situated 85 m downstream of the target and determines the final beam shape. Both these collimator apertures are square, with a taper to reduce particle scattering off of the inner surfaces. To further reduce the probability of scattered particles getting past the collimation system, a "slab collimator" is placed 40 m downstream of the target to prevent scattered particles from crossing over from one aperture to the other. A magnet situated after the defining collimator sweeps away any remaining charged particles. The beams are transported in vacuum starting at about 28 m downstream of the target.

After the collimation and regeneration system, the beams consist mostly of K_L and neutrons. The vacuum beam *kaon-to-neutron* ratio is about 0.8, and the regenerator ratio is about 1.3. At high energy, a significant K_S component survives in the regenerator beam.

2.2   The Regenerator

The regenerator is the means by which K_S are produced in the KTeV detector. Although these do not contribute significantly to three pion final states, we will give a brief description of it because we will mention it in the discussion of possible background sources.

The K_0 and $\overline{K}_0$ states have different quark content [1], so they interact differently with matter. As a result of this, an initial K_L state, which is a precise mixture of K_0 and $\overline{K}_0$, will be changed in the interaction with matter, acquiring a certain K_S component. This process is called "regeneration", and it is the means by which the KTeV experiment obtains K_S . If the kaon undergoes only elastic interactions with the material, it will emerge in a coherent state of the form K_L $+ \rho K_S$, where ρ is a well defined regeneration parameter. Since the lifetime of the K_S component is three orders of magnitude smaller than the one for K_L , most of these states will decay as if they were a K_S state, with some interference due to the fact that it is a coherent state.

---

[1]see Appendix A
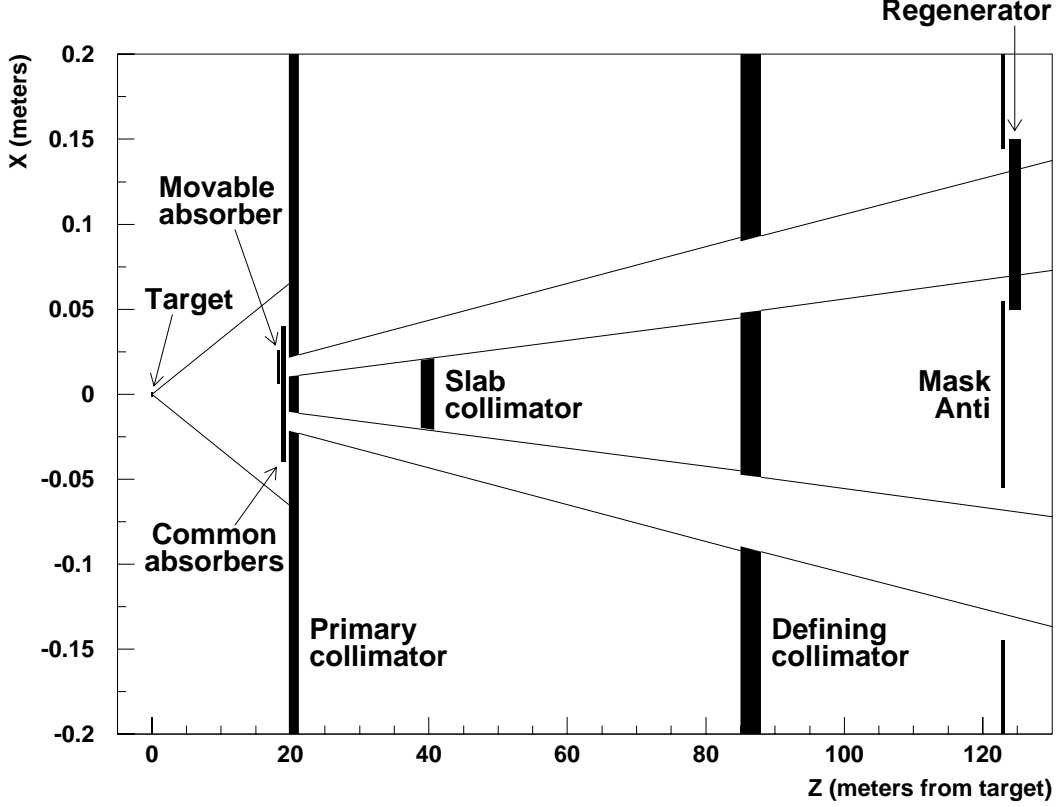
Figure 2.1: KTeV beam collimation system diagram.

The KTeV regenerator is made of blocks of plastic scintillator, with photomultiplier tubes attached to them. Figure 2.2 shows the KTeV detector, the regenerator being at the beginning on the decay region, right after the mask-anti. Most of the time, the kaon undergoes inelastic interactions on its way through the regenerator, and the emerging state is nearly pure K_S rather than the coherent state described above. Moreover, the outgoing kaon is likely to have a big transverse momentum. The photomultiplier tubes attached to the scintillators allow us to tag these events.

As already mentioned, only K_L contributes significantly to the $\pi^+\pi^-\pi^0$ decay [2]. For this reason, we will only consider events coming from the vacuum beam in the measurement of the Dalitz parameters. It is important that no kaons from the regenerator cross over and "look" like events coming from the vacuum beam. The regenerator veto helps in eliminating these events.

It is also important to mention that the regenerator alternates its position for each spill, averaging out any acceptance biases due to the asymmetries.

---

[2]see Appendix A

MUON FILTERS

MUON COUNTERS

LEAD WALL

CsI CRYSTAL CALORIMETER

HODOSCOPES

DRIFT CHAMBER 4

BACK-ANTI

HADRON-ANTI

DRIFT CHAMBER 3

MAGNET

TRD'S (E799)

DRIFT CHAMBER 2

DRIFT CHAMBER 1

SPECTROMETER ANTI

HELIUM BAG

RING VETOS

5m

10m

0

5m

KTeV

REGENERATOR (E832)

MASK-ANTI (E832)

BEAMS
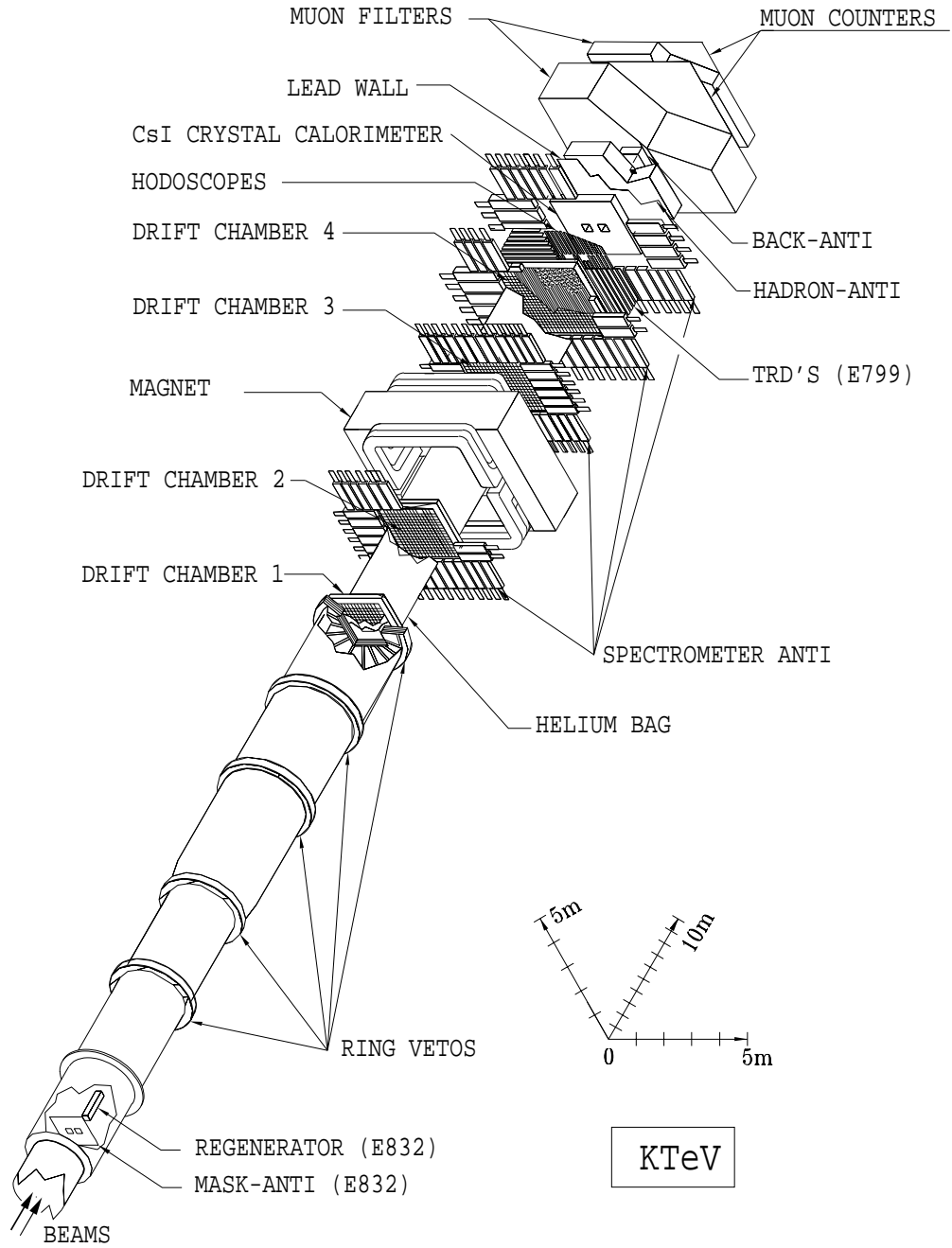
Figure 2.2: KTeV detector diagram.

2.3 The Drift Chambers

KTeV uses a set of four drift chambers for tracking charged particles. Two of these are upstream of the analysis magnet, while the other two are downstream, allowing for the measurement of the bend angle of charged particles as they pass through the magnet. Each of the chambers has two vertical and two horizontal planes of sense wires to measure the position of a passing charged particle. Surrounding the sense wires we have a set of field wires that provide the electric field required to attract the charged products left by the passing track onto the sense wire. Figure 2.3 shows the configuration of any one of the *views* of the drift chambers. There are two important reasons for using two planes of wires. Most particle tracks leave a single signal in each of these planes, i.e. produce "one hit" in each plane. If we had only one plane of wires, it would not be possible to determine which side of the wire the particle went through. Additionally, since we measure the time it takes for the ionized particles to reach the sense wires, we can select good hits from accidental hits by measuring the sum of drift distances to the wires, which should be the cell spacing, 6.35 cm. In the cases where a hit is missing, the ambiguity regarding which side of the wire a hit came from has to be resolved using information from the other drift chambers.

The drift chambers were operated with a 50%-50% mixture of argon and ethane, bubbled through isopropyl alcohol. The drift voltages were set to -2450 V or -2500 V, determined by a compromise between high efficiency and high current draw. Under these conditions, the drift speed is nearly constant over most of the drift cell and is about 50 μm/ns. The electrical pulse on the sense wire is amplified in two stages and discriminated, and the drift time is measured by a multi-hit TDC with a precision of 0.5 ns.

The calibration of the drift chamber system involves various steps. First is the calibration of the position resolution of a track in a given cell. This is done in two steps

- Shift each sense wire timing to a common T_0 reference time, add all time distributions,

- Calculate the *distance vs. drift-time* relation by integration of the time distribution.

The second step assumes a constant illumination across the cell, which is a very good approximation. This process is iterated to compensate for inefficiency differences at different distances from the sense wire. The resulting position resolution is about 100 μm. This resolution is derived from the "Sum of Distances" (SOD) distribution for tracks. A track passing through the drift chamber leaves signals in two neighboring cells, as shown in Figure 2.3. If we calculate the sum of the distances to the
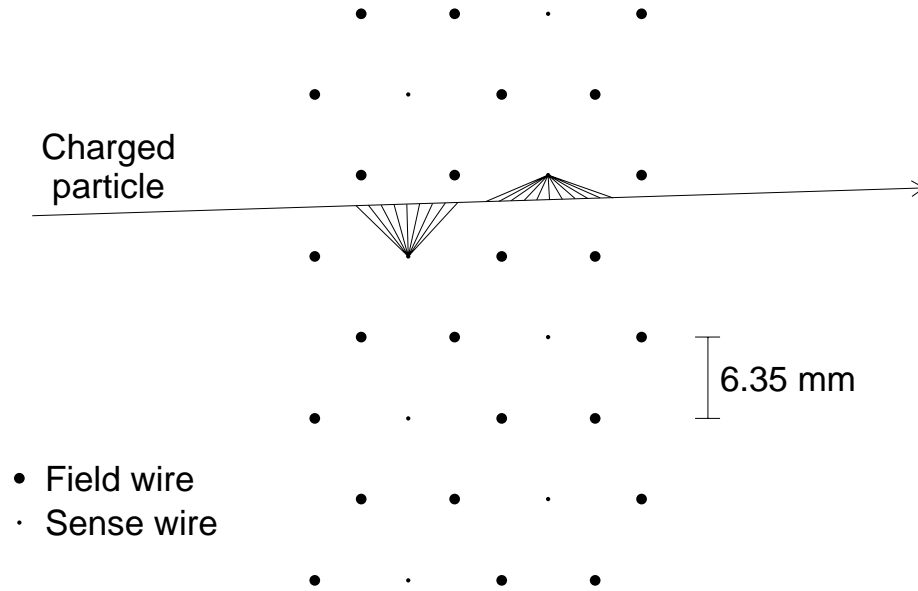
Figure 2.3: Drift chamber wire configuration. Shown here are the sense and field wires in one of the views of a drift chamber. There is one vertical and one horizontal view for each one of the chambers. Notice the design has no redundancy built in.

sense wires, we should get exactly *half* the cell separation[3]. The sense wire position resolution is $\sqrt{2}$ times smaller than this because the width of the SOD distribution is the resolution of the sum of two wire distances [4].

After all the data has been collected, we proceeded to the calibration of the relative and absolute positions of the drift chamber system. The Z positions come from survey measurements, as they cannot be determined from data. These are good to within a few millimeters. For all other positions we use muon runs with no magnetic field in the spectrometer magnet. The process involves various steps

- Fix the X, Y positions and rotations of DC1 and DC4 to the most recent values available (surveys or previous runs), and determine the X, Y positions and rotations of DC2 and DC3

---

[3]The X view of upstream chambers have wider SOD distributions because tracks are bent in the magnet and have a bigger incident angles.

[4]For tracks very close to one of the sense wires, the hit timing can be delayed further, resulting in worse resolution than the average resolution given by the total SOD distribution.

- Calculate a possible residual *corkscrew* rotation from an inaccurate value for the rotation of DC4.

This results in a positioning accuracy of about 20 μm for X and Y, and rotations good within about 50 μrad.

2.4 Analysis Magnet

The analysis magnet, together with the drift chambers, forms the charged particle spectrometer. It is operated at a current of about 1600 A, which imparts a total horizontal *momentum kick* of about 0.4 GeV/c to charged particles passing through it [5]. The magnet's field was mapped using a "zip track" system, and was found to be uniform to better than 0.25% over most of the region of interest, as expected from the design. Corrections to track momentum measured by the spectrometer are applied based on this field map. Additionally there is a "fringe field" produced by the magnet, which extends past DC2 and DC3 (the drift chambers upstream and downstream of the magnet, respectively). This produces a small track bending, which is corrected using measured data.

The "kick" provided by the spectrometer magnet is calibrated using $K_L \rightarrow \pi^+\pi^-$ events, since the invariant mass of these events is the kaon mass. An extra position correction is applied, based on measurements of the field variations across the kick plane of the magnet.

2.5 Calorimeter

The calorimeter constitutes one of the most important pieces of the KTeV detector, both for it's quality and cost.

Pure "Cesium-Iodide" (CsI) has two scintillation components, one "fast" (decay time $\sim$25 ns, peak wavelength $\sim$305 nm) and one "slow" (decay time $\sim$1 μ s, peak wavelength $\sim$480 nm). The fast component has sufficient light output that, at KTeV energies, the resolution term from photostatistics is acceptably small. Studies of radiation damage in small CsI pieces suggest that it could be made sufficiently radiation hard, although this had not been shown for large pieces. However, CsI also has some properties which make handling inconvenient: it is fairly soft, which makes polishing difficult and makes the crystals susceptible to scratches and bending, and it is somewhat hygroscopic, requiring a dry environment for storage and handling.

There are a total of 3100 pure CsI blocks in two cross-section sizes: 2.5 cm$\times$2.5 cm in the central region (where position resolution and the ability to distinguish two

---

[5]The "momentum kick" is defined as the total momentum change of a particle as it traverse the entire magnetic field region of the spectrometer. The change in momentum is independent of the particle's mass and momentum.

close photons is more important) and 5 cm×5 cm in the outer region. Figure 2.4 shows a representation of the CsI calorimeter face. All of the blocks are 50 cm long (27 radiation lengths) so that the electromagnetic shower from a high-energy photon or electron is almost fully contained, minimizing the resolution term from fluctuations in the amount of energy lost out the back of the CsI array. Two 15 cm×15 cm square beam holes (supported by square carbon-fiber tubes) allow passage of the neutral beams through the calorimeter.

Each crystal is wrapped in 13 μm thick mylar, part of which is aluminized. By choosing where we put the reflective mylar, we can tune the light collection to be uniform to within 5%, as determined using an automated test setup which measured the light output of the crystals, as produced by a Cs-137 source moved to ten places along their length. Finally, a plastic flange with magnetic shielding material is glued to the end of the crystal. This flange will hold the photomultiplier tube that will collect the scintillation light.

Cesium-Iodide is much more resistant to radiation damage as compared to the lead glass used in previous experiments, such as E731. Radiation damage tests were conducted on these crystals, and it was determined that the uniformity along the crystal is affected by the radiation damage. This behavior varied considerably from crystal to crystal.

The calorimeter was assembled in a sealed metal enclosure, "the blockhouse," in the KTeV hall. Size considerations were taken into account when assigning crystal positions in the calorimeter, so that sizes and surfaces matched as well as possible. The blockhouse has its own dehumidifying and air conditioning systems to protect the crystals and to cool the electronics. Vertical "ribs", just downstream of the crystals, support the readout electronics and convey power, digital and analog signals, and optical fibers. The front of the blockhouse has a "window" of several layers of aluminized mylar to allow particles to enter through minimal material while keeping the interior dark.

The scintillation light from each CsI block is collected by a photomultiplier tube (PMT) coupled to the crystal with a soft silicone "cookie" and a disk of Schott UG-11 filter glass, which blocks a significant fraction of the slow-component scintillation light. The PMTs were custom-designed for KTeV to meet the stringent specification on linearity at the rather low gain required by KTeV. For many crystals, we used a cookie with an embedded black annular "mask" to reduce the amount of light seen by the PMT, so that we can operate the PMT at a higher gain where the linearity is better.

The CsI signal is read out by a novel "digital photomultiplier tube" (DPMT) device [16], in which the PMT anode is connected by a very short cable to a circuit which digitizes the signal, buffers the digitized value, and transmits it on demand. The heart of the device is an ASIC (Application Specific Integrated Circuit) developed at Fermilab, the QIE (for "charge integrator and encoder"), which divides the input signal into several ranges (with 1/2, 1/4, 1/8, ... of the input signal),
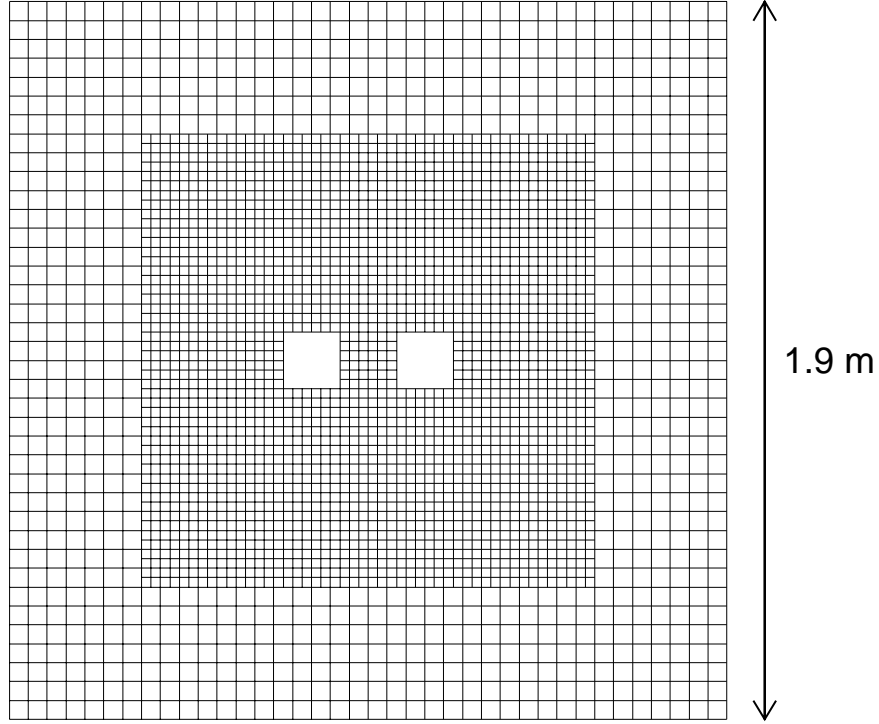
Figure 2.4: Cesium-Iodide calorimeter crystal arrangement. Notice the small crystals in the inner portion of the calorimeter, and the big outer ones, and also the beamholes, which have been left open to prevent hadronic interactions with the leftover beam.

accumulates PMT charge on capacitors over a given time interval ("slice"), selects the range for which the voltage on the capacitors lie within a certain window, and outputs that voltage to be digitized by a separate flash ADC chip. The range selected is indicated by a binary "exponent" code, which is recorded with the digital "mantissa" from the flash ADC. Each range uses four capacitors in a rotating sequence, so that the device continuously produces outputs for each time slice. A second ASIC, the DBC (for "driver, buffer, clock"), contains a FIFO to store the digitized information from the QIE and flash ADC on each clock cycle, and transfers the data for several consecutive time slices to a "pipeline" module when an event is accepted by the trigger. Thus, this device provides a wide dynamic range with very low noise (pedestal width ~ 0.5 MeV) and with pulse shape information.

The multitude of DPMT ranges and capacitors makes calibration rather complex. Cross-calibration is done using a laser calibration system which distributes shaped

pulses of UV light (produced in a dye by the primary laser pulse) to each crystal along a quartz fiber connected to a hole in the flange; the light intensity is scanned up and down over the full dynamic range, and referenced to PiN photodiodes with excellent intrinsic linearity. This system is also useful for monitoring short-term drifts in the PMT gains during normal running.

The channel gains are then calibrated using electrons, by matching the energy measured by the calorimeter to the momentum measured by the spectrometer, in an iterative procedure. Figure 2.5 shows the ratio of the calorimeter energy to the track momentum ("E/p") for these electrons after all calorimeter corrections. The width of the distribution is the result of both the calorimeter and the momentum resolution. Figure 2.6 shows the calorimeter resolution after subtracting the track momentum resolution from the width of the E/p distribution. The track momentum resolution is estimated from the mismatch of tracks at the magnet's kick plane (which is a measure of the error in the determination of the difference of the slopes of charged tracks). Figure 2.7 shows the π^0 mass distribution from $K_L \to \pi^+\pi^-\pi^0$ events. The mass of a π^0, calculated from the positions and energies of the photons reconstructed in the calorimeter, is

$$m(\gamma\gamma) \approx r/z\sqrt{E_1 E_2} \tag{2.1}$$

where r is the distance between the photons in the calorimeter, z is the distance from the vertex to the calorimeter, and E_i are the energies of the photons. Since we have

$$\begin{aligned} \sigma_r/r &\approx \sqrt{2} \times 1mm/50cm \approx 0.3\%, \\ \sigma_z/z &\approx 10cm/50m \approx 0.2\%, \\ \sigma_E/E &\approx 0.6\%, \end{aligned} \tag{2.2}$$

the m_{π^0} relative resolution of $\approx 0.7\%$ matches well with this estimate.

2.6 Trigger and Veto counters

The trigger hodoscope is the primary component in the charge-mode trigger. It consists of two planes of plastic scintillator, called "V0" and "V1", each about 2 m square in size, and divided into individual paddles, as shown in Figure 2.8. The paddles are placed such that the gaps between counters (known as "cracks") are in different locations for the two successive planes. This is to prevent a given particle from passing through cracks in both planes (except at discrete locations along the horizontal cracks). The scintillation light is collected by photomultiplier tubes attached to the top and bottom of the scintillator paddles. The beam holes, each 14 cm square in size, were added to the design after it was determined that a significant fraction of the radiation dose in the E731 lead glass was due to hadron interactions in the E731 trigger hodoscopes, which had no beam holes. The output pulses from the photomultiplier tubes are fast enough to allow single-bucket timing.

There are several types of veto counters collectively referred to as "photon ve-
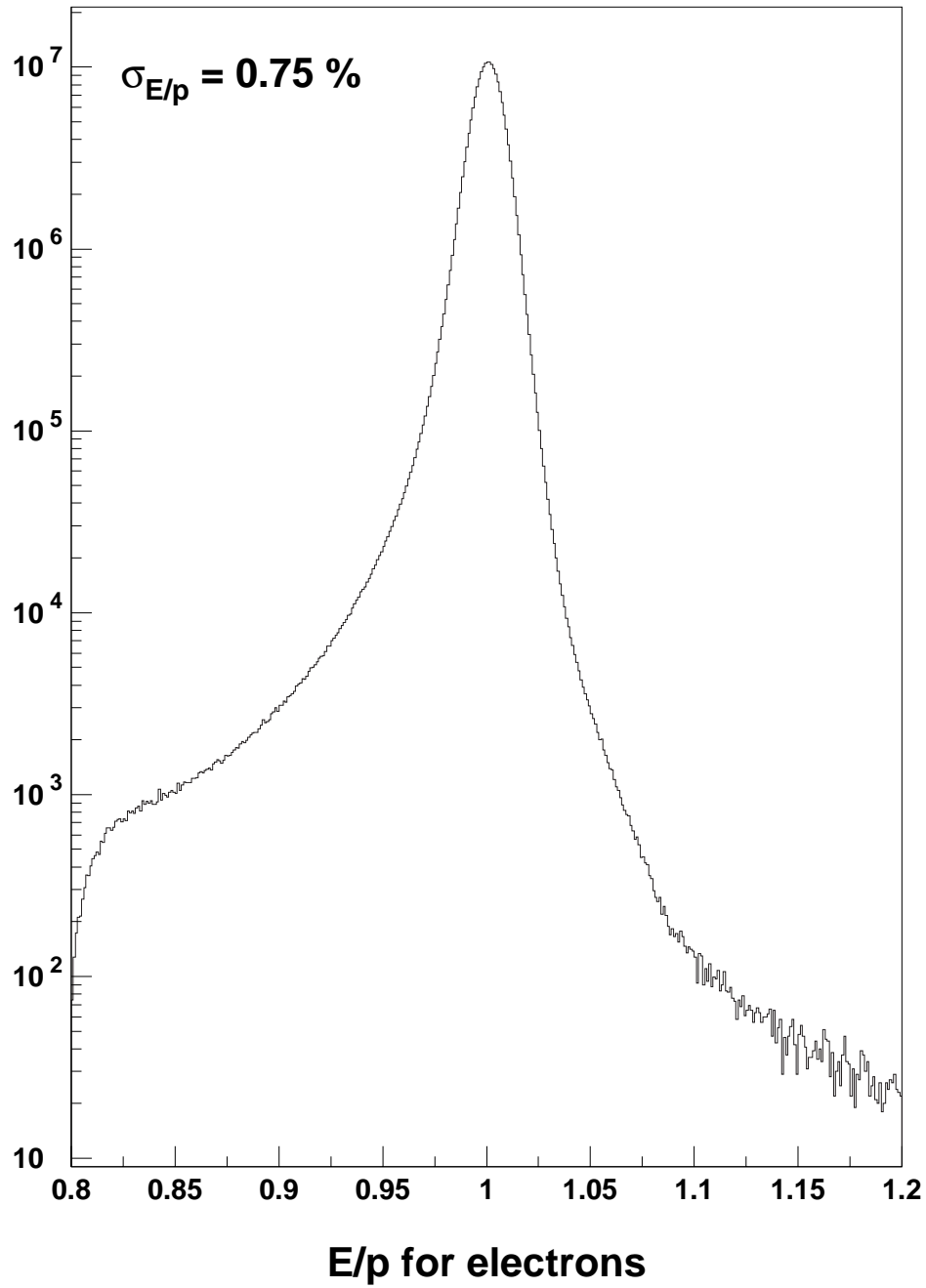
Figure 2.5: Energy/momentum distribution for electrons in $K \to \pi e \nu$ decays. The peak at $E/p = 1$ indicates that electrons deposit all of their energy in the calorimeter. The width of the distribution is due to tracking and calorimeter resolution effects.
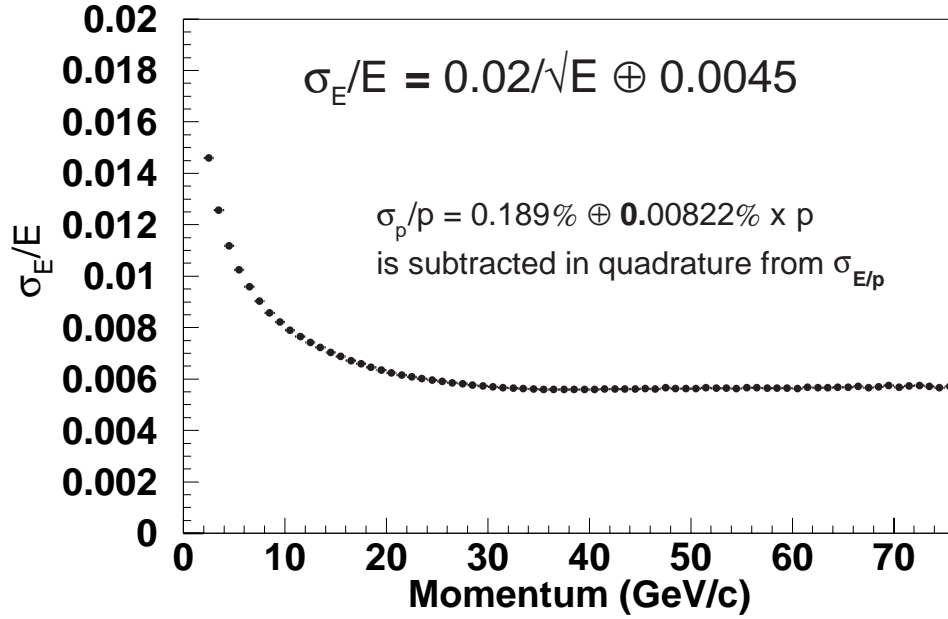
Figure 2.6: Calorimeter energy resolution as a function of track momentum, for electrons. The momentum resolution, which is determined by how well upstream and downstream tracks match at the magnet, has been subtracted in quadrature.

toes". These include the "Ring Counters" (installed along the vacuum tank), "Spectrometer Antis" (at the outer edges of the drift chambers and the calorimeter), and the "Back Anti" (BA) (downstream of the beam holes in the calorimeter, just in front of the muon filter steel). All of these counters are made of alternating layers of lead and scintillator and are divided into segments with individual photomultiplier tubes. The BA is also segmented longitudinally to help distinguish between electromagnetic and hadronic showers. For each photon veto counter, a signal above a certain threshold generates a digital pulse which is sent to the trigger system and may be used in the Level 1 trigger decision.

The Collar Anti is also intended to detect photons, but has a different construction and also has the important task of defining the inner aperture for photons landing near the beam holes of the calorimeter. The CA consists of two identical detectors around the two beam holes of the calorimeter. Each one is 1.5 cm wide to occlude the inner part of the crystals immediately surrounding the beam holes, as shown in Figure 2.9.
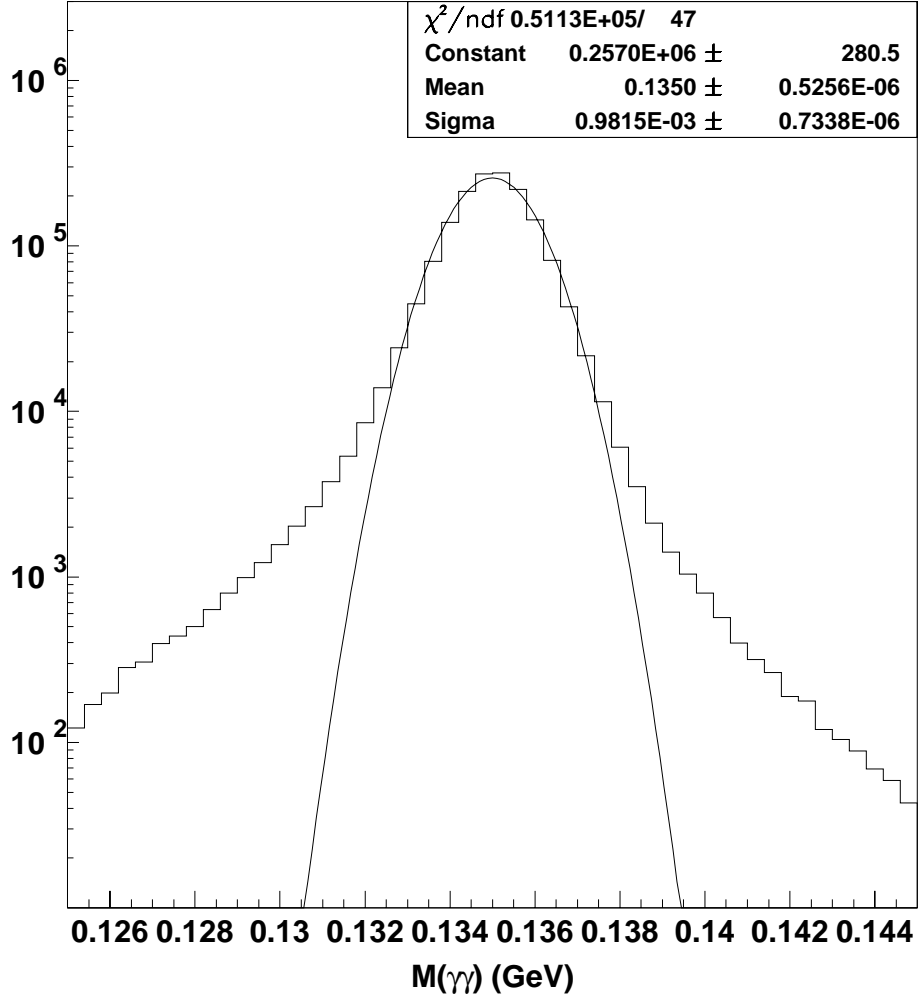
Figure 2.7: Mass of $\gamma\gamma$ pair in $K_L \to \pi^+\pi^-\pi^0$ data.

Behind the calorimeter, we have some additional hadron/muon vetoes. In the downstream direction, we have a lead wall, 15 cm deep, followed by the Hadron-Anti, which detects hadronic shower products. Then comes 1 m worth of steel, followed by the Back-Anti, which can be used to veto photons. Finally, we have a set of two muon counters, MU2 and MU3, each preceded by a steel wall, which are used to veto muons. In our measurement, these can come from pion decays in-flight, or from shower subproducts.
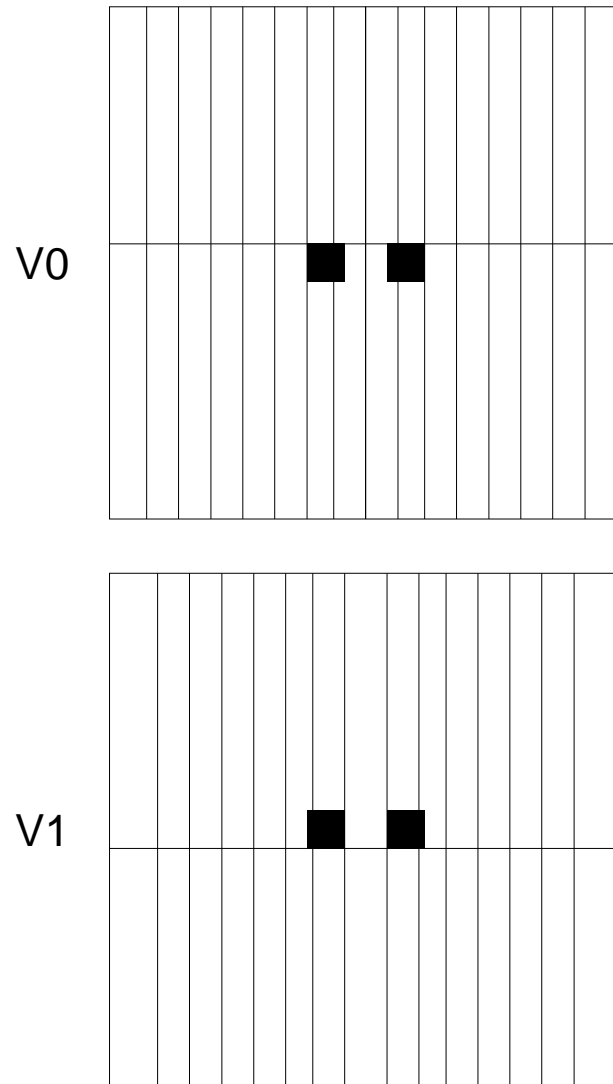
Figure 2.8: Trigger hodoscope banks used in the charge-mode trigger. The banks are approximately 2 m×2 m in size. Note that the paddles are placed such that a particle cannot go through gaps in both banks.
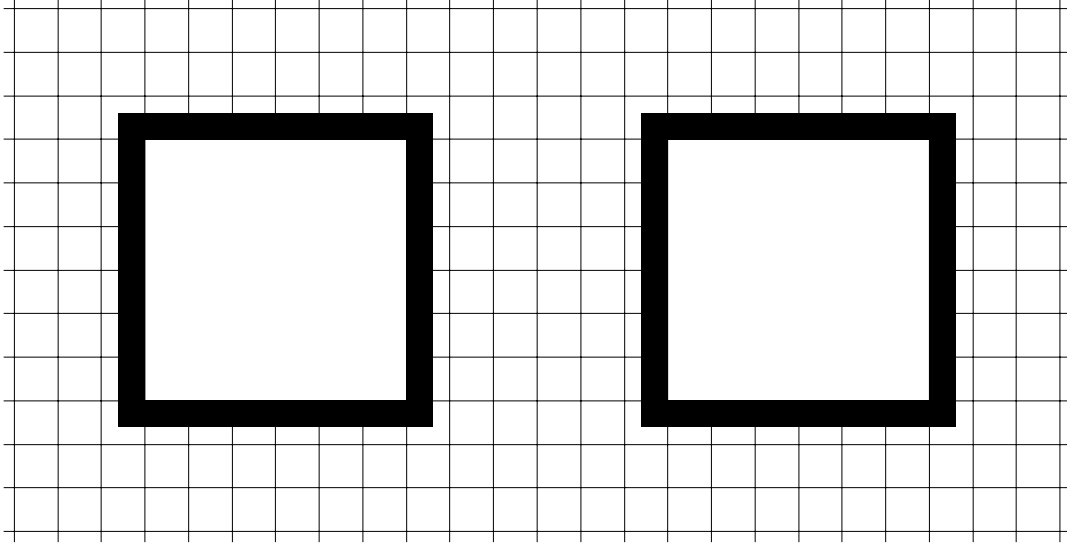
Figure 2.9: Collar Anti geometry.

2.7   The Trigger System

Most of the events resulting from kaons coming from the target are not useful to us. The "Trigger" system is the means by which we select those events which we consider to be "good", and read all detection system outputs and write the information to tape. The KTeV trigger system is described in detail in Chapter 3 of Ref. [17]. It consists of three "levels" with different strategies and deadtime implications. Level 1 uses fast synchronous signals from various detector elements and simple logic to evaluate the state of the detector for every RF bucket. Level 2 consists of a set of specialized electronic processors which evaluate the number and pattern of signals on individual drift chamber wires and calorimeter channels. For events which pass the Level 2 trigger, the detector information is transferred to computer memory, and a Level 3 trigger process, running in parallel on 24 CPUs, reconstructs the event and applies some loose kinematic cuts to select candidate events.

2.7.1   Level 1 Trigger

Several dozen boolean "source" signals are available for the Level 1 trigger decision. For example, one source indicates that at least two counters in the V0 plane of the trigger hodoscope were hit, while another indicates that the total energy deposit in the calorimeter (based on an analog sum of phototube dynode outputs) is above a certain threshold. These sources are formed and combined using mostly

commercial electronics and simple logic. To keep the trigger rate at a manageable level, triggers may be inhibited by fast veto signals from the Regenerator, the Mask-Anti, the photon vetoes, and the muon veto hodoscope. An "accept" decision by the Level 1 trigger initiates the digitization of various detector signals (ADCs, TDCs, and latches) and buffers the continuously-digitized calorimeter information in FIFOs. The raw Level 1 trigger rate is about 60 kHz under normal running conditions. In Chapter 4 we will give the details of the trigger requirements used in $\pi^+\pi^-\pi^0$ events.

2.7.2   Level 2 Trigger

Only the Y views of the drift chambers are used in the Level 2 trigger decision. The hit-counting system, consisting of "Banana" and "Kumquat" modules, takes signals from each wire and counts the number of pairs of complementary wires (or isolated wires) in each chamber which were hit within an appropriate time interval. The hit-counting system takes around 800 ns to provide a result.

An additional Level 2 processor called the "Y Track Finder" (YTF) was added to evaluate whether the drift chamber hits found by the hit-counting system are consistent with two straight tracks. It is designed to be used for $\pi^+\pi^-$, and so it looks for one upward-going track and one downward-going track, with an overlap region in the central region of the drift chamber system which satisfies both the "up" and "down" requirements. It was built from commercial programmable-logic and memory-lookup modules. It uses coarse-grained outputs from the hit-counting system (each one an OR of 16 contiguous wires) as its inputs, and generally returns a decision a few hundred nanoseconds after the hit-counting system.

If an event passes the Level 2 trigger, then digitization is allowed to finish and the front-end modules are read out, a process which takes around 18 μs. If the event fails, then the front-end modules are cleared and the trigger system is re-enabled after a few hundred nanoseconds. Front-end readout and clearing together cause a fractional deadtime of about 35% under normal running conditions. The total Level 2 trigger rate is about 10 kHz.

2.7.3   Level 1 and Level 2 Trigger Definitions

Both the Level 1 and Level 2 control logic use programmable memory lookup units (MLUs) to make the trigger decision based on the inputs. A text configuration file is used to define symbols for logical combinations of low-level trigger inputs and to specify the trigger requirements for 16 trigger types; the file is parsed to generate the necessary memory maps to be loaded into the MLUs. The trigger is designed to be almost 100% efficient for the $\pi\pi$ modes, to minimize possible biases on the measurement of direct CP violation. The same trigger used in $\pi^+\pi^-$ accepts $\pi^+\pi^-\pi^0$ events. For example, we define loose trigger-hodoscope, hit-counting and YTF trigger requirements to be insensitive to a single crack or inefficiency.

Additionally, there are special triggers with looser requirements to permit study of inefficiencies in the nominal triggers. There are also extra triggers to collect $3\pi^0$ decays for detector studies and to select candidates for several rare kaon and hyperon decay modes. Among other things, this makes it possible to measure the Dalitz parameters for $K_L \to \pi^0\pi^0\pi^0$ decays. Finally, an "accidental" trigger is formed, using (prescaled) scintillation counters near the kaon production target, to randomly record the underlying activity in the KTeV detector with the same instantaneous-intensity distribution as the physics data.

In addition to the beam-related triggers, there is a separate set of hard-wired "calibration" trigger, used mostly to monitor the response of the calorimeter to light from the laser calibration system and to cosmic-ray muons, and to measure "pedestals" (baseline digitized values reported by the ADCs and DPMTs when no energy has been deposited).

2.7.4 Level 3 Trigger

The detector data is read out into VME memory modules with sufficient capacity to hold the data from an entire 20-second spill. Therefore, the Level 3 computers have a whole minute to process the data without introducing any deadtime. A minimal set of kinematic and particle-identification cuts are applied to select $\pi^+\pi^-\pi^0$ candidates, and the cuts are loose since event reconstruction has to rely on preliminary detector calibrations. The track and vertex candidates are reconstructed first, and the approximate charged invariant mass, $m_{\pi^+\pi^-}$ is calculated for each vertex candidate. The charged invariant mass is required to verify 0.2 GeV$< m_{\pi^+\pi^-} <$0.4 GeV. If this is true, the calorimeter information is unpacked and clusters are found and matched to the tracks. If the tracks have matching clusters, the quantity E/p is calculated for each track and required to be less than 0.9. Additionally, a third cluster with $E > 1$ GeV is required, together with a minimum separation between the tracks and photon clusters of 0.2 m. Lastly, an effective prescale of 7 is implemented by requiring that $\pi^+\pi^-\pi^0$ events pass both TRIGGER 1 and TRIGGER 2. TRIGGER 2 is the same as TRIGGER 1 with the additional requirement of HCC readout, and it is prescaled by 7. If all these conditions are met, the event is tagged as a $\pi^+\pi^-\pi^0$ candidate and written to tape.

CHAPTER 3
THE KTEV 1997 RUN

The KTeV experiment's 1997 run collected data from January until September of 1997. The detector can function in two different configurations: experiment E832, designed to measure $Re(\epsilon'/\epsilon)$, and experiment E799, which studies a variety of rare kaon, π^0, and hyperon decays. The main difference between E832 and E799 is that, in the latter, the Mask-Anti and regenerator are taken away from the beam, and *transition radiation detectors* are placed in the beam path, between the fourth drift chamber and the calorimeter. Our data comes from the E832 collected set, which run between April and July of 1997.

Data was collected around the clock, with shifts of three people handling tasks such as starting new runs, monitoring various detector performance indicators, resetting the system when needed, and calling specific experts if serious problems occurred.

3.1 Data Taking

KTeV is a complex experiment, and problems are bound to occur. The main problem we had involved the calorimeter readout electronics, although we also had other system problems as well. Overall, 15-20% of otherwise good beam time was lost due to beamline and detector problems. We will mention the most important problems we encountered.

3.1.1 Calorimeter Readout

The KTeV CsI calorimeter has about 3100 photomultiplier tube channels in its readout. The photomultipier tube signals are collected by DPMT boards. The QIEs occasionally indicated an incorrect readout range. It was thought that this was related to a bad batch of chips, but it was later demonstrated to be intrinsic to the particular chip fabrication process used. The failure rate was about one per day.

Any serious DPMT failure was generally noticed within a few minutes by the monitoring software and triggered an alarm. We generally replaced the DPMT immediately, which involved steering away most of the primary proton beam and putting in the beam stop to allow people to go into the calorimeter blockhouse.

Thankfully, the actual replacement was simple, causing a downtime of less than an hour.

3.1.2 Drift Chamber System

The drift chambers had a number of problems. After they were installed in the KTeV Hall, it was found that the sense wires were able to pick up electronic noise, which after amplification, was large enough to be recorded as fake hits. In particular, there was substantial noise during the asynchronous readout of the digitized TDC information, when the detector should have been ready to record another event. To avoid this problem a number of modifications were made. Extra grounding was added to the first amplification stage (at the chambers themselves). The gain of the second-stage analog amplifiers was reduced as well. These modifications generally reduced the noise pickup level to below the discriminator threshold.

There were a number of instances in which excessive current was drawn from the high-voltage supplies. A few such cases turned out to be due to discharges from wire stubs or other metal objects. Cleaning the interiors of the chambers seemed to help at one point. When high-intensity beam was delivered for the first time, there was a concern about how much current was being drawn, and the chamber voltages were lowered. Even so, there were several instances of unexplained current draw during data collection which were cured by cycling the high voltage. This current draw was generally at a low level and did not seem to adversely affect the drift chamber efficiencies.

On several occasions, one of the drift chamber electronic subsystems would begin to "oscillate", producing a continuous stream of fake hits on many of its wires. This happened in sets of sixteen channels, associated with the fact that there is one amplification/discrimination card every sixteen channels. Usually, all channels in a card would start to oscillate, as they are coupled by the power supply rails, and peak-to-peak oscillations in one amplifier can easily trigger oscillations in neighboring devices. The power to the amplification/discrimination system had to be cycled to stop these oscillations. The most likely source of the instability of the system was the high gain of the second amplification stage: there was no filtering on the output of this stage to the discriminator (as was later discovered). This, together with the undampened feedback loop of the design, can cause an oscillation of the amplification stage at its bandwidth limit frequency of 3 MHz. This was observed afterwards, and we will discuss it in Section 3.1.4.

An important problem during the 1997 running was the high level of hit pairs whose "sum-of-distances" (SOD) to the hit wires was bigger than expected. A "good SOD" is a hit pair whose distances to the sense wires adds up to 6.35 mm, which is half the cell size. "Low SODs" are expected because delta-rays and other charged particles can produce extra hits, which arrive to the sense wire before the actual

hit. Figure 3.1 shows the SOD plot for the 1997 run, and compares it with the one for the E773 [18] experiment, which used the same drift chambers.

Save for resolution effects, a properly functioning chamber should not have an excessive number of high SODs present in the SOD distributions. This can happen if
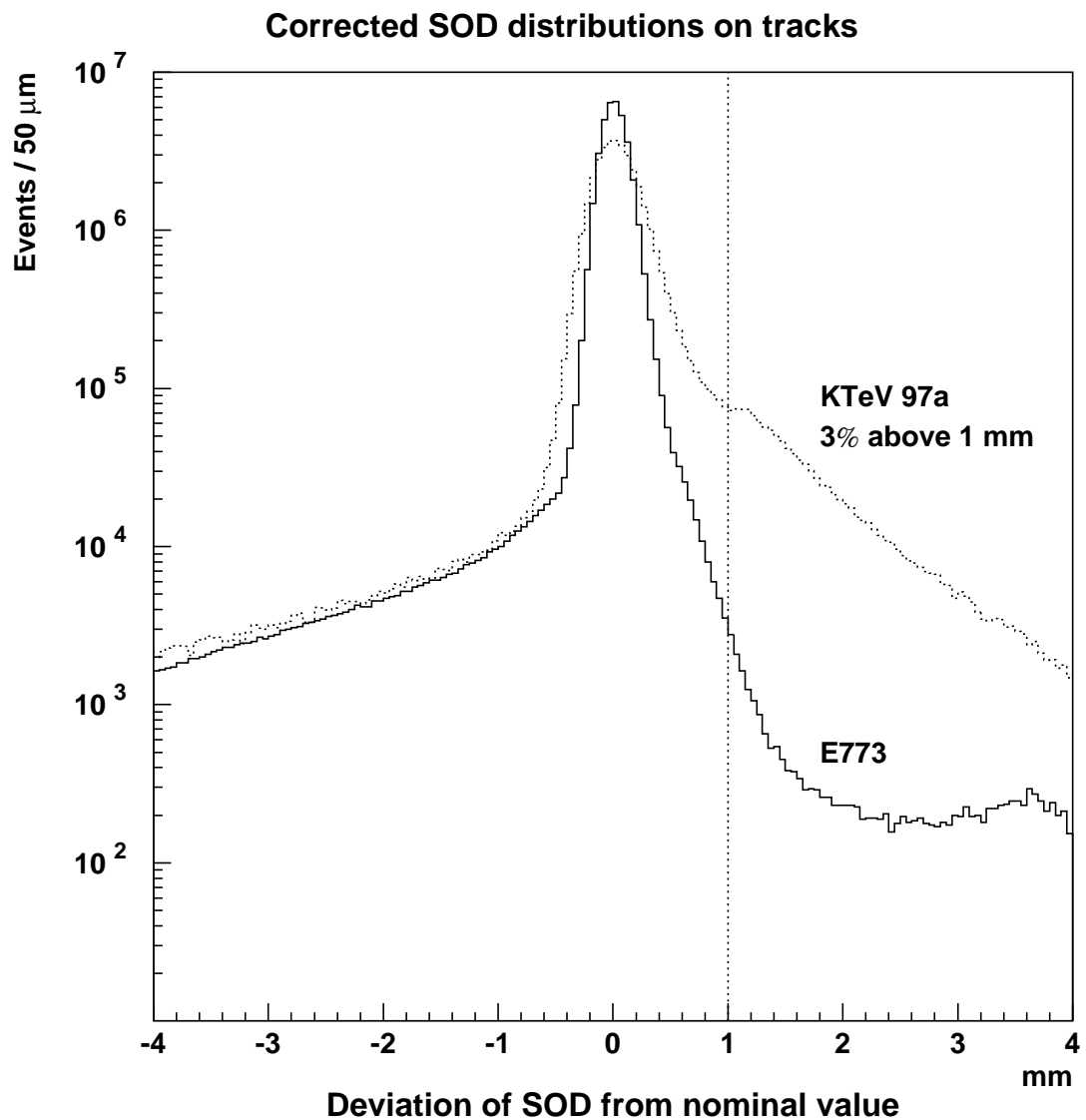
Figure 3.1: "Sum of Distances" distribution for the first portion of the KTeV run, compared to the one from E773 [18], which used the same drift chambers. Notice how much higher the high-SOD tail is.

the gain of the chamber is not high enough. This gain can be raised by increasing the accelerating voltage, but we are constrained by current draw. It can also be raised with a higher analog gain, but then we are constrained by noise pickup and instability of the system. Another possible reason for high SODs is radiation damage: a sense wire can be damaged at various points, making it less efficient. This was clearly indicated by the fact that the high SOD probability was much higher where the radiation was higher: in the beam region of DC1. Moreover, the problem got worse as the run progressed, indicating that all wires were being affected more and more by the radiation deterioration. It is not clear what mechanism produced the wire deterioration. Photomicrographs of the wires were taken after the run. It was seen that some wires had developed small silicon deposits on them, which might be the cause of the inefficiency, and might explain why the performance got worse as time progressed.

The biggest changes in the high SOD probability were seen when the high voltages were lowered from 2500 V to 2450 V. The remaining time dependence showed some correlation with atmospheric pressure. These two factors are directly related to drift chamber gain. There was also some dependence on beam intensity, though the loss probability changed by only $\sim 30\%$ of itself between nominal intensity and very low intensity, so the bulk of the effect is independent of intensity. The intensity dependence is greatest in the beam regions of the drift chambers.

It was established early on that most instances of the high-SOD effect occur when a particle passes close to a wire (within a few hundred microns): it is the wire *closest* to the track that mismeasures the drift time. This suggested a mechanism which we now believe to be the correct explanation for the high-SOD effect: the total gain of the chamber gas and electronics was too low for the system to trigger on *single* electron hits. When a particle passes far from a wire, several drift electrons reach the wire at about the same time, giving a peaked, short pulse. However, when a particle passes close to a wire, the drift electrons tend to dribble in, giving a broad, long pulse. The first few drift electrons arrive one at a time, resulting in a broad pulse. Then two or more may arrive simultaneously and trigger the system. The end result is a bigger spread in hit times than normally expected.

The probability of mismeasuring a hit distance varies significantly from wire to wire, presumably due to small gain or threshold variations from channel to channel. It also varies along the length of a given wire. Intriguingly, many wires have one or more spots where the high-SOD probability is *very* high, which we have named "freckles." The freckles are highly localized, with sizes of order a few millimeters, and generally persist throughout the whole 1997 run. This is in line with the carbon fiber formations observed on the wires after the experiment was over. Usually the wire also has a significant inefficiency, i.e. a chance that no hit at all will be recorded at the same spot, supporting the idea that a freckle is a place where the wire has a very low effective gain.

We used the $e\pi\nu$ and $\pi^+\pi^-\pi^0$ decay channels in the random-accept sample to

map out the time and position dependance of the high-SOD probability (with separate maps for the two regenerator positions) and added these effects to the drift chamber simulation in the Monte Carlo. Figure 3.2 shows the high-SOD probability and missing-hit probability distributions in data, determined by the random-accept sample.

3.1.3   Miscellaneous Other Problems

We experienced some additional problems during physics data taking. We will mention a few of the most relevant issues here.

The digitized information from the various parts of the detector was transmitted to the computer memories along a rather convoluted path. The calorimeter information was assembled asynchronously by a "Crate-Trigger Interface/Readout Controller" (CTI/RC) in each crate of pipeline modules, using a custom backplane. For all other systems, readout within a crate was based on the "FERA" readout protocol developed by LeCroy for the ADC modules of the same name; it relied on front-panel cables which tended to be fragile, especially in crates where modules of different types were in the same readout chain. In all cases, the data from each crate was transmitted to the computer memories along ribbon cables using the RS-485 protocol, but because total distances of a few hundred feet were involved, it was necessary to add "repeaters" at several places to retransmit the digital information. All of these systems were subject to occasional glitches, which generally either froze the data-acquisition system or else caused errors when events were unpacked, and required the system to be reset. Monitoring software was developed and improved over time to alert the people on shift to problems as they occurred.

3.1.4   Drift Chamber Improvements for the 1999 KTeV Run

After the 1997 run had concluded, we decided that we needed to improve the drift chamber performance for the upcoming 1999 run. This comprised a set of improvements. Firstly, some of the chambers were rewired. This was most important for those chambers exposed to higher beam intensities, which showed the most damage. Secondly, the gas supply and alcohol bubbling systems were refurbished. The biggest change in the drift chamber turned out to be the modification of the electronics. The hit detection system has three stages. The first stage is signal amplification at the chamber itself. A signal from a wire gets picked up by a current-sensitive device, which in turn does some amplification and sends a balanced signal to the second stage amplifier. The second stage amplifier and discrimination circuit is integrated in cards, sixteen channels each, which are located in a separate rack. This stage receives the balanced signal from the first amplifier and amplifies it some more, putting out a single-ended signal for the discriminator to trigger on. Once discriminated, the signal is fed to a TDC system, which does the timing with a resolution of 0.5 ns, and sends the result upstairs.

High-sod probability in DC1X, regenerator on left

Missing-hit probability in DC1X, regenerator on left
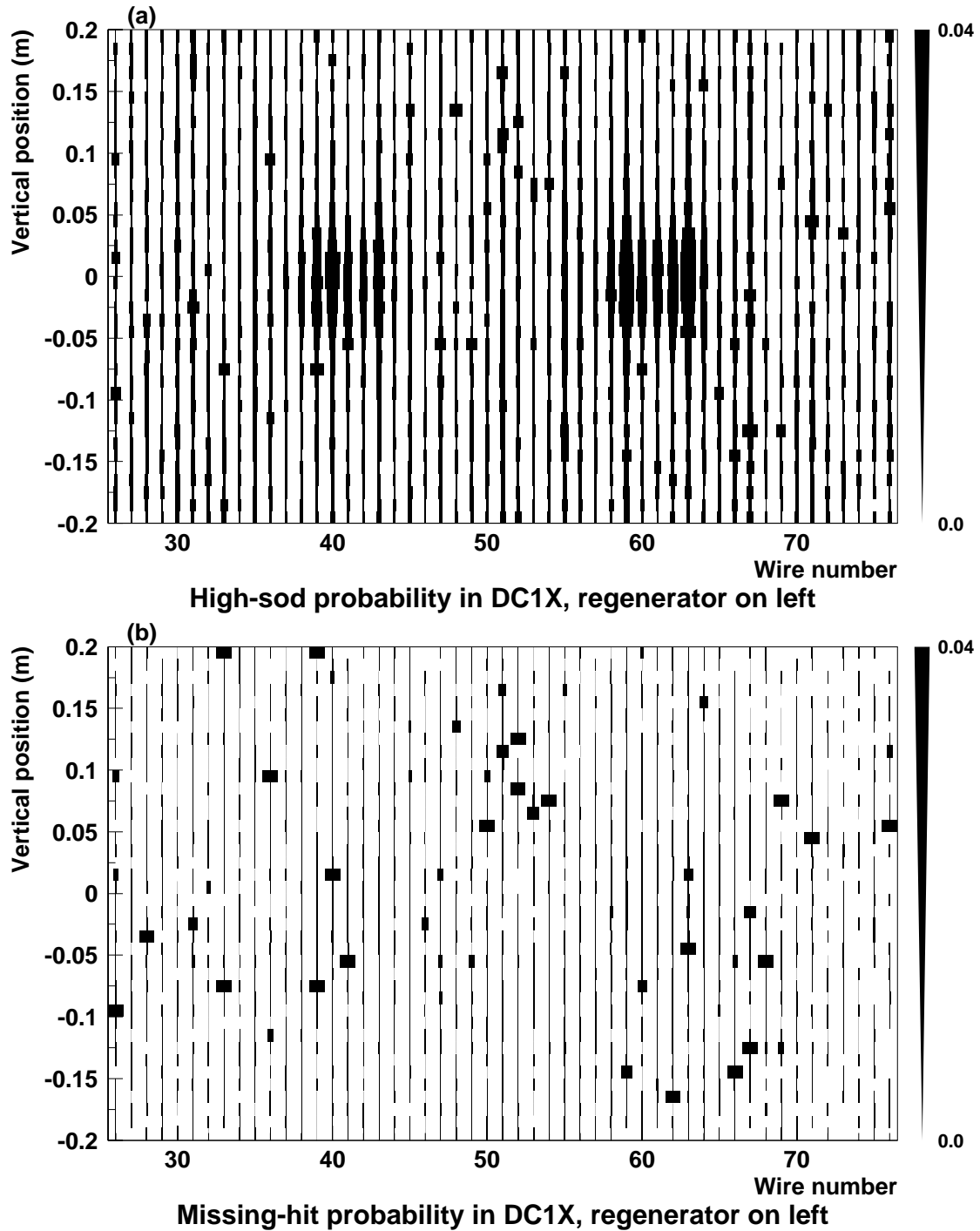
Figure 3.2: High-SOD and missing-hit probability distributions in Chamber 1 (DC1). Notice the presence of high inefficiency spots in the bottom plot. Their positions were quite stable throughout the run.

Our goal was to increase the drift chamber system efficiency. As mentioned earlier, this can be done by increasing the amplifier gain. This is, however, not straightforward. Increasing the gain means a higher chance of noise triggering the system. It also means that the system would be prone to oscillations. There are two important sources of noise: the digital signal being sent to the TDCs; and the digital noise picked up by the sense wires themselves during system readout. Increasing gain alone would lead to oscillations. Looking at drift chamber signals using an Fe55 source, we determined that the rise time of a signal was, at best, 1-2 ns. So we added a low-pass filter with a time constant of roughly 1 ns between the second amplification stage and the discrimination circuit. This made it possible to increase the gain without system oscillations. To further decrease the chance of oscillations and picking up noise, we added ferrite cores to all the ribbon cables going from the discriminators to the TDCs. During the 1999 run, the system experienced a few instances of oscillation, but for the most part it behaved admirably.

3.2   Data Reduction

KTeV generated a very large amount of data. For E832 alone, over five billion events were written out to about 3000 DLT tapes. Since each has a nominal capacity of 10 GB before compression, the total data stream size is about 35 terabytes. Accessing the data presented a major challenge, since it is not practical to read through all 3000 tapes multiple times for the various analyses to be performed. The data was "split" into separate datasets according to the sample tags determined by the Level 3 processing. All events tagged as $\pi^+\pi^-\pi^0$ candidates were copied to 126 tapes. During the copy procedure, the calorimeter and HCC information was "squeezed" into a more compact format, reducing the average event size of an event by about 40%, without any loss of information. The subsequent selection varied from sample to sample, each analysis requiring different characteristics.

CHAPTER 4
$K_L \to \pi^+\pi^-\pi^0$ SAMPLE SELECTION

We will describe how the $K_L \to \pi^+\pi^-\pi^0$ sample is selected from the data: the hardware trigger requirements; the reconstruction; and the event-selection cuts applied to select the final $\pi^+\pi^-\pi^0$ sample for the measurement of the Dalitz parameters.

4.1   Hardware Trigger Requirements: Level 1

The Level 1 trigger for $\pi^+\pi^-\pi^0$ events uses various logical sources to make a decision and pass the event to Level 2. There are two main trigger sources in the charge mode trigger in E832: the V0 and V1 trigger hodoscopes and drift chambers 1 and 2, used as hit counting devices. All in all, Level 1 processing takes about 19 ns.

4.1.1   Trigger Hodoscope Banks

The main hardware trigger are the V0 and V1 hodoscope banks previously described (see Figure 2.8). Two hits in one of the hodoscope planes, and one hit in the other are required. Additionally, we impose a topological condition: there must be at least one hit in the "upper" and one in the "lower" portion of the hit counters, and one of them in the "east" and one in the "west" regions (right and left portions of the counters, when looking downstream). The upper and lower regions overlap slightly, and so do the east and west regions. A charged particle hitting the overlap region would count as belonging to both regions. This trigger is designed to be most efficient for $\pi^+\pi^-$ events, as they will naturally have this topology given that the incoming kaon is roughly centered with respect to the hit counters, as it's position is inside one of the beam holes. For $\pi^+\pi^-\pi^0$, this trigger requirement is not as efficient given the presence of the π^0 , which can carry a substantial amount of momentum.

4.1.2   Drift Chambers as Hit Counters

The probability of a kaon decaying between drift chamber 1 and drift chamber 2 is rather large. We do not want events like these, as we would not have enough tracking information to reconstruct the charged pion momenta. To reject these events at Level 1, avoiding useless Level 2 deadtime, the X and Y views of chambers 1 and 2 are added in hardware to form the equivalent of a hit counter. The "paddles" are

formed by adding together 16 wires over the two overlapping planes in each view, i.e. 8 wires from the upstream and 8 wires from the downstream planes in a given view. This makes each effective "paddle" of width 10.16 cm. Sense wire signals are "OR"-ed together in hardware by a DC-OR system, and a central controller counts the number of paddles hit in each chamber plane. This controller produces two sources per X and Y planes in each chamber, that are used in the Level 1 trigger. Given the relatively long drift times of ∼150 ns, these sources cannot have the single-bucket resolution that most other Level 1 sources have. It was chosen to take a 90 ns window for these sources, a little more than *half* the drift time, as a hit ought to have a drift time less than half the maximum for one of the two planes in a given view. Additionally, since a hit can be missed, only three of the four views are required.

4.1.3   Vetoes

The Charge-mode trigger was vetoed if there was significant energy deposited in the regenerator, the spectrometer antis, the Cesium-Iodide anti, or the muon hodoscope.

4.2   Level 2 Trigger Requirements

Once the Level 1 trigger is satisfied, the Level 2 trigger analysis is started. Level 2 processing takes roughly 2 μs. The first step is hit counting in the Y views of the drift chambers. An event was required to have at least two hits in any three chambers, and at least one hit in the remaining chamber. Additionally, the "Y Track Finder" was required to find one track in the upper half of the chambers and one track in the lower half, with a small overlap region slightly bigger than the beam widths [1]. Finally, one of the tracks was allowed to miss a hit in either chambers 1 or 2.

4.3   Level 3 Trigger Requirements

The Level 3 trigger takes the longest time to process, about 2 ms. It required some loose kinematic constraints on the $\pi^+\pi^-$ invariant mass and the energy-momentum ratio of each track:

$$0.2 \; GeV/c^2 < m_{\pi^+\pi^-} < 0.4 GeV/c^2, \qquad E/p < 0.9. \tag{4.1}$$

together with an extra cluster in the calorimeter, with E>1 GeV, at least 20 cm away from the track positions at the calorimeter.

---

[1]As with the hodoscope logic, this is optimal for $\pi^+\pi^-$ events, and will eliminate a bigger fraction of otherwise good $\pi^+\pi^-\pi^0$ events.

4.4   Charged Pion Tracking

The offline analysis of the sample begins by finding tracks in the spectrometer. We first unpack the drift chamber information and convert drift times to distances from the sense wires. For a given wire, only the earliest hit is considered. Most of the time, a track leaves one hit per plane. However, there is a probability that a track would leave no hit, and since there are 32 planes in the tracking system, this becomes all the more likely. The types of possible "imperfections" are:

- "Delta rays", which are high energy electrons, knocked off of the gas atoms by the incident pion. These electrons produce a secondary ionization trail, resulting in a low SOD;

- The two charged pions pass through the same sense wire cell, leading to a low-SOD;

- Inefficiencies can produce a missed hit or a delayed hit, leading to a high-SOD.

A "good" SOD is within ± 1 mm of the cell size (± 1.5 mm in the X views of chambers 3 and 4, since the bending in the magnet leads to bigger incident angles, which broadens the SOD distribution). To accommodate for imperfections, various possible configurations are evaluated. If the number of configurations gets to high, the worst types of configurations are dropped.

To decide which set of hit configurations best represents our event, we first look at the Y hits. Since, to first order, there is no magnetic field in the X or Z directions, the Y view of a track should be straight from the first to the last chamber. Thus, all Y hits are required to lie on a line. The hits must have, at least, two good SOD pairs. As for the X direction, there is a looser requirement, since there is bending in the magnet. In this case, tracks are required to match within 6 mm at the magnet bending plane (usually referred to as "kick plane"), which is the effective plane at which tracks bend [2].

Even with all these conditions, there are usually more than one set of candidates for the X and Y views. Since the drift chambers have only one set of horizontal and vertical wires, external information is required to pair up hits in the two views to form tracks. For this purpose we use the clusters in the calorimeter: we require each possible candidate to extrapolate within 7 cm of a cluster in the calorimeter.

Finally, the possible combinations left are evaluated according to the vertex they point to. For a given vertex candidate, the two tracks are not allowed to share any hits.

Once we have determined the best track candidates, we apply second order corrections to the tracking information: fringe fields from the analysis magnet and

---

[2]This is only an abstraction, of course. A fringe field correction is applied to compensate for the fact that fringe field at drift chambers 2 and 3 will start bending the tracks.

magnetic field non-uniformities, calculated from the field map variations measured independently in the magnet.

The final decision is made based on the quality of the vertex found (minimum "vertex χ^2"), and the smallest discrepancy of extrapolated tracks at the kick plane (minimum "Offmag χ^2"). How many missing hits there are also plays a role in this estimation.

4.5 π^0 Reconstruction

The requirements for a $\pi^+\pi^-\pi^0$ event to pass Level 3 are:

- Satisfy all charged event tracking conditions, as if it were a $\pi^+\pi^-$ event; and

- An additional cluster, with $E > 1$ GeV, should be present in the calorimeter.

These are very loose requirements for a $\pi^+\pi^-\pi^0$ event. During offline analysis, the photon clusters are required to have an energy of at least $E > 3$ GeV, and the two photon clusters are required to reconstruct an invariant mass close to the π^0 mass, which in and of itself is a very stringent condition. It is important to point out that extra low energy clusters are not a cause for vetoing the event. This allows us to use this sample for the measurement of the radiative cross section, as described in Appendix D.

4.6 Pion Showers

Charged pions have electromagnetic and hadronic interactions with the Cesium-Iodide in the calorimeter. Given the momentum spectrum of the pions in our sample, roughly $10-80 GeV$, the ionization energy loss per unit length of material, dE/dx, is approximately constant. This is known as the "Minimum Ionizing Particle" (MIP) regime. For pions in Cesium-Iodide we have $dE/dx|_{min} = 1.243$ MeV/(g/cm^2) (PDG2000 [8]). Since the crystals are $\sim$50 cm in length, the energy deposited by MIP pions is $E_{CsI} \approx 0.282$ GeV. Figure 4.1 shows the energy of track clusters in the calorimeter, as measured from data. As can be seen here, the peak is at $E_{CsI}^{peak} \approx 0.37$ GeV, which is higher than the value quoted above. This is because the MIP value for dE/dx is the minimum possible. For higher pion momenta, the energy deposited per unit length of material slowly increases. From the information available in PDG2000 [8], page 164, Figure 23.3, one can estimate that the value of dE/dx in the 10-80 GeV/c pion momentum range is roughly 30% higher than the value at the minimum, which explains the difference [3]. Notice also that the peak in Figure 4.1 has a long tail. These are events where the pion had some hadronic

---

[3]The same holds true for muons, so an energy cut could be used to select higher momentum muons during calibration runs.

interactions with the Cesium-Iodide. Figure 4.2 shows an event in which one of the charged pions showered in the calorimeter. Note that the energy it deposited is a substantial amount of its momentum ($E/p \approx 0.42$), whereas the other pion did not deposit much energy. About 2/3 of incident charged pions will shower in the calorimeter. This means that, for $\pi^+\pi^-\pi^0$, the probability of both pions *not* showering is roughly 1/10. Figure 4.3 shows an event in which neither pion deposited much energy in the calorimeter.

We have chosen to implement a cut to reject events with "big" pion showers. We do this by requiring that all charged pions be such that the energy deposited in the calorimeter is less than a certain threshold:

$$E_{CsI,tracks} < 1GeV, \tag{4.2}$$

where the threshold value was chosen from the cluster energy distribution in Figure 4.1. This "MIP sample", as we will call it, was originally intended for the measurement of the radiative branching ratio

$$Br = \frac{\Gamma(K_L \to \pi^+\pi^-\pi^0\gamma\ )}{\Gamma(K_L \to \pi^+\pi^-\pi^0\ )}\ , \tag{4.3}$$

where we need very small track clusters in order to reconstruct the radiative photon accurately. However, we decided that it would be best to use this sample for the Dalitz measurement as well, to reduce possible biases from pion showers. These showers tend to be big in size, they can easily have a 20-30 cm radius. They also tend to have quite irregular shapes. A great deal of effort has been put in simulating this accurately in the Monte Carlo, but it is not clear how well the simulation reproduces the shower details. Additionally, photon clusters can be contaminated by shower secondaries. Although it has been shown that event *loss* due to this effect is negligible at photon-track separations bigger than about 30 cm, the cluster energies could be modified, which would affect our reconstruction.

4.7   Analysis Cuts

We will now discuss the main analysis cuts implemented in this analysis.

4.7.1   Trigger Verification

We verify that the reconstructed tracks obey the correct hodoscope "up-down" and "east-west" logics that we have already described. The data has a small tail that does not verify this logic. This could be due to accidental activity in the trigger hodoscopes. For this reason we force the up-down and east-west requirements in the offline analysis by extrapolating tracks to the hodoscopes and verifying that the logic is satisfied. We also check that MU3, the muon counter downstream of MU2,
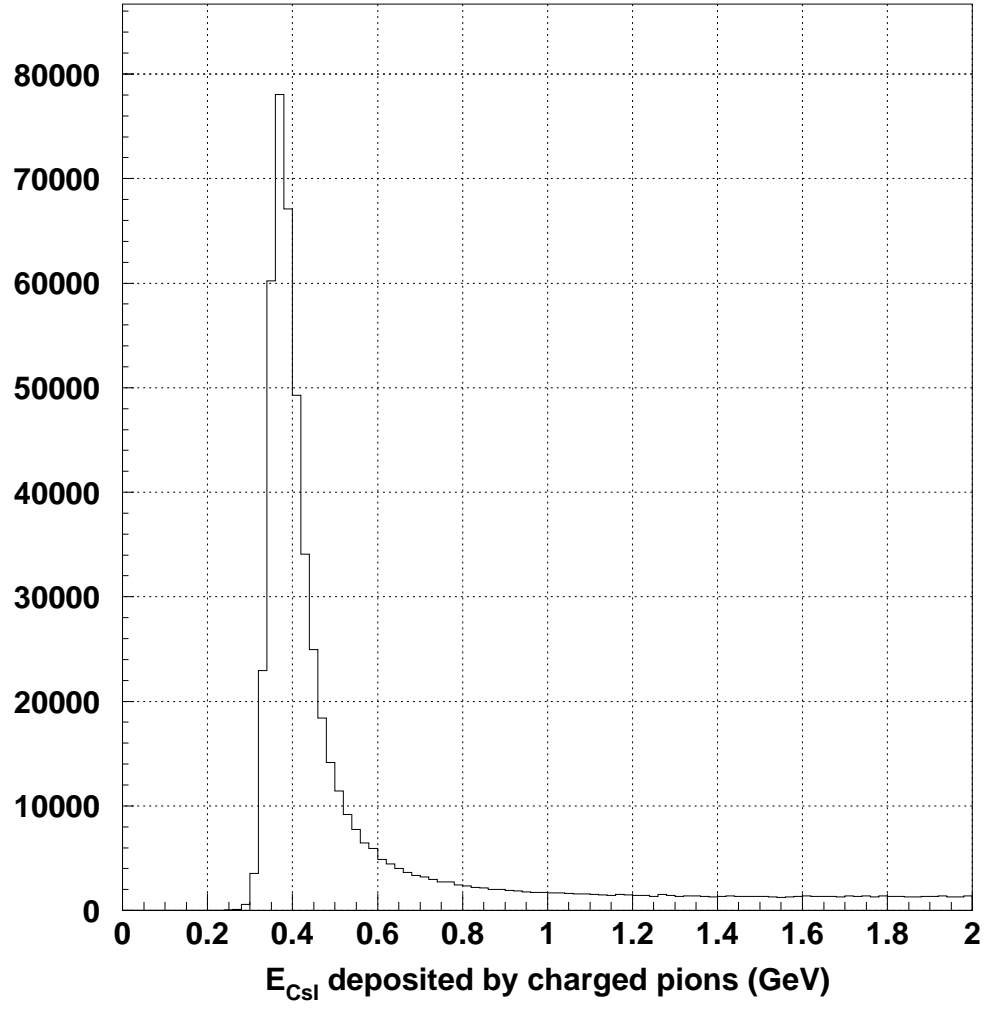
Figure 4.1: Energy distribution of calorimeter clusters from charged tracks. The peak corresponds to the energy deposited by a MIP particle in the calorimeter.

36

Figure 4.2: Sample event with one charged pion showering in the calorimeter, in the upper right quadrant. Notice that it deposits a substantial amount of its energy in the calorimeter ($E/p \sim 0.42$).
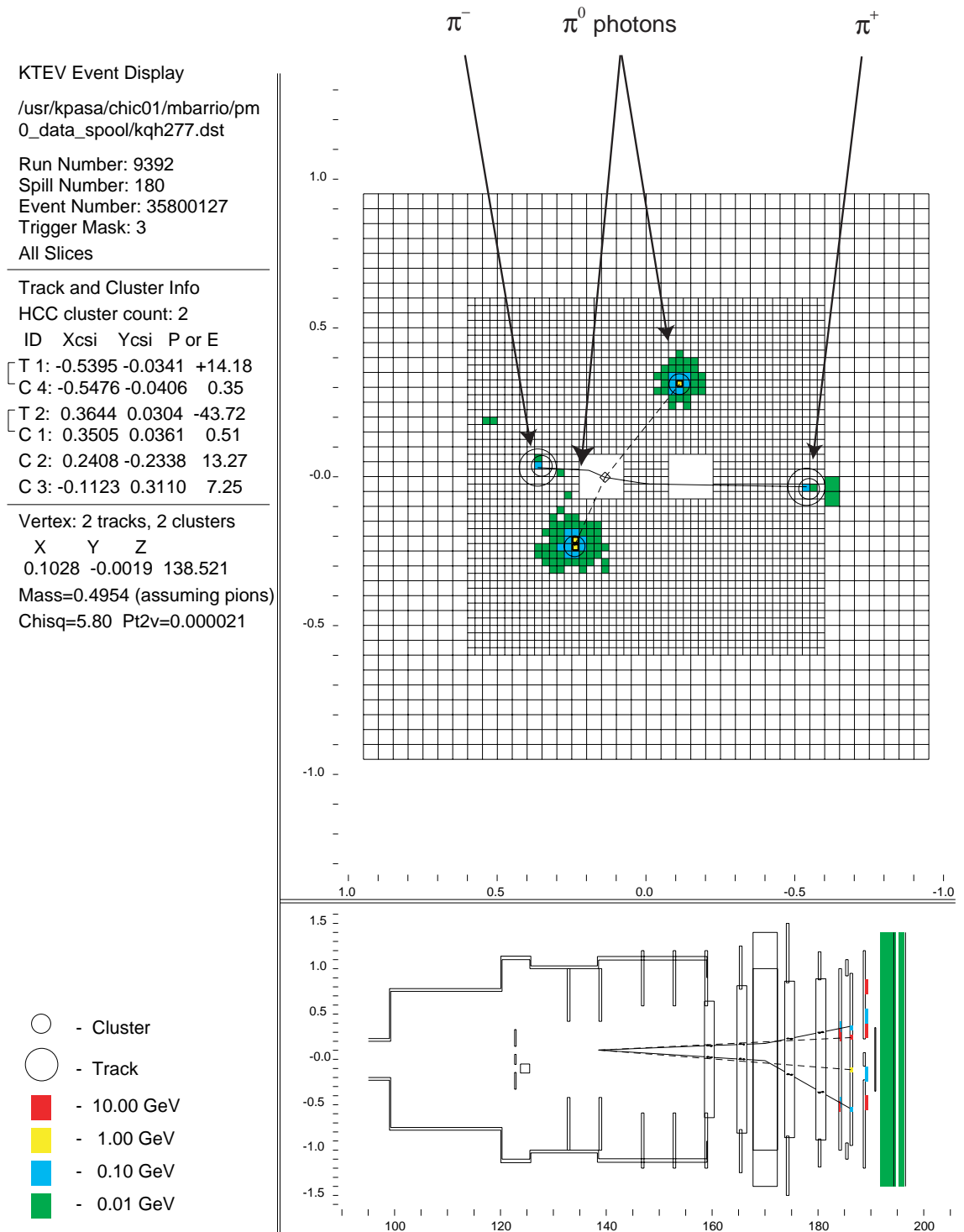
Figure 4.3: Sample "MIP" event in the calorimeter. Here both pions are minimum ionizing. The higher momentum pion leaves a bit more energy than the lower energy one, which might indicate that it showered some.

did not fire. An inefficiency in MU2 could cause it not to fire, in which case a hit in MU3 serves as a backup.

4.7.2   Veto Counters

The main veto cut in our analysis is Regenerator activity. Scattered events in the Regenerator could "look" as if they were coming from the Vacuum beam. Such events would normally have a big transverse momentum, and would be rejected by this cut. Still we prefer to apply the cut to avoid any problems. No cuts are made on BA or CA energies, as small pion showers could trigger these counters, and this is not simulated in the Monte Carlo.

4.7.3   Aperture and Fiducial Cuts

The KTeV detector has a number of physical apertures which limit the acceptance of $\pi^+\pi^-\pi^0$ events. We know these aperture sizes and positions with good precision. However, charged pion tracks can pass through some amount of matter leaving little energy, which effectively reduces the efficiency of veto detectors, particularly at the edges. To avoid having to simulate these edge effects, and to make sure both apertures are the same in the data and Monte Carlo samples, we impose slightly tighter clearance cuts than the ones defined by the apertures and detector boundaries.

Lets first describe these cuts on charged pions. Tracks are required to be at least 3 mm away from the Mask Anti edges (see Figure 2.1). The tracking resolution at the mask is roughly 2 mm in either direction. At the drift chambers, we require that tracks do not pass through the "outer" edges (the definition of which varies from chamber to chamber). Tracks are required to be a certain distance away from each other at each chamber plane, to avoid problem events. A "Wire Centered Cell" is defined as the hexagon, delimited by the high voltage wires, and centered in the sense wires, see Figure 4.4. The separation requirement is that track cells are at least 3 cells apart. This is the most natural way to avoid hits from two different tracks being captured by the same sense wire. The cell separation cut eliminates a substantial amount of events, particularly at drift chamber 1. Roughly 18% of the data is eliminated by this cut. At the calorimeter, tracks are required to be separated by at least 6 cm in the X direction and 3 cm in the Y direction, and the actual distance between tracks is required to be at least 20 cm. They are also required to be at least 2 mm away from the Collar Anti (the beamhole edge veto counters) and 2.9 cm away from the Cesium Iodide Anti (the outer edge veto counter in the calorimeter).

For the π^0 , it is required that the photon's "seed" crystal not be at the boundaries of the array. Boundary crystals are those around the beamholes and the outer edges of the calorimeter. Photon clusters are *not* required to be separated at the calorimeter.
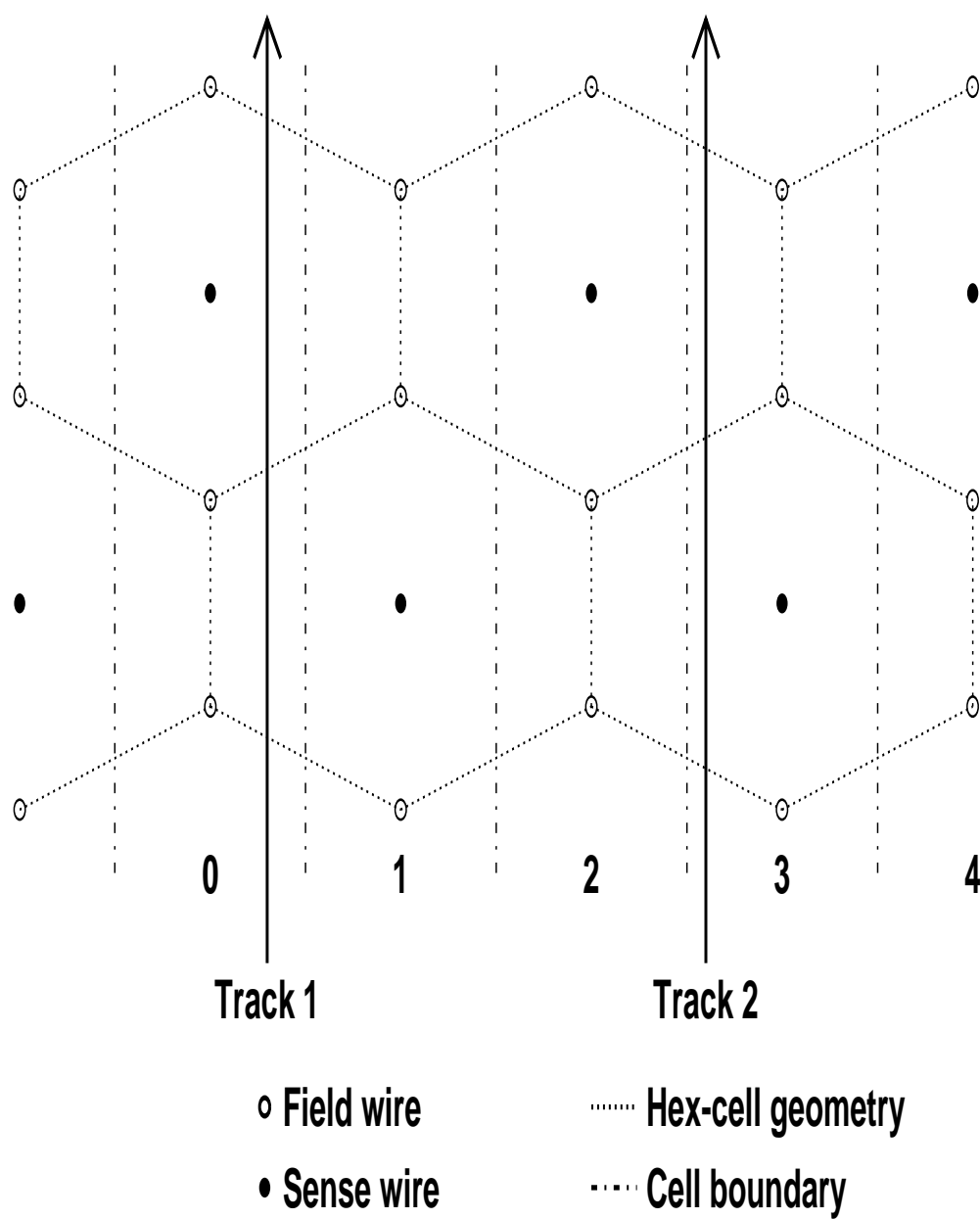
Figure 4.4: Cell separation cut diagram. These two tracks pass the cell separation cut.

Finally, we require the vertex to have 120 m$< Z_{vertex} < 158$ m. This region starts slightly upstream of the Mask Anti and extends down, almost reaching the Vacuum window.

4.7.4 Extra Particle Cuts

Only two tracks are allowed in each event. However, extra calorimeter clusters are allowed, as there can be satellite clusters from pions hitting the trigger hodoscopes. Additionally, no extra $\gamma\gamma$ pairs are allowed. An "extra pair" is found if an extra photon cluster is such that its Shape χ^2 and Timing χ^2 are within our cut constraints (50 each), and its pairing with any of the other two photons results in an invariant mass between 0.125 GeV and 0.145 GeV.

4.7.5 Track Quality Cuts

There are two indicators of good tracks: "Offmag-χ^2", which is a measure of how well the tracks match at the magnet's kick plane; and "Vertex-χ^2", which is a measure of the quality of the vertex (based on the uncertainties resulting from chamber hit topologies and the intrinsic resolution). These cuts are set at 500 and 100, respectively, which is very loose and don't have any effect (as we determined from the systematic studies).

4.7.6 Photon Quality Cuts

Photon energies are required to be at least 3 GeV. This is done because there are small differences between data and simulation for lower energy photons, so it is safer to cut them away. It is important to mention that this cut is only applied to those photons that form a good pair, i.e. have an invariant mass close to the π^0 mass. Extra clusters such as those coming from radiative events are not required to have $E > 3$ GeV. Additionally, a "Shape-χ^2" cut is applied. This quantity is a measure of the photon cluster energy distribution, and is useful to reject events were an extra photon overlays onto a π^0 photon cluster. In $\pi^+\pi^-\pi^0$ events, this can only happen with either a radiative or an accidental photon. The cut is set very loose at 50. Lastly, a "Timing-χ^2" cut is applied, at a value of 50. These two cuts are extremely loose, and they have no effect on the measured parameters, as determined in the systematic studies.

4.7.7 Pion Identification Cuts

An E/p cut of 0.85 is applied to the charged tracks. The MIP cut previously described makes this cut irrelevant since we do not have low momentum charged pions in our sample. However, since an $E/p < 0.9$ cut is applied in Level 3, we decided to leave this cut in.

4.7.8   Kinematic Cuts

The most important kinematic cuts we apply are the constraints on the invariant masses of the system

$$0.488 \; GeV < m_{\pi^+\pi^-\pi^0} < 0.508 \; GeV, \quad 0.130 \; GeV < m_{\gamma\gamma} < 0.140 \; GeV. \quad (4.4)$$

These two requirements by themselves make for a very clean $\pi^+\pi^-\pi^0$ sample. Additionally, the transverse momentum is required to be $P_t^2 < 2.5 \times 10^{-4} GeV^2$. Figure 4.5 shows the mass distributions obtained in data.

Additionally, the total energy of the kaon is required to be in the 40-160 GeV range. The charge track momentum is required to be at least 10 GeV. This is done to avoid the $8 - 10 \; GeV$ momentum region, where the MIP efficiency varies considerably, as will be discussed in Section 6.1.

4.7.9   Kinematic boundary in the Dalitz Plane

Figure 4.7 shows how the data populate the Dalitz X, Y plane. The boundary regions correspond to kinematic limits of the Dalitz variables. Any resolution discrepancy between data and simulation is prone to be enhanced at these edges. For this reason, we "mask" out these edges, keeping only the data inside the grid in Figure 4.7. Figure 4.8 is a lego plot of the same distribution, with the mask applied. The mask cuts away roughly 17% of the data.

4.8   Backgrounds

As mentioned previously, the stringent double mass constraint requirements make this a very clean sample. It is extremely unlikely that these requirements would be met by any other but $\pi^+\pi^-\pi^0$ decays. Still, we could have some absorber or collimator scatter background present. By extrapolating the exponential tail in Figure 7.13 to the signal region, we estimate the level of background to be 0.16%. The effect of the background on the fitted Dalitz parameters has been studied in the systematics (Chapter 7) and found to be negligible.

4.9   Final Analysis Cuts

Table 4.1 summarizes the final analysis cuts. All these, except for the "MIP" cut, were applied to the Monte Carlo generation as well, which will be discussed in Chapter 5. Table 4.2 shows the final sample sizes for data and Monte Carlo.
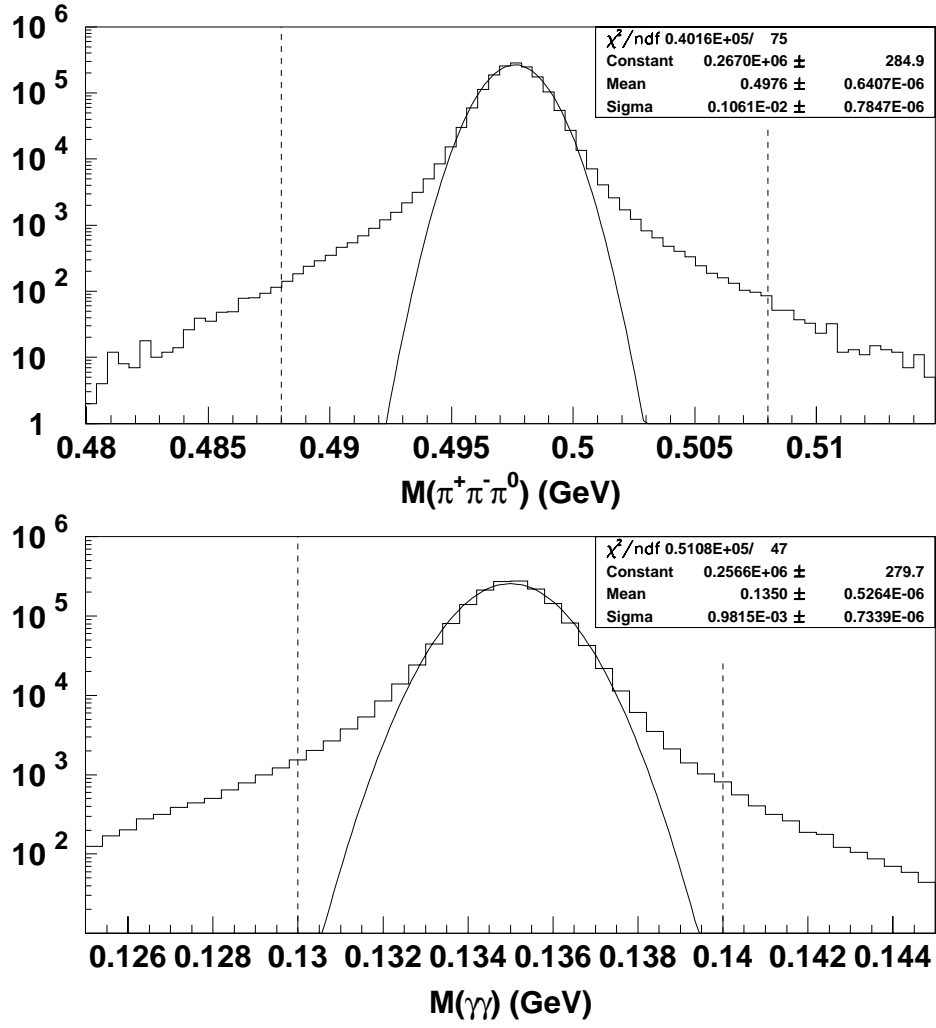
Figure 4.5: Invariant mass distributions for $\pi^+\pi^-\pi^0$ and $\gamma\gamma$ in data. The dashed lines indicate where the nominal cuts are made.
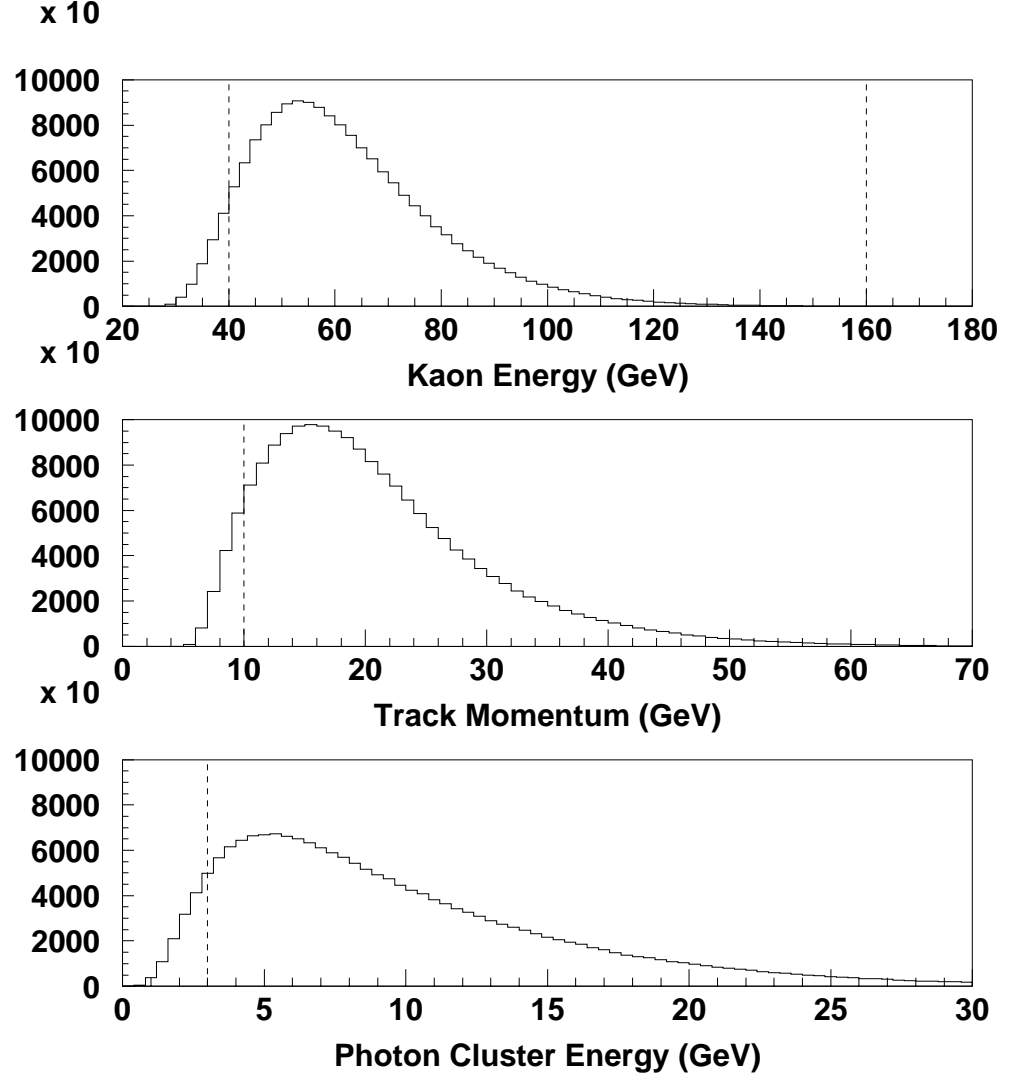
Figure 4.6: Kaon energy, track momentum, and photon cluster energy distributions in data. The dashed lines indicate analysis cut values.
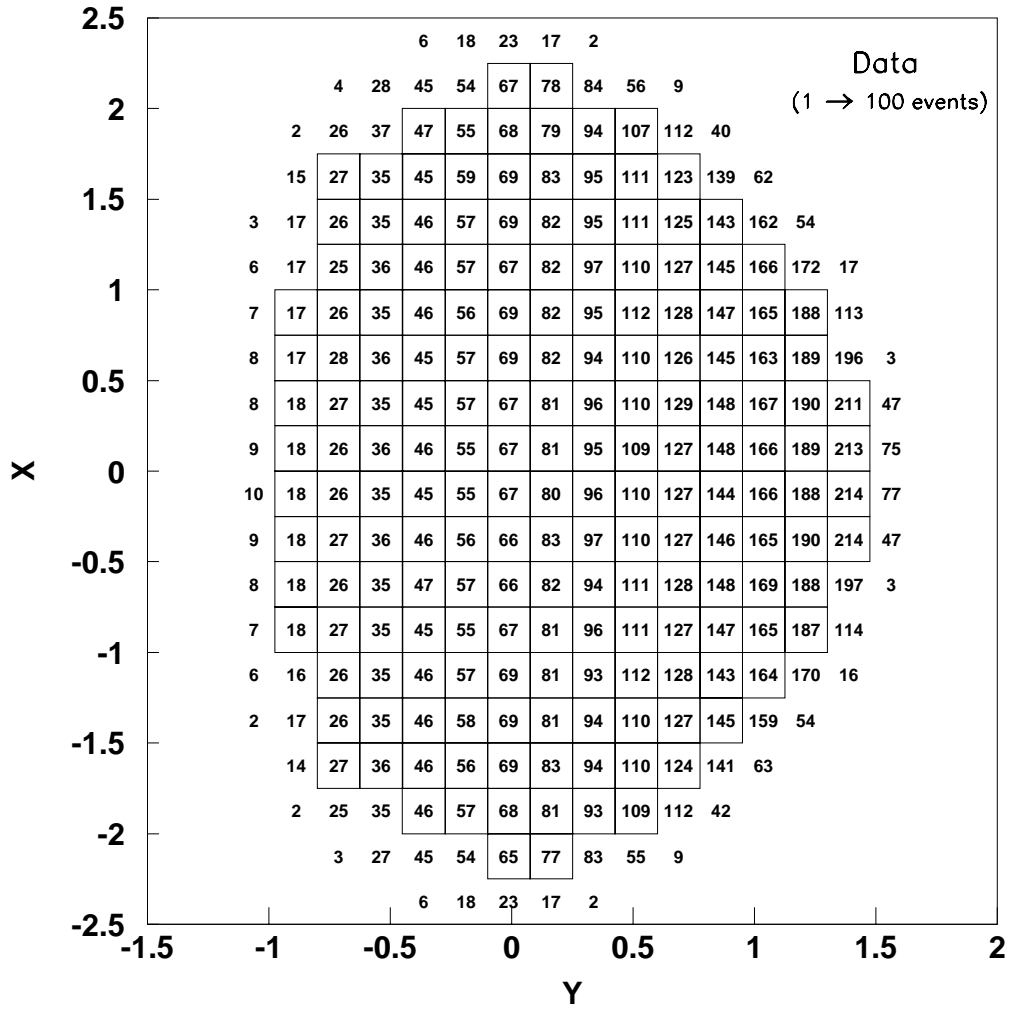
Figure 4.7: Dalitz plane distribution of data points. The grid represents the "mask" used to select the bins for the nominal measurement.
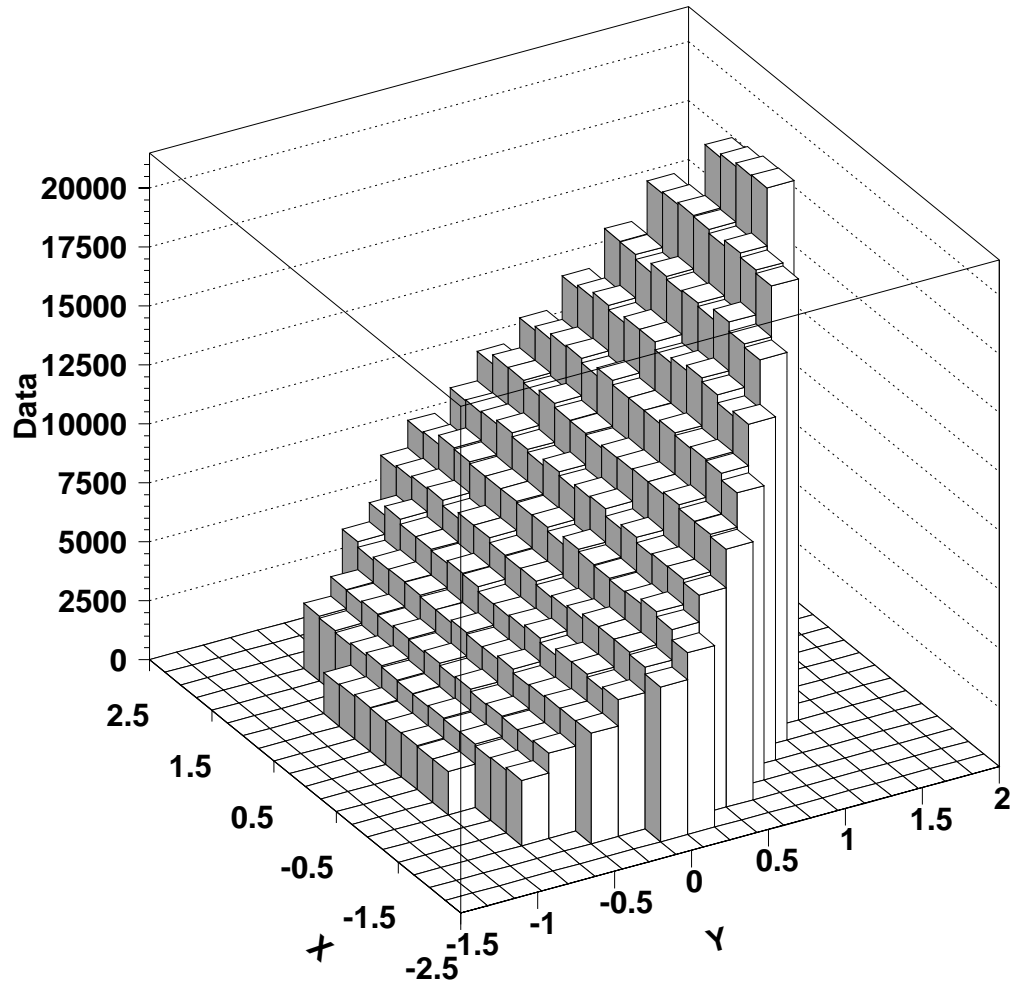
Figure 4.8: Dalitz plane distribution of data points, lego plot. Same plot as in Figure 4.7, with the points around the boundary removed (i.e. including only points selected by the mask.

Z vertex window	$120.0 - 158.0$ m
Total energy	$40.0 - 160.0$ GeV
Total $P_{t,tot}^2$	$< 2.5 \times 10^{-4}$
Vertex χ^2	< 100.0
Offmag χ^2	< 500.0
Number of tracks	2
Minimum track momentum	10.0 GeV
E/p for the tracks	< 0.85
Track cluster energy cut ("MIP" cut)	$< 1.0 GeV$
Minimum X separation b/w tracks at CsI	6 cm
Minimum Y separation b/w tracks at CsI	3 cm
Minimum distance b/w tracks at CsI	20 cm
Minimum γ cluster energy	3.0 GeV
Timing χ^2	< 50.0
Shape χ^2	< 50.0
Minimum separation b/w tracks & photons	25 cm
$\gamma\gamma$ invariant mass window	$0.130 - 0.140$ GeV
Veto cuts (VT0832)	charge mode (see text)
Fiducial cuts (FID832)	charge mode (see text)
CsI boundary cut	all crystals in boundaries
$\pi^+\pi^-\pi^0$ invariant mass window	$0.488 - 0.508$ GeV
Number of extra $\gamma\gamma$ pairs	0
Cut on kinematic boundary	mask (see text)

Table 4.1: Final selection cuts. Effect of cuts on the measured Dalitz parameters was included into systematic uncertainty (see Section 7).

	Data	MC (v 5.06)
Final sample	1.62M	3.05M

Table 4.2: $\pi^+\pi^-\pi^0$ event yields in data and Monte Carlo.

CHAPTER 5
DETECTOR SIMULATION

The KTeV Monte Carlo is a computer program which simulates kaon decays and the response of the KTeV detector in considerable detail. It simulates decays with the same energy and Z distributions as the data, and produces output that looks essentially the same as real KTeV data, with a few extra data banks added to the event format to store information about the original generated quantities, which can be used for special studies. The Monte Carlo events are analyzed as if they were data, with the same reconstruction algorithms and analysis cuts, except for the MIP energy cut, which we will describe in Section 5.7.

The main use of the Monte Carlo simulation is to determine the acceptance of our detector, i.e. the fraction all the possible $\pi^+\pi^-\pi^0$ decays we actually reconstruct. There are essentially two parts to the acceptance: geometrical, defined by the apertures and geometrical selection cuts (e.g. particle separation cuts at various detector systems); and detector efficiencies (the probability that a hit would be lost in a given device). The Dalitz parameter measurement is directly dependant on acceptance, there is double ratio cancellation, so it is extremely important that we simulate the detector as accurately as possible.

The Monte Carlo simulation is also important for determining the effect of systematic uncertainties on the measured parameters.

5.1   Kaon Generation

The MC can generate a wide variety of kaon and hyperon decay modes. We will use the $K_L \to \pi^+\pi^-\pi^0$ decay mode for our measurement, to which we will add radiative events using the PHOTOS [19] package.

5.1.1   Kaon Production

Simulation of an event begins by choosing a beam (left vs. right, and vacuum vs. regenerated) and an initial kaon eigenstate (K^0 vs. $\overline{K}^0$) [1]. Next, the kaon energy and production angle, relative to the primary proton beam, are chosen from a combined distribution. This distribution was motivated by a parametrization by

---

[1]See Appendix A for a brief phenomenological description of the neutral kaon system.

Malensek [20] of measurements of K^+ and K^- production by 450 GeV protons incident on a beryllium target [21]. Using the valence quark content of the incident proton as a guide, the forward production of neutral kaons is assumed to be related to charged kaon production as follows:

$$K^0 \sim (K^+ + K^-)/2, \qquad \overline{K}^0 \sim K^-. \qquad (5.1)$$

The energy distribution given by this parametrization is modified by a polynomial correction adjusted to match the distributions observed for $K_L \to \pi^+\pi^-$ decays from Vacuum beam data. This correction is within $\pm 8\%$ of unity across the whole energy range (40-160 GeV). The KTeV neutral beams (after collimation) includes a range of production angles, from 4.55 mrad to 5.05 mrad. The production model predicts a variation of the flux and energy distribution over this range, and such variations are observed in the data.

5.1.2   Kaon Transport

The kaon is assigned an initial position within the production target, with the transverse distribution based on the size of the primary proton beam and an exponential distribution along the length of the target based on the proton and kaon interaction cross sections in Beryllium. The kaon is then propagated downstream toward the detector. It first passes through the absorbers. There is a chance of scattering in the absorber, in which case the kaon is given a transverse momentum chosen from an exponential distribution before continuing downstream. The kaon is evolved from the initial K_0 or $\overline{K}_0$ states onto the two hamiltonian eigenstates K_S and K_L. A very small amount of K_S is left as we reach the decay region, except at very high energies.

5.1.3   Kaon Decay

The kaon is forced to decay within a certain region of the detector, bigger than the region selected for our measurement. The Z position for the decay is chosen from the expected distribution for the energy of the generated kaon. This includes an interference term between the K_S and K_L, but since there are so few K_S left by the time the fiducial region is reached, this is not an issue here.

The $K_L \to \pi^+\pi^-\pi^0$ decay is modelled using the PDG-1994 [22] form factors. A momentum configuration for the decay is picked based on the Dalitz distribution given by

$$|\mathcal{M}|^2 = 1 + 0.67Y + 0.079Y^2 + 0.0098X^2, \qquad (5.2)$$

where X and Y have already been defined in 1.4. To this event we add a radiative component using the PHOTOS [19] package.

After the decay products have been generated in the kaon rest frame, they are boosted to the lab frame based on the generated kaon energy and direction.

5.1.4   Tracing the Decay Products

The products of each kaon decay (except neutrinos) are traced through the KTeV detector in sections. A charged pion is permitted to decay to $\mu\nu$ according to its lifetime, and the muon is traced through the remainder of the detector. Charged particles receive a transverse momentum kick from the analysis magnet, based on a field-integral map which is a function of the transverse position of the particle at the center of the magnet.

Charged particles undergo multiple scattering as they pass through the vacuum window and the material in the spectrometer, with a GEANT-based parametrization of a non-Gaussian scattering component. Photons are permitted to convert into e^+e^- pairs.

Energy deposit in the photon-veto detectors and trigger hodoscope counters is simulated during tracing. Depending on the trigger configuration in use, sufficient energy deposit in a photon-veto detector can cause the event to be rejected immediately, saving CPU time when simulating backgrounds with extra photons.

A particle (other than a muon) which hits a photon-veto detector or some passive material, or any particle which escapes the detector volume, is no longer traced. The user can specify that an event should be rejected immediately in such a case, which can conserve CPU time when a physics signal mode is being generated.

The Monte Carlo stores the position of each particle at the drift chambers and calorimeter for more detailed simulation later, as described in the sections below. Tracing ends when a particle hits the calorimeter or the Back Anti, except for muons, which are propagated through the downstream material (calorimeter and steel muon filters) in a separate step.

5.2   Drift Chamber Simulation

The basic approach would be to calculate the distance to the closest wire in a given sense plane and convert this to a drift time using the inverse *time vs. distance* relationship measured in data. There are, however, a number of corrections that need to be applied to this procedure. The original reason for this is the discrepancy in the "Sum Of Distance" (SOD) distributions that had been observed between data and Monte Carlo.

The high-SOD probability, i.e. the fraction of events where the SOD is higher than the cell size, was observed to be higher in data compared to the Monte Carlo simulation. In essence, the high-SOD problem stems from the fact that the drift chamber system is not sensitive to the signal produced by *one* drift electron, as we already explained. A track leaves a trail of ionization electrons in the gas, which

are separated by a certain distance according to a Poisson distribution. For tracks far away from the sense wire, most ionization electrons will arrive at the wire in a relatively short time interval, giving a well defined, sharp pulse. For tracks very close to the wire, the first drift electron arrives very soon in time, with the other electrons trailing behind. This produces a different pulse shape, much broader than the one from far away tracks. In principle, this is built into the *time vs. distance* relation, as it is measured from data. However, since there are *discrete* electron contributions, the pulse shapes from close tracks are not smooth, they exhibit a structure given by the time differences with which electrons are collected by the sense wire. This results in a broader distribution of possible trigger times, and increases the probability to get a high SOD considerably. This has been modelled in the Monte Carlo in the form of a "threshold curve", which gives the triggering threshold as a function of the high-SOD rate [23] measured in data. We also mentioned the position dependance of the high-SOD probability, for which maps can be derived from data as well. These give the high-SOD probability as a function of the wire and the position along the wire. It has been observed that these maps show points along the wire where the high-SOD rate is particularly high, probably corresponding to local defects along the wire, or deposits of some sort.

The drift chamber simulation also includes a model for generating a "delta ray" above a certain cutoff energy, which can produce an extra hit on a wire. This hit may arrive before the hit from the original particle, causing the drift distance to be underestimated when the event is reconstructed.

Finally, the Monte Carlo models the response of the discriminator cards to multiple pulses on a wire. This is important because an "accidental" hit before the beginning of the in-time window can obscure the hit from the simulated particle. The discriminators were designed to have a deadtime of about 50 ns, although lab measurements show that the deadtime was more like 46 ns (i.e. 92 TDC counts), falling exponentially after that. Sometimes a hit can prevent retriggering for an even longer period of time, presumably due to a particularly broad analog pulse which stays above the discriminator threshold longer than expected.

5.3   Calorimeter Simulation

The high precision of the Cesium Iodide calorimeter demands a very accurate description if its response. The main component of the calorimeter simulation are the shower libraries. These are generated using the GEANT package [24], which simulates all relevant interaction processes in the Cesium-Iodide. This is done in the form of a shower library instead of direct GEANT simulation because doing it event-by-event would be extremely taxing in terms of CPU time.

5.3.1   Photon and Electron Showers

A library of 13×13 small crystals (each 2.5 cm×2.5 cm in size) is used to simulate the calorimeter response to photons and electrons. The showers are generated at six incident energies (2, 4, 8, 16, 32, and 64 GeV) and 325 incident positions (within the central crystal in the 13×13 array). The information for each shower includes the energy deposited in each crystal, as well as the longitudinal profile of the energy deposited for the central 7×7 region (collectively) and the four crystals with the most energy (individually).

The Monte Carlo selects a shower based on the incident position and energy. It "interpolates" between the discrete shower energies in the library by randomly selecting a shower with lower or higher energy than the actual particle energy, using weights calculated from the logarithms of the energies; thus, the mixture of Monte Carlo showers used is a continuous function of the energy of the incident particle . For purposes of selecting a shower for a particle incident at an angle, the transverse position is calculated at an appropriate depth within the crystal, roughly the energy-weighted mean depth of the shower but with a correction determined from a study of electrons incident at significant angles.

5.3.2   Pion Showers

A separate library is used to simulate pion showers. It was generated using GEANT with the FLUKA package for hadronic interactions. A 41×41 small crystal array is used in this case, which is considerably bigger than the photon case as pions can generate big hadronic showers. Interactions with the hodoscope banks, which are 2 m upstream of the calorimeter face, are simulated as well. The incident pion positions are chosen randomly in the upper right quadrant of the central crystal, and classified according to a 3×3 grid (all other incident positions can be obtained by suitable reflections along the vertical and horizontal axis). The momentum distribution used is that from $Ke3$ decays. The information for each shower includes the energy deposited in each of the 1,641 crystals as well as the type of primary interaction, and whether hadronic secondaries were produced. The library has a total of about 900,000 shower events, separated in records with approximately 3,200 events each.

In the charged pion case, the Monte Carlo select a shower based on the position of the incident particle at the central crystal and its momentum. To pick a shower, we first determine the position of the incident pion within a 3×3 grid in the upper right quadrant of the central (seed) crystal. We then smear the incoming pion's momentum by a gaussian function of width 5% the momentum. Finally, we pick that shower whose position is within the same 3×3 cell in the upper right quadrant and with the momentum closest to the smeared one we just obtained. Shower energies are scaled by the ratio of the actual incoming momentum to the smeared one used to pick the shower. The density of shower events, per record, is such that,

in most cases, the discrepancy between the pion momentum and that of the shower is less than 1 GeV.

In our analysis, we needed to modify the way these showers are picked because of the MIP selection we require in data. This will be explained in detail in Section 5.7.

5.4   Veto Counters Simulation

Energy deposit by photons in the Mask Anti, Ring Counters, and Spectrometer Antis is simulated with an energy-dependent Gaussian resolution, parametrized from data. There is a fixed resolution for minimum-ionizing particles which varies from about 30-40%, depending on the counter.

Muons are traced through the steel muon filters and will reach the muon veto hodoscope unless they are stopped in the steel. Energy loss in the steel is modelled as Bethe-Bloch ionization loss, with Landau fluctuations from a parametrization determined from studies with GEANT. We expect the simulation to do a reasonably good job of reproducing the probability of a muon to be stopped as a function of energy.

5.5   Accidental Overlays

Given the high flux of kaons and neutrons in the KTeV detector, it is natural to expect some amount of underlying activity in the detector. Stray particles from upstream hyperon decays, particles produced in the Regenerator, cosmic rays, and other sources produce some underlying activity that sometimes does not trigger the veto counters. This can lead to misreconstruction of tracks or increase the energy in the calorimeter clusters.

We study this effect by "overlaying" an accidental event from the accidental trigger on top of our good event. The accidental energies in detector elements are added to the event's energy, and the extra drift chamber hits are incorporated in the event. It is important to note that the accidental trigger is proportional to the instantaneous beam intensity in order to eliminate possible biases.

5.6   Trigger Simulation

The Monte Carlo simulates the behavior of all of the trigger elements, including the hit-counting system (Banana and Kumquat modules), Y Track Finder, and HCC. The hit-counting and YTF models are rather robust since their behavior depends on digital information from the drift chambers, with only a few minor subtleties having to do with the timing of accidental hits.

The trigger decision is made using the same trigger definitions as were used on-line for the data collection. In fact, the same binary trigger-definition maps are

used in the Monte Carlo, with software performing the memory lookups which were originally done in hardware.

5.7   Generating MIP events in the Monte Carlo

We have chosen to use MIP charged pion events in our measurement to avoid hadronic showers in the calorimeter. This keeps the shower products from contaminating the photon clusters, and also reduces the need to simulate precise shower details. The standard way to pick a MIP event is to require that the energy of a cluster associated with a charged track be E_{CsI} <1 GeV, as we described already. Since we make this MIP energy cut in data, we ought to make the same cut in our Monte Carlo analysis. However, this presents a problem. Figure 5.1, top, shows a data over Monte Carlo overlay after applying a MIP energy cut to both data and Monte Carlo. The jumps that we see here are the combined result of both having a finite number of showers in each momentum bin *and* cutting on a shower parameter. During shower generation, the momenta are picked randomly from the $Ke3$ pion momentum distribution [2]. There will be a certain number of shower events that fall within each momentum bin in Figure 5.1. If we do not cut on any parameters associated with the showers (e.g. the energy deposited in the calorimeter), this momentum distribution will be continuous. However, if we cut on the shower energy, we will cut slightly different amounts of events in consecutive track momentum bins. This is because we have a finite number of showers in each bin, and it is most likely that a slightly different number of showers will pass the cluster energy cut in consecutive bins. The relative difference in the number of showers that pass the cut in consecutive bins is exactly the size of the jumps in the track momentum distribution. To get around this problem we modified the way a pion shower is picked from the library. This is done in three steps:

1. Select a shower by picking a gaussian-blurred momentum around the generated pion momentum (the width of this gaussian distribution is chosen to be 5% of the incident pion momentum);

2. Require that the energy the shower deposits in the central 3×3 blocks cluster, $E_{3x \times 3}$, be less than 1 GeV;

3. If $E_{3 \times 3}$ >1 GeV, go back to the first step and pick a new shower.

The effect of this modification is seen in Figure 5.1, bottom plot. The key to the solution is not to cut on shower energy in the Monte Carlo analysis since the Monte

---

[2]We use this distribution instead of a flat distribution to maximize the density of showers in the most likely region for pion momenta. This does not bias the momentum distribution for $\pi^+\pi^-\pi^0$ events, as the momenta are picked by Monte Carlo during generation, independently of what the shower momentum density is.

Carlo is already a MIP sample by construction. The statistical effect just described also appears (to a lesser degree) when we apply an E/p cut in Monte Carlo. The magnitude of the effect is much smaller because only a very small fraction of shower events will have $E/p > 0.85$. In this case the solution is also not to apply an E/p cut to the Monte Carlo sample, which is fine since there is no $Ke3$ background to reject anyway.

5.8 Acceptance in the Dalitz Plane

We generated ten million $K_L \to \pi^+\pi^-\pi^0$ Monte Carlo events for this analysis. The events were generated requiring that the charged pion energy deposited in a 3×3 grid, centered at the crystal hit by the pion, be less than our MIP cut, as was explained in Section 5.7. Figure 5.2 shows the acceptance at different stages of the simulation. We can see that the average Monte Carlo acceptance is about 6% on average. However, this does not include the effect of the MIP cut applied in data since this cut is not applied to the simulation. Since the probability that a $\pi^+\pi^-\pi^0$ event is MIP is about 11%, the acceptance in data, as deduced from this Monte Carlo estimation, should be about 0.6%. This is in good agreement with the ratio of final events to raw events in data (1.62 M events compared to 224 M events in the split tapes, which gives roughly 0.7% acceptance).
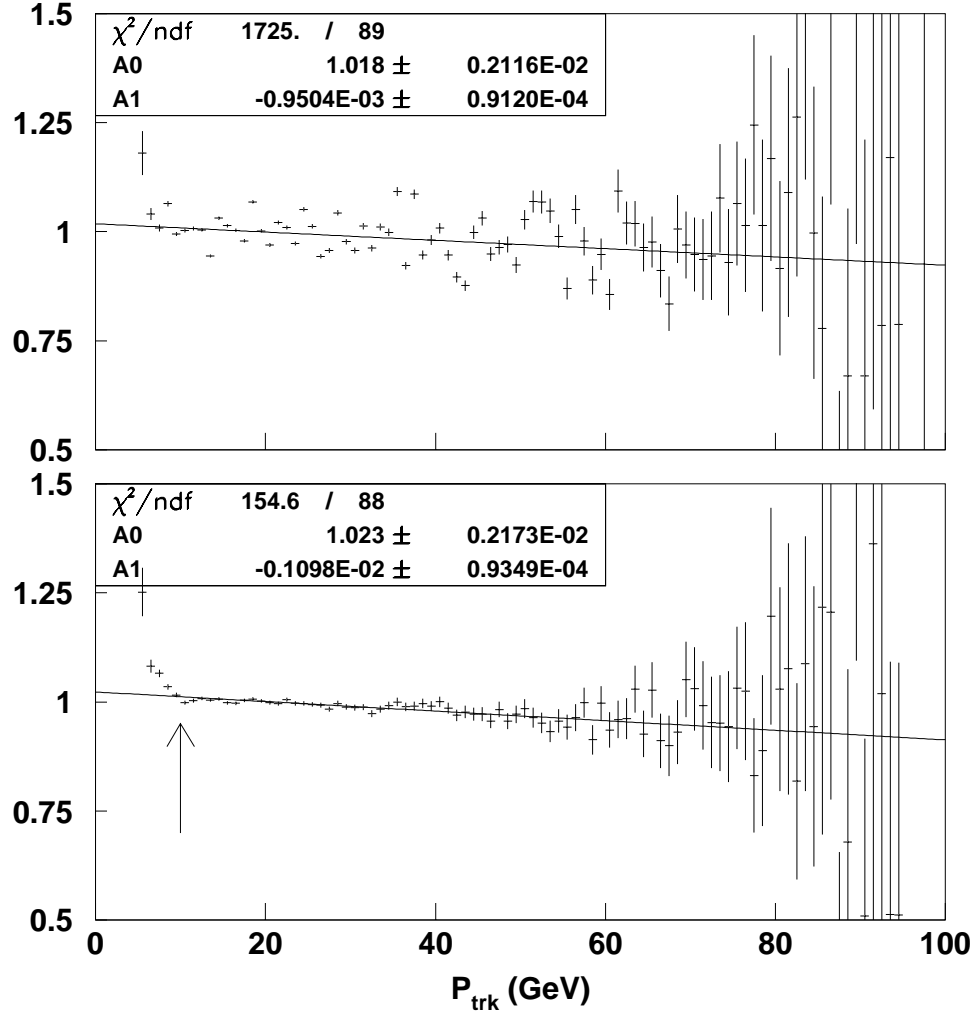
Figure 5.1: Track cluster energy cut in Monte Carlo. Top: Data over Monte Carlo ratio plot using the standard shower library code. Bottom: The same distribution after the modification described in Section 5.7. It is important to mention that this is a single-entry plot, i.e. it is filled by randomly selecting only one of the two tracks in the event. Note the rise at low momentum: we see this same feature in our data MIP efficiency, but we chose not model it since the gain in data points is rather small. For this reason we cut at $10 GeV$ (arrow).
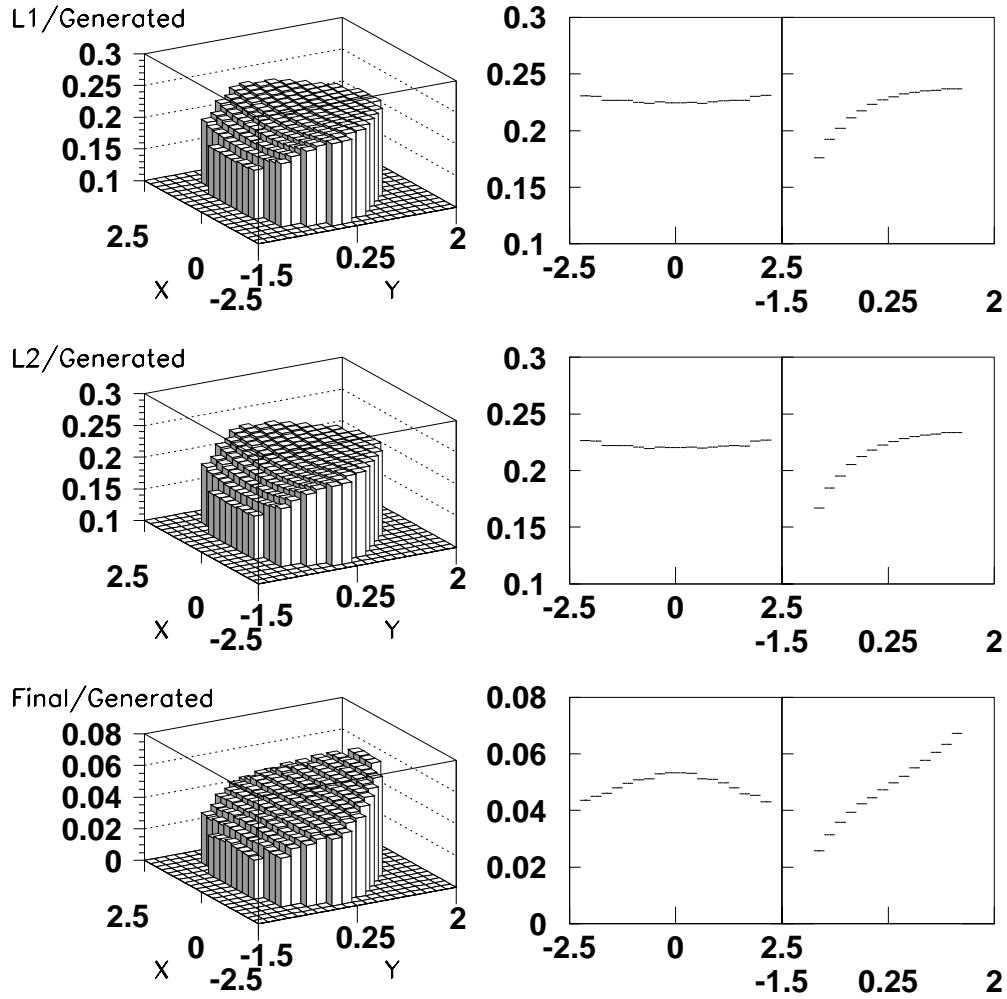
Figure 5.2: Detector acceptance after the different stages of event processing. Top: After Level 1 the acceptance is similar to $\pi^+\pi^-$. Only the charged tracks are required at this stage. On the right we have X and Y projections of the 2D distributions. Middle: Level 2 does not produce much of a change in the number of accepted events. Bottom: Final sample and event selection requires a proper π^0 to be reconstructed, and that the invariant mass of the total system be close to the kaon mass. Note that no MIP selection is done here, as the Monte Carlo sample is forced to be MIP at generation level (see Section 5.7).

CHAPTER 6
DALITZ ANALYSIS

In this chapter we will get into some more detailed discussion about the main issues in our measurement of the Dalitz parameters.

6.1 Efficiency of Minimum Ionizing Particles in the Calorimeter

In the Dalitz measurement we require that the energy deposited in the calorimeter by charged pions be less than $1 GeV$. As previously mentioned, we do this to eliminate events where the charged pions showered extensively.

The probability that a charged pion will undergo hadronic interactions in the Cesium-Iodide can be measured in data. For a single pion, this probability is roughly 2/3, so the probability to be MIP is roughly 1/3. We expect this probability to be a function of the charged track momentum and the position of the track at the calorimeter. In particular, we expect a noticeable difference in the boundary between small and large crystals, as not only the crystals themselves, but the cluster algorithm is different in each case: for small crystals, the clusters are defined by a 7×7 grid, centered in the seed crystal, whereas for big crystals, the clusters are 3×3 in size, i.e. equivalent to a 6×6 small crystal grid.

To determine the probability for a single track to MIP, we used a data sample with no MIP energy cut, and determined the probability for a *single track* to deposit and energy $E_{CsI} < 1 GeV$. Figure 6.1 shows the measured MIP efficiency for single tracks at the calorimeter, as a function of the position and momentum of the charged pion. We studied the 2D distribution of efficiency in the calorimeter and found no feature mixing the X and Y position distributions in a non-trivial way. To include this efficiency in the Monte Carlo simulation, we determined the momentum and position dependance of the efficiency by the following procedure

1. Start with the P_{trk} slope;

2. Add the X position dependance (using a parabola for small blocks and a constant value for the big ones);

3. Compensate for the small remainder P_{trk} slope (caused by the position correction).

The first step involves incorporating the P_{trk} slope in the Monte Carlo efficiency, which has a value of $(9.0 \pm 1.4) \times 10^{-4}$ 1/GeV. Note that this slope is roughly three times bigger than the one quoted in the fit in Figure 6.1. This is because we apply a relative efficiency correction, normalized to one, instead of the absolute efficiency shown in the plot. Also note that the denominator corresponds to data with an E/p cut at 0.85. We cross-checked this slope with a sample with no E/p cut (from the B01RAN triggers) and found no discrepancy with this result, within statistics.

Figure 6.2 shows how the position dependance changes when we do this. This is because the outer regions of the calorimeter are preferentially illuminated by lower momentum particles. The next step is to correct for the position dependance, for which we used a parabola for the small crystal region, and a constant for the big crystal region. This produces a residual P_{trk} slope of $(0.65 \pm 0.4) \times 10^{-4}$ 1/GeV, which is 1.5σ away from flat, so we compensated for this effect. The final result of this is a flat distribution of the MIP probability as a function of both position and momentum in the calorimeter, as shown in Figure 6.3.

We will study the effect introduced by incorporating the MIP efficiency in the Monte Carlo when we study systematic effects.

6.2 Mass Constrained Vertex Reconstruction

One of the very nice characteristics of $K_L \rightarrow \pi^+ \pi^- \pi^0$ decays is that they are over-constrained. It is possible to use a mass constraint to reconstruct some of the kinematics based on some other kinematics. In fact, most of the previous determinations of the Dalitz parameters were not able to reconstruct the π^0 , and used these kinematic constraints instead. We will make use of these kinematic constraints to improve the reconstruction of the vertex position.

In standard tracking, the position of the vertex is reconstructed using the extrapolation of the charged tracks to a Z position that minimizes the distance between them. This is not a good method of reconstruction when tracks have small opening angles, particularly if the vertex is located in the upstream portion of the decay region. It would also render bad results if any of the charged particles scattered at the vacuum window.

To give an idea as to how this works, consider $\pi^+ \pi^-$ decays. It is possible to determine the Z position of the vertex if we know the magnitudes of the momenta and the position of the tracks at the vacuum window. From the kaon invariant mass relation, we have

$$
\begin{aligned}
M_K^2 &= (P_{\pi^+} + P_{\pi^-})^2 \\
&= 2m_{\pi^+}^2 + m_{\pi^+}^2 \left(\frac{p_{\pi^+}}{p_{\pi^-}} + \frac{p_{\pi^-}}{p_{\pi^+}} \right) + 2p_{\pi^+} p_{\pi^-} (1 - cos\theta) + O\left(\left(\frac{m}{p} \right)^4 \right),
\end{aligned}
\tag{6.1}
$$

where θ is the opening angle between the pions. Using this equation, if we know the
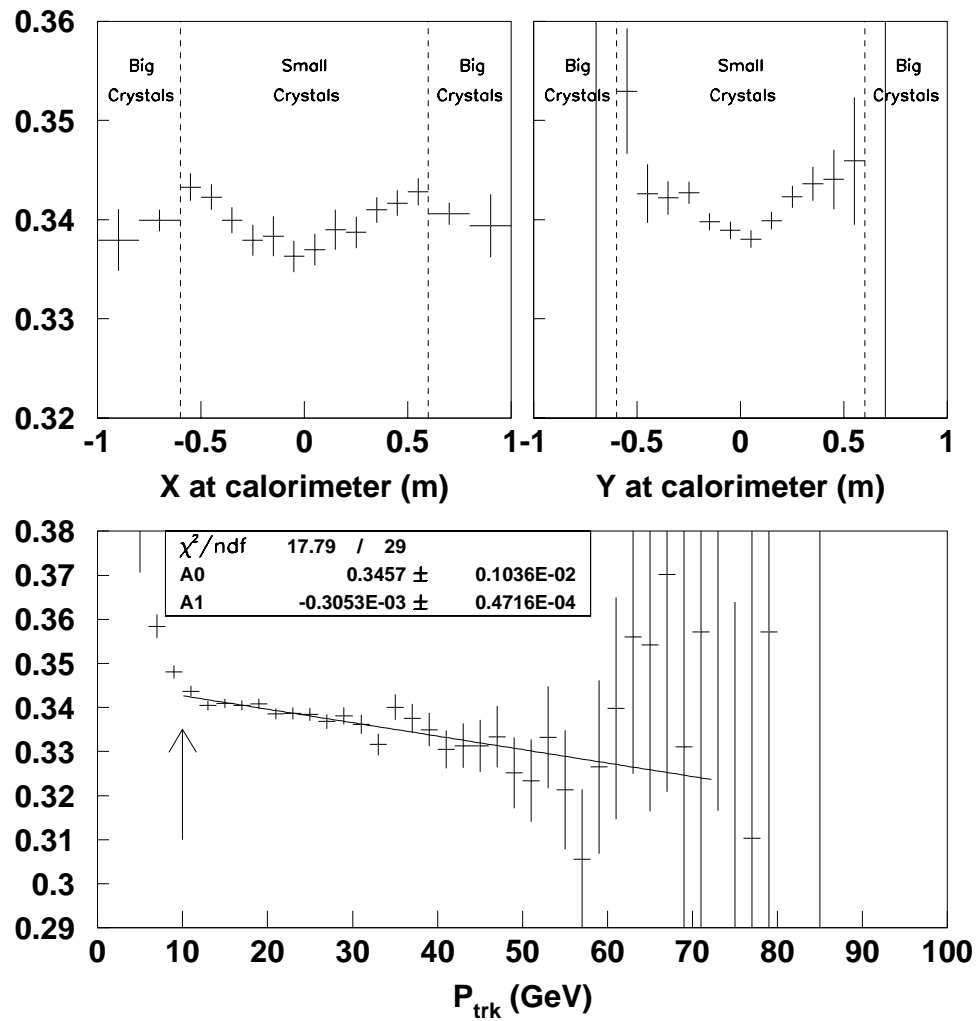
Figure 6.1: "Minimum Ionizing Particle" (MIP) probability in the calorimeter. Top: Single-track data MIP efficiency as a function of the X and Y positions of the track at the calorimeter, left and right respectively. Note the difference between small and large blocks. Bottom: Single-track data MIP efficiency as a function of track momentum.
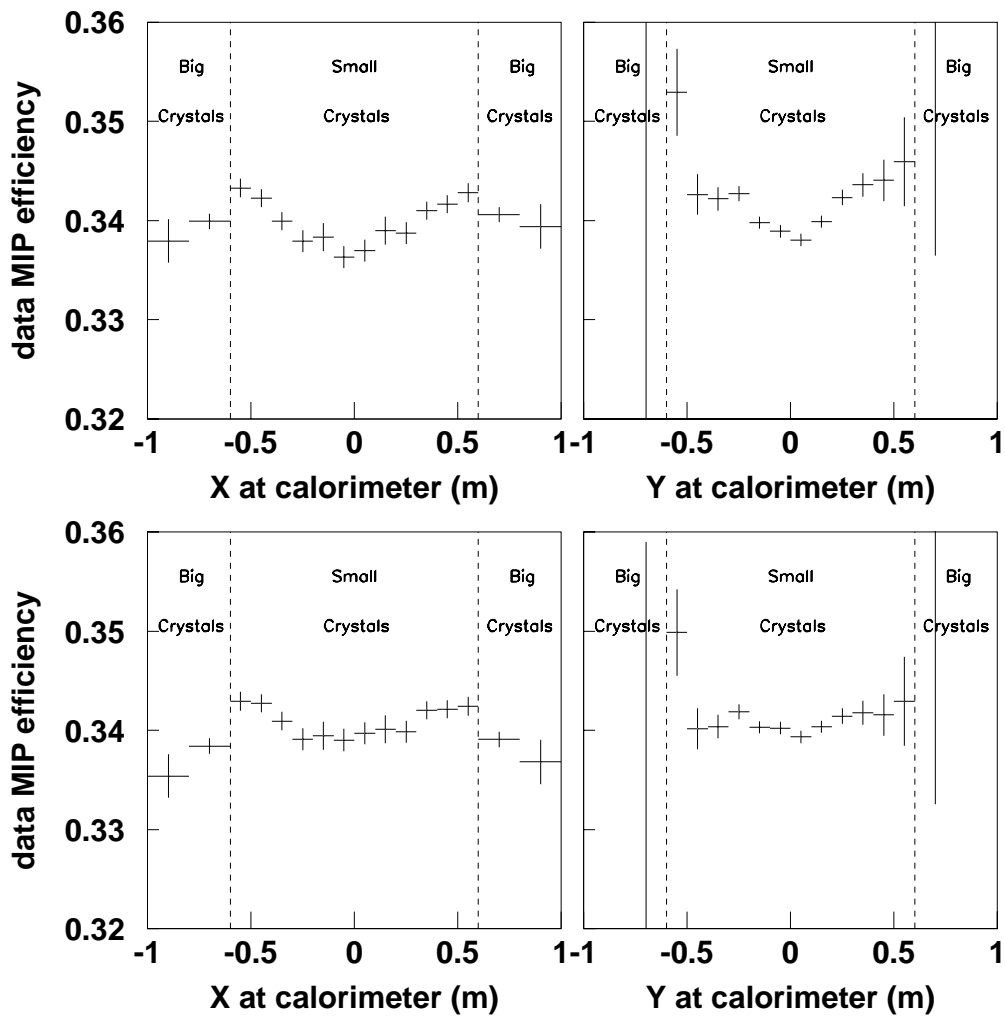
Figure 6.2: MIP probability change as a function of position in the calorimeter. Top: Single track data MIP efficiency as a function of the X and Y position of the track at the calorimeter, left and right respectively. Note the difference between small and large blocks. Bottom: Effect of compensating for the track momentum efficiency.
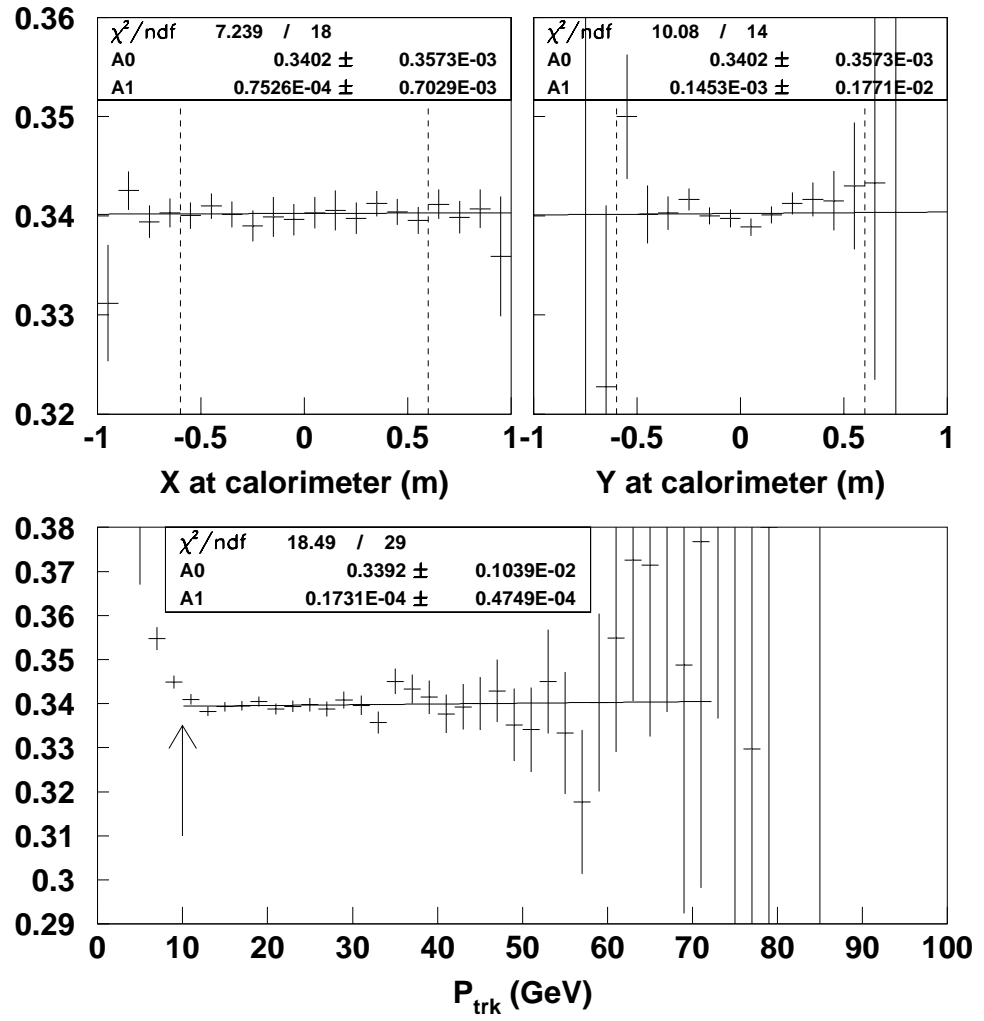
Figure 6.3: Final MIP distributions after efficiency reweighting. By reweighting the data distributions (event by event) by the MIP efficiency we determined, we can check whether the effect is compensated for. These distributions are, within statistics, flat.

momenta of the charged pions and the position of the tracks at the vacuum window, we can determine the Z position of the vertex.

For $\pi^+\pi^-\pi^0$ events, a similar mass constraint can be derived (the details are developed in Appendix C). It is slightly more complicated to impose the kaon mass condition because the point at which the π^0 intersects with the vacuum window is determined by the vertex position itself. We start with the vertex calculated using standard tracking. We then calculate the position of the π^0 at the vacuum window, and with that we calculate the new Z position of the vertex. This is iterated until the discrepancy between the two is less than $1\ mm$. The method converges very fast. Figure 6.4 shows the difference between generated and reconstructed Z vertex positions for both standard tracking and the mass constraint method. The result is that resolution is improved by a factor of two. One caveat of this method is that the mass constraint requires an accurate charged momentum measurement for the reconstruction of the vertex position. If there is a problem with momentum reconstruction, such as a scale problem, this method of vertex reconstruction can be biased. However, by the same token, even if there is a problem with momentum reconstruction, imposing a mass constraint gives the most physical reconstructed quantities, especially since the Dalitz variables Y and X are proportional to invariant masses $M(\pi^+\pi^-)$ and $M(\pi^+\pi^0) - M(\pi^-\pi^0)$, respectively. The effect of using the standard vertex reconstruction instead of this mass-constrained version is included in the systematic uncertainties.

After an optimal Z position of the vertex is found, we determine the best X and Y vertex positions. It is possible for a charged track to scatter at the vacuum window. To first order, this would alter its direction but not the magnitude of the momentum. In this case, the best X and Y position for the vertex would be given by the extrapolation of the *unscattered* track to the Z position of the decay. We consider three cases: the standard X, Y vertex position (the one given by standard tracking) and the ones obtained by extrapolating each track back to the Z vertex position. We then choose the best candidate based on which one has the smallest total P_t^2. Figure 6.5 shows the improvement of the resolution, from about $0.85mm$ to about $0.69mm$, about 20%.

6.2.1   Resolution of the reconstructed Dalitz variables

We can estimate the resolution of the Dalitz variables X and Y in the same manner that we estimated resolutions for the vertex reconstruction. Improving the vertex reconstruction would not mean much to us if it did not influence the resolution of the variables we use to fit the data. Figure 6.6 shows the improvement in resolution afforded by the mass constrained vertex reconstruction.
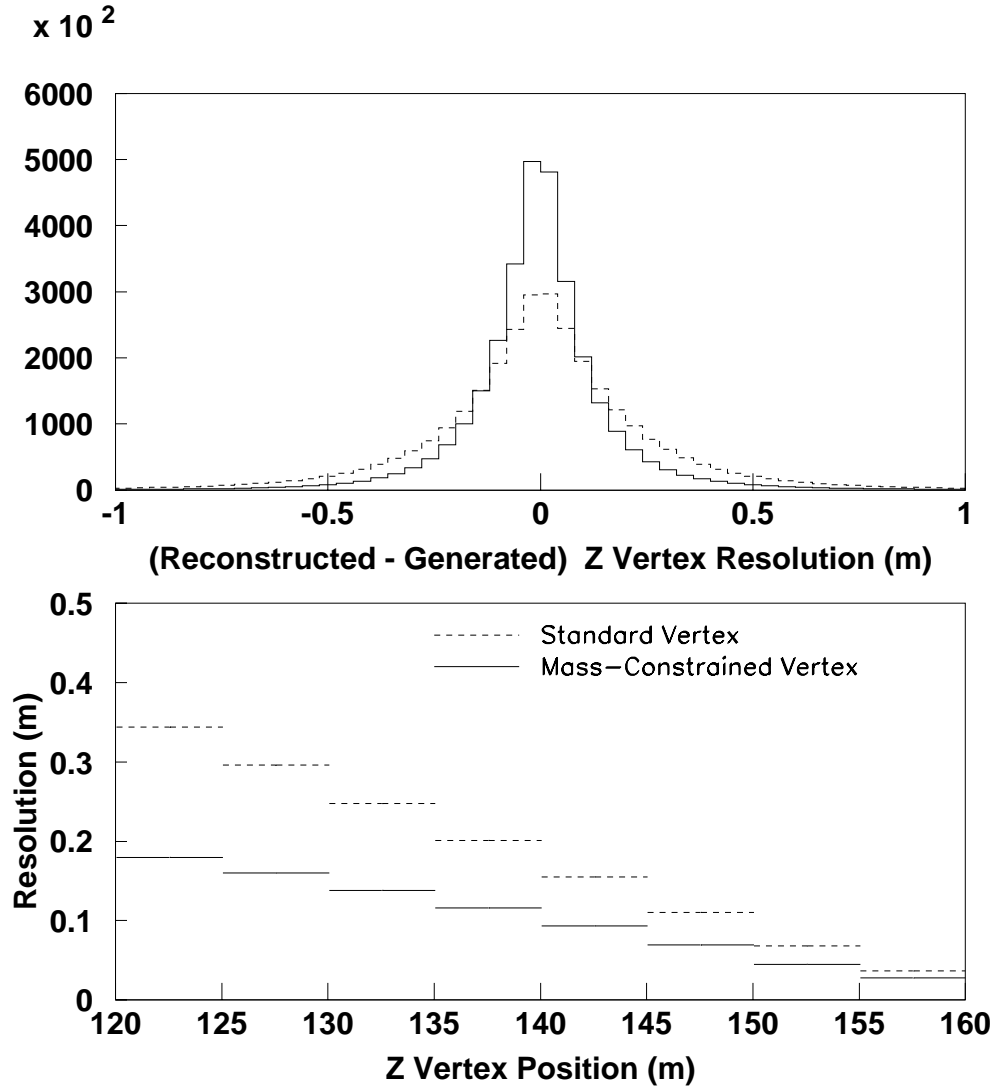
Figure 6.4: Z vertex position resolution, improved by using the kaon mass constraint. Top: Difference between reconstructed and generated Monte Carlo. Bottom: Resolutions as a function of position in the decay region. The improvement is more noticeable upstream, as those events have very small opening angles.

64
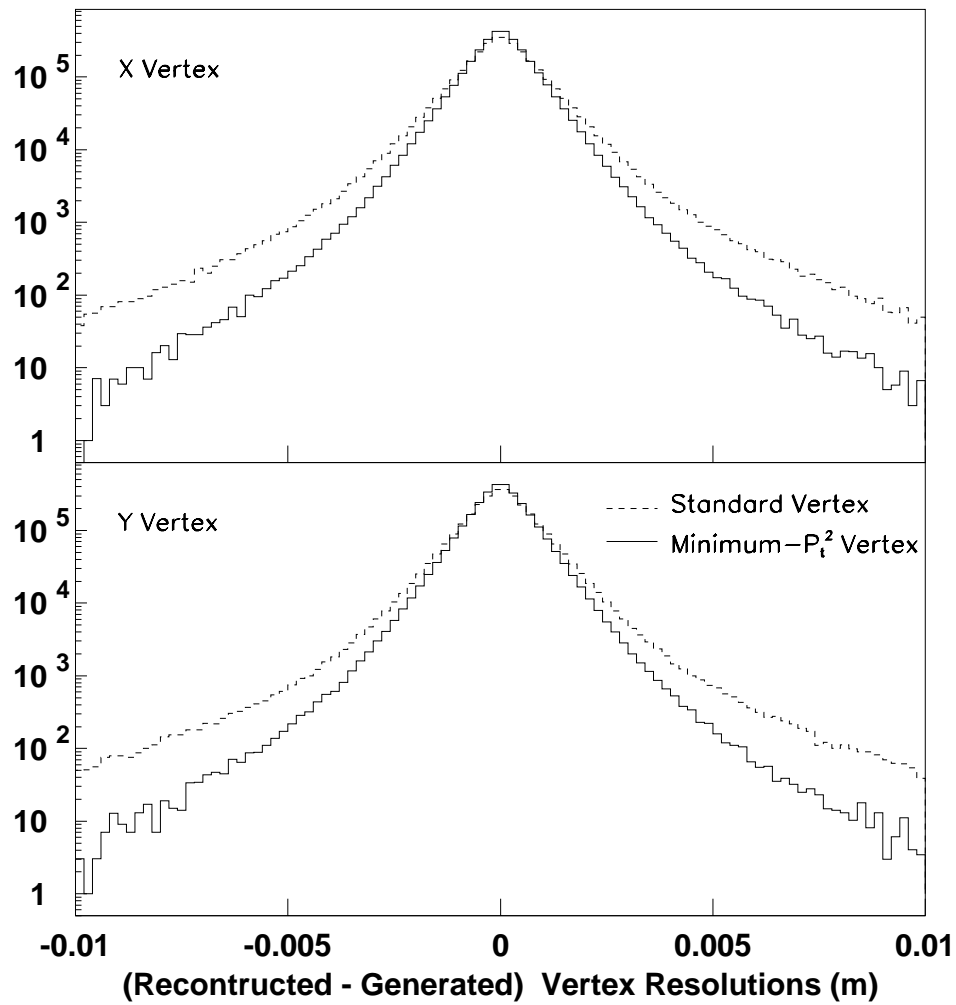
Figure 6.5: X and Y vertex positions resolutions. Plotted here is the difference between reconstructed and generated Monte Carlo vertex positions. The improvement is not as striking as in the case of the Z vertex resolution, but it is still quite noticeable.
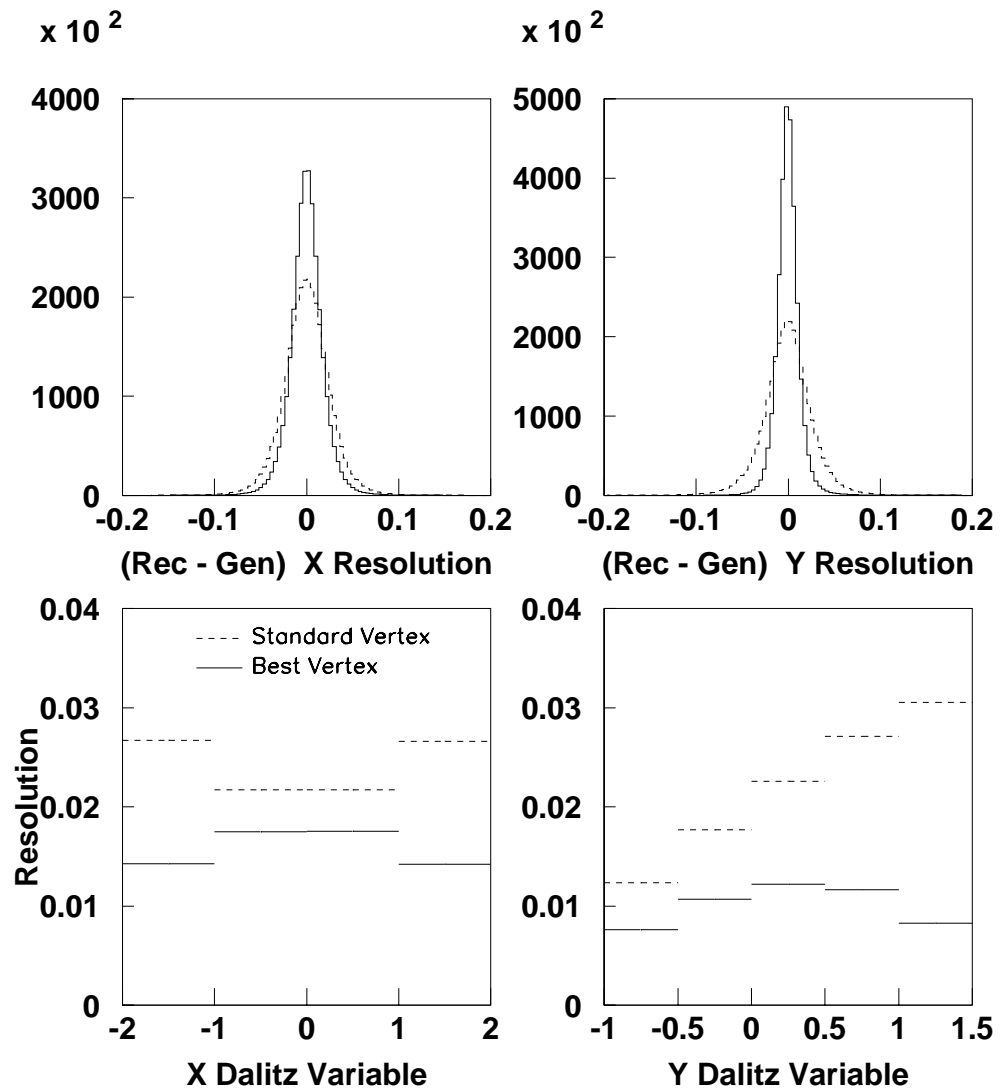
Figure 6.6: Dalitz variables resolution. Left (right) plot shows the difference between reconstructed and generated values of the Dalitz variable X (Y) as a function of the generated value.

6.2.2   Data resolution

It is very important for our measurement that we get accurate charged particle tracking information. It is also very important that resolution effects are simulated correctly. We already showed that the mass-constrained vertex improves the Monte Carlo resolution considerably. A good way to directly asses whether it also helps in data, is to calculate the "missing particle momentum" defined by

$$p_{\pi^0\|} = \frac{(m_K^2 - m_{\pi^0}^2 - m_{\pi^+\pi^-}^2) - 4m_{\pi^0}^2 - 4m_K^2 P_{t,\pi^+\pi^-}^2}{4\left(m_{\pi^+\pi^-}^2 + P_{t,\pi^+\pi^-}^2\right)}, \tag{6.2}$$

where $m_{\pi^+\pi^-}^2$ is the invariant mass of the $\pi^+\pi^-$ system, and $P_{t,\pi^+\pi^-}^2$ is the component of the $\pi^+\pi^-$ system's momentum, $P_{\pi^+\pi^-}$, perpendicular to the kaon direction. The quantity defined in Equation 6.2 is the component of the π^0 momentum along the kaon direction *in a reference frame where the $\pi^+\pi^-$ momentum is perpendicular to the kaon direction,* as shown in Figure 6.7 . In this particular reference frame, we have $P_{\pi^+\pi^-} = P_{t,\pi^+\pi^-}$. This frame is special because the longitudinal π^0 momentum *should not* depend on the actual value of $P_{t,\pi^+\pi^-}$, i.e. on the value of $P_{\pi^+\pi^-}$. In other words: if tracking was perfect, with infinite resolution, the quantity calculated in Equation 6.2 would be the same for all values of $P_{\pi^+\pi^-}$. The width of this distribution is due to resolution. A data and Monte Carlo overlay tests how well the tracking system, with its resolution effects, is simulated. Figure 6.8 shows such an overlay in various situations. The agreement between data and Monte Carlo is very good for our nominal analysis. Note also the improvement in resolution when using the mass-constrained vertex instead of the standard vertex.
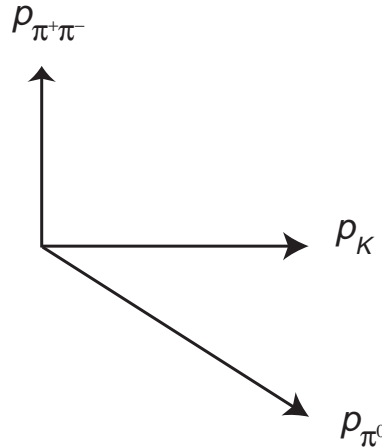
Figure 6.7: Diagram of momenta for "missing particle momentum" frame.
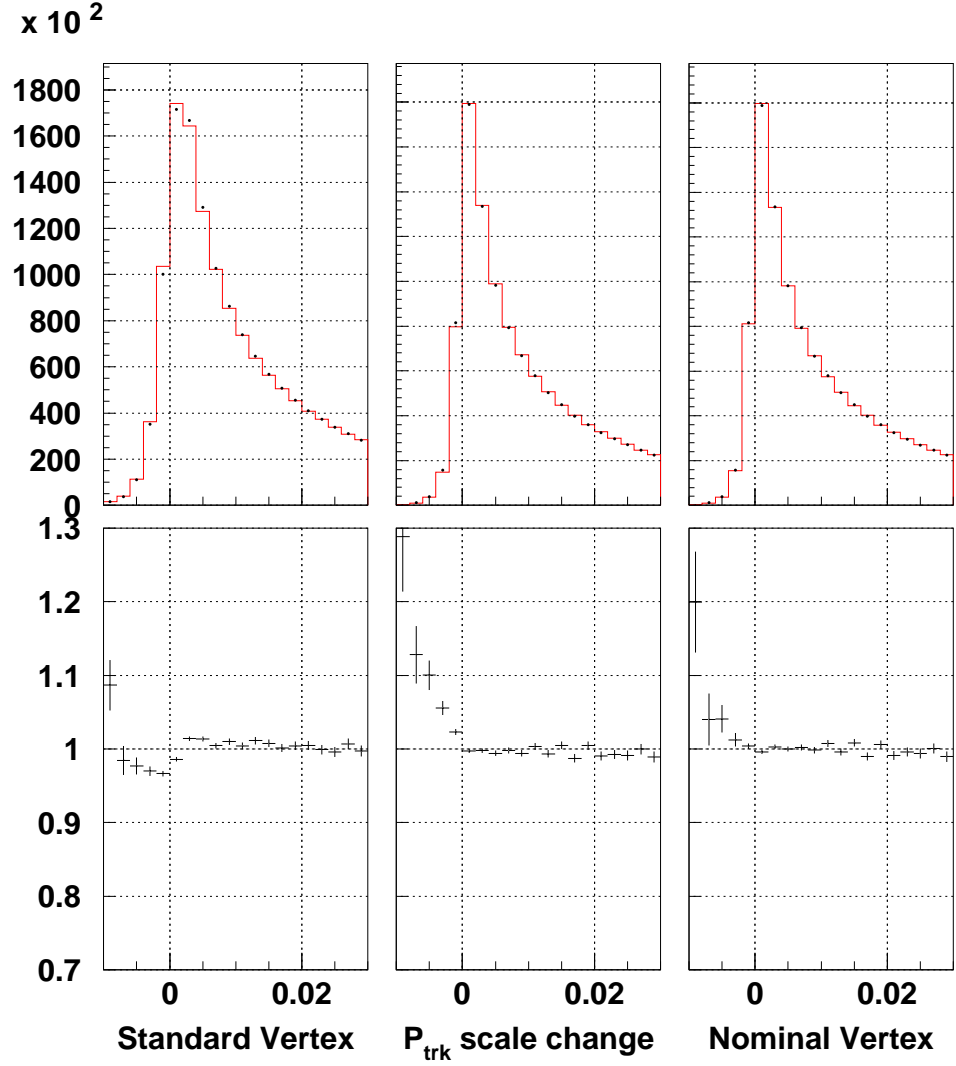
Figure 6.8: Tracking resolution in terms of "missing particle momentum". Data (dots) and Monte Carlo overlays of $p_{\pi^0\|}$, as defined by Equation 6.2. Left: using the standard vertex in the reconstruction. Middle: effect of changing the charged momentum scale (see Section 7). In this plot, the mass-constrained vertex has been used. Right: our nominal analysis result, using the mass-constrained vertex. Notice the width has been reduced considerably by the mass constraint, indicating better resolution. Also, the nominal data and Monte Carlo overlay is much better, indicating matching resolutions in data and Monte Carlo.

6.3 Measurement of the Radiative Cross-section

The KTeV calorimeter is a very good tool for reconstructing photons. The MIP sample we have used in the Dalitz analysis is also very suitable for measuring the radiative branching ratio

$$Br = \frac{\Gamma(K_L \rightarrow \pi^+\pi^-\pi^0\gamma\ )}{\Gamma(K_L \rightarrow \pi^+\pi^-\pi^0\ )}. \tag{6.3}$$

This branching ratio was predicted back in 1996, using Chiral Perturbation Theory[7]. It is in itself a very interesting measurement, especially because there is good acceptance cancellation between the two modes.

The cuts applied for this measurement are essentially the same as the nominal cuts applied in for the Dalitz parameter measurement except for requiring an extra cluster in the calorimeter, together with modified mass constraints (see Table 6.1).

The two mass constraints are designed to eliminate accidental photon events, which can be mistaken for radiative events. The "out of mass" window cut reduces the misidentification of radiative photons by identifying those $\pi^+\pi^-\pi^0$ events which make a "good" kaon mass. A more detailed discussion of this measurement can be found in Appendix D. The main issue here is that, by comparing the data and Monte Carlo energy distributions of radiative photons in the center of mass frame, we have been able to determine a correction to the PHOTOS contribution. This essentially amounts to increasing the amount of PHOTOS contribution by a factor of 2. Details of this correction and the systematic uncertainty introduced to our measurement will be discussed in Chapter 7.

6.4 Fitting the Dalitz Parameters

The Dalitz function 1.4 gives the probability distribution of $\pi^+\pi^-\pi^0$ events in the Dalitz phase space. Figures 4.7 and 4.8 show how the data populates the Dalitz plot (there is no acceptance correction applied here). One possible way to calculate the Dalitz parameters is to fit the Dalitz distribution to the acceptance corrected data. In the i-th bin, the decay probability $|\mathcal{M}_i|^2$ would be

$\pi^+\pi^-\pi^0\gamma$ invariant mass window	$0.49 - 0.502$ GeV
$\pi^+\pi^-\pi^0$ invariant mass *outside* of the range	$0.495 - 0.500$ GeV
Separation between radiative γ and tracks	> 0.1 m
Extra cluster energy, in the lab frame	> 0.5 GeV

Table 6.1: Extra/modified cuts applied in the radiative analysis.

$$|\mathcal{M}_i|^2 = \frac{N_i^{Rec.\ data}}{F_{data}} \times \frac{1}{Acc_i} \times BC_i, \tag{6.4}$$

where F_{data} is the kaon flux, Acc_i is the acceptance, given by

$$Acc_i = \frac{N_i^{Rec.\ MC}}{N_i^{Gen.\ MC}}, \tag{6.5}$$

and BC_i is the "bin-center" correction given by

$$BC_i = \frac{|\mathcal{M}^{MC}(Y_i, X_i)|^2}{\int_i |\mathcal{M}^{MC}|^2,}, \tag{6.6}$$

where $\mathcal{M}^{MC}$ is the Dalitz distribution function used in the Monte Carlo simulation, Y_i and X_i are the value of the Dalitz variables at the center of bin i, and the integral is taken across bin i. Combining formulae 6.4, 6.5, 6.6, and using that $N_i^{Gen.\ MC} = \int_i |\mathcal{M}^{MC}|^2 \times F_{MC}$, where F_{MC} is the kaon flux in the simulation, one obtains

$$|\mathcal{M}_i|^2 = \frac{N_i^{Rec.\ data}}{N_i^{Rec.\ MC}} \times \frac{F_{MC}}{F_{data}} \times |\mathcal{M}_i^{MC}|^2. \tag{6.7}$$

so that

$$\frac{|\mathcal{M}_i|^2}{|\mathcal{M}_i^{MC}|^2} = \frac{N_i^{Rec.\ data}}{N_i^{Rec.\ MC}} \times \frac{F_{MC}}{F_{data}}. \tag{6.8}$$

The l.h.s. of Equation 6.8 is

$$\frac{|\mathcal{M}_i^{data}|^2}{|\mathcal{M}_i^{MC}|^2} = \frac{1 + gY_i + hY_i^2 + jX_i + kX_i^2 + fX_iY_i}{1 + g_{MC}Y_i + h_{MC}Y_i^2 + j_{MC}X_i + k_{MC}X_i^2 + f_{MC}X_iY_i}. \tag{6.9}$$

To fit the Dalitz parameters we have to fit the function $\mathcal{F}(Y_i, X_i; g, h, j, k)$, defined by

$$\mathcal{F}(Y_i, X_i; g, h, j, k) = \frac{1 + gY_i + hY_i^2 + jX_i + kX_i^2 + fX_iY_i}{1 + g_{MC}Y_i + h_{MC}Y_i^2 + j_{MC}X_i + k_{MC}X_i^2 + f_{MC}X_iY_i}, \tag{6.10}$$

to the ratio of reconstructed data and reconstructed Monte Carlo histograms. This is done by minimizing

$$\mathcal{L}(g, h, k, \epsilon) = \sum_i \frac{1}{\sigma_i^2} \left(\frac{N_i^{Rec\ data}}{N_i^{Rec\ MC(g,h,k)}} - \epsilon \mathcal{F}(Y, X; g, h, j, k, f) \right)^2 \to \min. \tag{6.11}$$

where σ_i is the statistical error in bin i.

Using this strategy, we first fit allowing all Dalitz parameters to float. Table 6.2 shows the values obtained in this case. The CP-violating parameters j and f are

consistent with zero, so they will be fixed to zero for our nominal fit. Table 6.3 shows the nominal fit values.

g	0.7065 ± 0.0023
h	0.0963 ± 0.0034
j	-0.00036 ± 0.0011
k	0.0216 ± 0.0011
f	0.0018 ± 0.0023
χ^2	199.1 for 178 d.f.

Table 6.2: Dalitz parameter fit, allowing all parameters to float. Only statistical errors are quoted here. The CP violating parameters j and f are consistent with zero.

	KTeV 1997
g	0.7065 ± 0.0023
h	0.0962 ± 0.0034
k	0.0216 ± 0.0011
χ^2	199.8 for 180 d.f.

Table 6.3: Nominal Dalitz parameter fit. The CP violating parameters j and f have been fixed to zero. Only statistical errors are quoted here.

CHAPTER 7
SYSTEMATIC STUDIES

The Dalitz parameter measurement depends to first order on an accurate detector simulation. Figure 5.2 shows that the acceptance varies roughly by about a factor of two across the Dalitz plane, and its biggest variation is in the Y direction, which affects the linear slope parameter g directly.

7.1   Kinematic Limits for the Dalitz Variables

7.1.1   Charged Invariant Mass Resolution

The most important aspect for this analysis are systematic errors associated with momentum measurement of the charged pions. For the $\pi^+\pi^-\pi^0$ decay, the invariant mass of the two charged pions, $m_{\pi^+\pi^-}$, has a maximum value which depends on their transverse momentum squared, $p_{t,ch}^2$, and is given by

$$m_{\pi^+\pi^-}^2 \leq \left(M_K - \sqrt{m_{\pi^0}^2 + P_{t,\pi^+\pi^-}^2}\right)^2 - P_{t,\pi^+\pi^-}^2. \tag{7.1}$$

Since

$$Y = \frac{S_3 - S_0}{m_{\pi^+}^2} = \frac{m_{\pi^+\pi^-}^2 - S_0}{m_{\pi^+}^2}, \tag{7.2}$$

this is also a kinematic limit for the Y Dalitz variable. Figure 7.1, top, shows the distribution of Y for data as a function of $P_{t,\pi^+\pi^-}^2$. The solid line indicates the kinematic limit. Events accumulate at the boundary because the boundary is a symmetric configuration in the $\pi^+\pi^-$ momenta. Some events go past the boundary, as can be more clearly seen in the lower plots. This is due to finite detector resolution. Note also that, as we go higher in P_t^2, the limit for Y, Y_{max}, goes down. If it were the case that only the absolute maximum value of Y was affected by resolution, this would not really be an important issue, as we cut the kinematic boundaries away for our measurement anyway. However, since Y_{max} spans all possible Y values, a mismatch in the data and Monte Carlo reconstruction would produce a difference in event migration all across the Dalitz plane, which could bias our measurement. In Section 6.2.2 we analyzed how well the data and Monte Carlo resolutions match. The same arguments apply here.
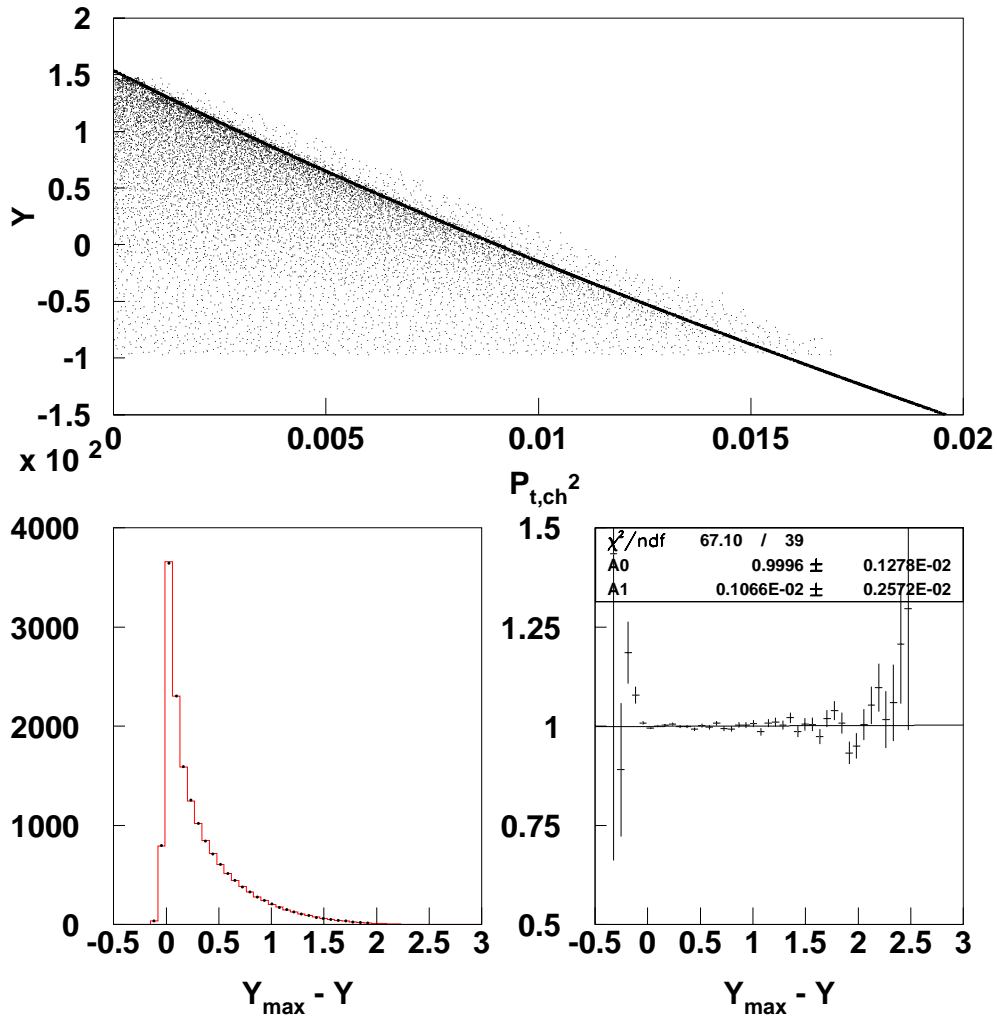
Figure 7.1: Distribution of reconstructed values for the Y Dalitz variable. Top: Distribution of the reconstructed values of the Y Dalitz variable as a function of $p_{t,ch}^2$ for data. The solid line indicates the kinematic limit given in Equation (7.2). Bottom: the same distribution projected along the kinematic limit. Dots and open histogram represent data and Monte Carlo simulation, respectively. On the right the data/MC distribution is shown.

7.1.2   Kinematic Limits in the Dalitz Plane: The Mask

Finite detector resolution leads to the event migration beyond the kinematic limit in the X, Y Dalitz plane as well. To avoid events at the kinematic boundary, we apply a mask to our Dalitz plot. This mask is determined by the requirement that it eliminates those points around the kinematic boundary that either have much fewer counts than its neighbors, or are very close to the kinematic boundary. Figure 4.7 shows the data, where the grid represents the selection mask. From this plot we estimate that we cut away roughly 1-2 bins away from the kinematic boundary. Each bin is roughly 0.2 units wide in the Dalitz variables X and Y, which are adimensional. Since the Dalitz variables are in units of $m_{\pi^+}^2$, this means we are cutting events that are roughly closer than $\sqrt{\Delta s} \sim 0.06$ GeV to the boundary. In terms of the Dalitz variable resolution, which we estimated to be on the order of 0.01-0.02 (Figure 6.6), this boundary cut is safe. The effect of the mask is considered in the systematic uncertainty, as shown in Figure 7.8. We evaluated the effect of removing the mask altogether and also "tightening" the mask, by increasing the distance we cut from the boundary to about 5 bins. Since the effect is small, within statistics, we did not include it in the evaluation of the systematics.

7.2   MIP Efficiency Systematic

The MIP probability, as determined from data, was incorporated in the Monte Carlo. It could be argued that, although a sample with a MIP energy cut is used to avoid biases due to pions showers in the calorimeter, estimating the MIP efficiency using non-MIP data (i.e. data with no MIP energy cut), effectively reintroduces whatever bias we were trying to avoid. One way in which the non-MIP sample could be biased is if the shower subproducts affect the photon clusters from the π^0. This would be important during full reconstruction, as the energies associated with the π^0 would be biased. However, in the efficiency determination we only evaluate the probability of single tracks to be MIP, disregarding whatever happens to the π^0. To verify that there is indeed no bias, we calculated the data MIP efficiency with these modifications:

- Eliminated the m_{π^0} and m_K window cuts. In this case we obtain a P_{trk} efficiency slope of $(-3.27 \pm 0.47) \times 10^{-4}$ c/GeV (to be compared with the nominal $(-3.05 \pm 0.47) \times 10^{-4}$ c/GeV value);

- Relaxing the track-photon separation cut to 25 cm (from the nominal 35 cm used in the efficiency study). This results is a P_{trk} slope of $(-2.60 \pm 0.29) \times 10^{-4}$ c/GeV.

Additionally, we studied the measured MIP efficiency as a function of the separation between the charged tracks. This is important because a track's probability to pass the MIP energy cut might depend on whether the other charged track showers or

not, especially when the two tracks are close together. To study this, we plotted the MIP probability of one track when the other track does *not* MIP. We did not find any dependance of the MIP probability as a function of track separation at the calorimeter.

The systematic uncertainty associated with the MIP efficiency correction in the Monte Carlo is evaluated by simply eliminating the efficiency correction rather than considering the possible uncertainties in its determination. Its effect is smaller than other systematics.

7.2.1   Selection cut systematics

The measurement of the Dalitz parameters can be biased if some of the selection cuts reject $\pi^+\pi^-\pi^0$ events differently in data and Monte Carlo. To analyze the systematic effect of the analysis cuts, we considered the variation of the fitted Dalitz parameters when we add all events eliminated by each cut. The basic assumptions in such procedure are that

- There is no bias at the preselection level, i.e. the preselection cuts are not too tight.

- The sample with one cut added is sufficiently free of background.

- Different cuts are not correlated.

The preselection cuts are indeed looser than the selection cuts, as we have verified. Figure 7.8, left, shows the variation of the Dalitz parameters when we add all events that did not pass the corresponding cut. We only show those cases in which the effect is noticeable and/or the study would produce a direct effect on the Dalitz parameters. One can see that most of the variations in the fitted parameters are consistent with statistical fluctuations.

The quantity that stands out is the analysis with no MIP cut. This systematic is evaluated by doing the analysis without a MIP cut (both in data and Monte Carlo). We chose this procedure instead of one in which we would increase the MIP energy selection cut because the shower distribution is spread over a broad spectrum of energies. Increasing the track cluster energy cut from 1 GeV to, say, 2 GeV does not add many events to our sample, and we fail to really probe the effect of big showers in the analysis. It is also important to mention that the sample with no MIP cut does have an E/p cut at 0.85. We used B01RAN $\pi^+\pi^-\pi^0$ events to determine if a bias is caused by this cut, and we did not see any effect, within statistics.

Other cut systematics are within the statistical uncertainty of our measurement.

7.3 Discrepancies Between Data and Monte Carlo

7.3.1 Scales and Resolutions

We studied the systematics associated with photon reconstruction energy scales, track momentum scales, and momentum resolution by reweighting the Monte Carlo analysis. In the case of the track momentum scale, a shift of -0.09% was used, chosen to make the data and Monte Carlo $M(\pi^+\pi^-\pi^0)$ overlays match. Additionally, a smearing of 0.3% of the value of the momentum was chosen to make the widths match, Figure 7.2, left. For the photon scale, we modified the scale by 0.1%, based on the possible discrepancy in the $M(\gamma\gamma)$ invariant mass plot, Figure 7.2, right.

7.3.2 Drift Chamber Illumination

Figure 7.3 shows the data and Monte Carlo overlays for drift chamber illuminations. We see a feature in the Y illumination, corresponding to an excessive loss of data events close to the center of the chambers. Many possible causes have been studied:

- Fringe magnetic fields around the drift chambers;

- Magnetic field non-uniformities at the kick plane;

- Event loss as a function of track separation at the calorimeter (due to the MIP energy cut);

- Drift Chamber alignment;

- Effect of Event Loss due to Cracks in the hodoscope bank and/or the calorimeter;

None of the above studies have proven to correct the illumination discrepancy. So far, the only modification that has fixed the illumination problem is to assume that the vertical dimension of one of the drift chambers is different from the nominal value by about 100 μm/m.

To estimate the systematic error introduced, we reweighted the Monte Carlo distribution such that the illumination by tracks at drift chamber 1 is flat. This is the leading negative systematic for the slope parameter g ("negative" because it pulls the value of g down), and is one of the most important issues to solve in the future.

7.3.3 Energy and Track Momentum Slopes

The energy spectrum for kaon has been tuned using $\pi^+\pi^-$ events. This tuning was done some time ago. At the time of this writing, the $\pi^+\pi^-$ kaon energy slope in the data and Monte Carlo overlay is about $(-3.5 \times 10^{-4}$ 1/GeV. In our analysis, we find
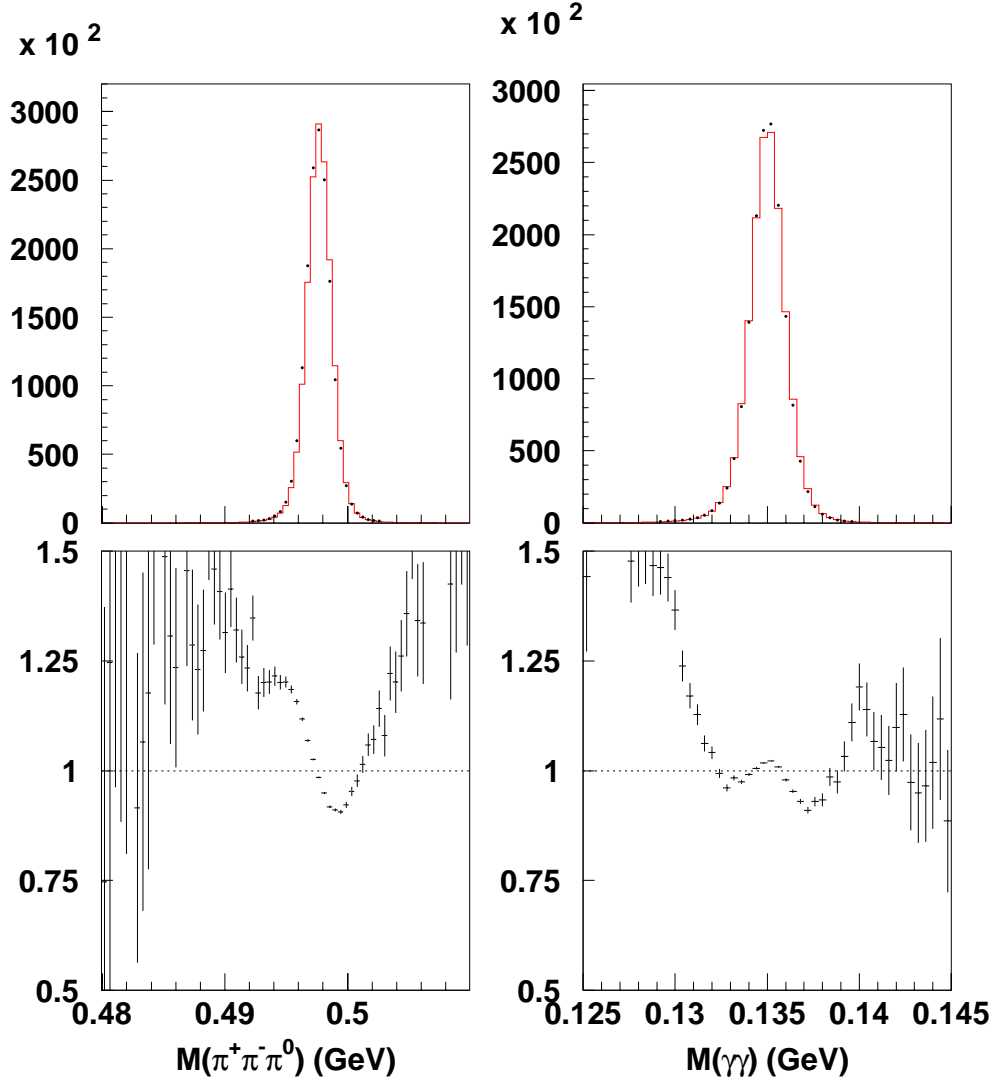
Figure 7.2: Kaon and neutral pion reconstructed invariant masses. Left: $M(\pi^+\pi^-\pi^0)$ invariant mass. Note the small data/Monte Carlo discrepancy and the difference in resolution. Both these effects have been taken into account in the systematic uncertainty. Right: $M(\gamma\gamma)$ invariant mass. The size of the wiggle has been taken as a measure of the E_γ scale uncertainty for the systematics.
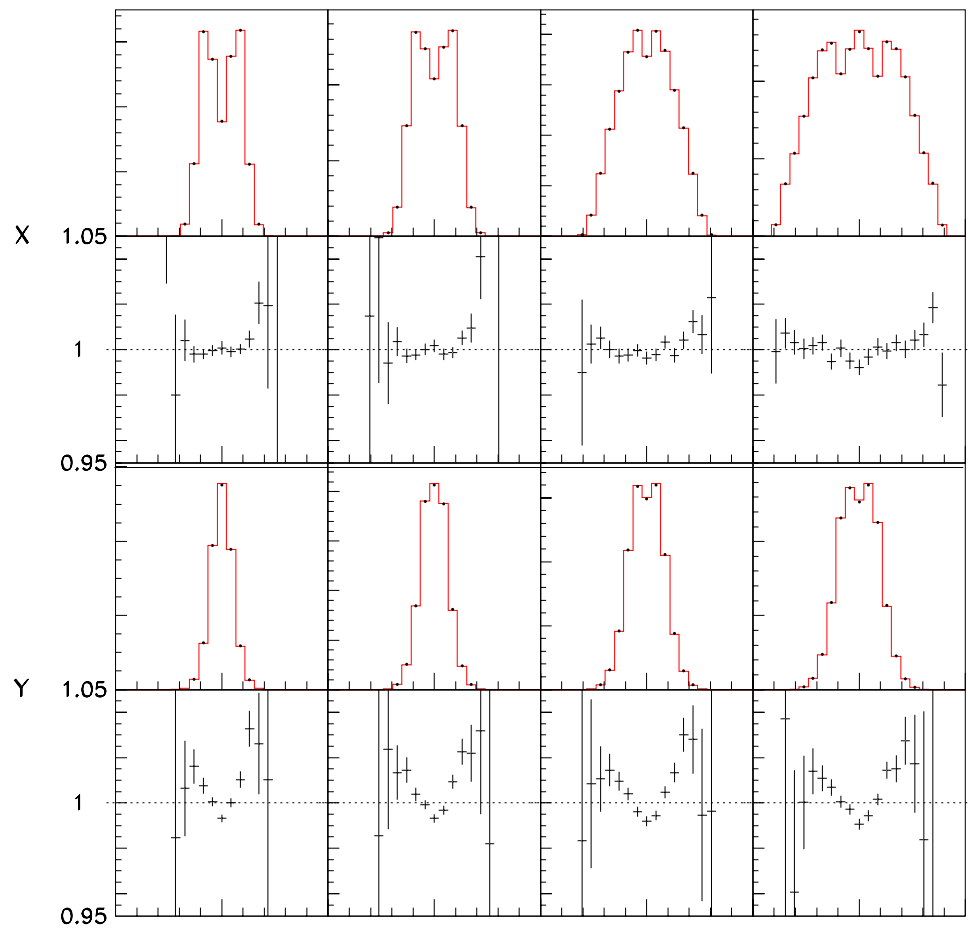
Figure 7.3: Drift chamber illumination by charged tracks, for the X view (top row) and the Y view (bottom row). Notice the shape seen in DC1-Y, which has been taken into account in the systematics.
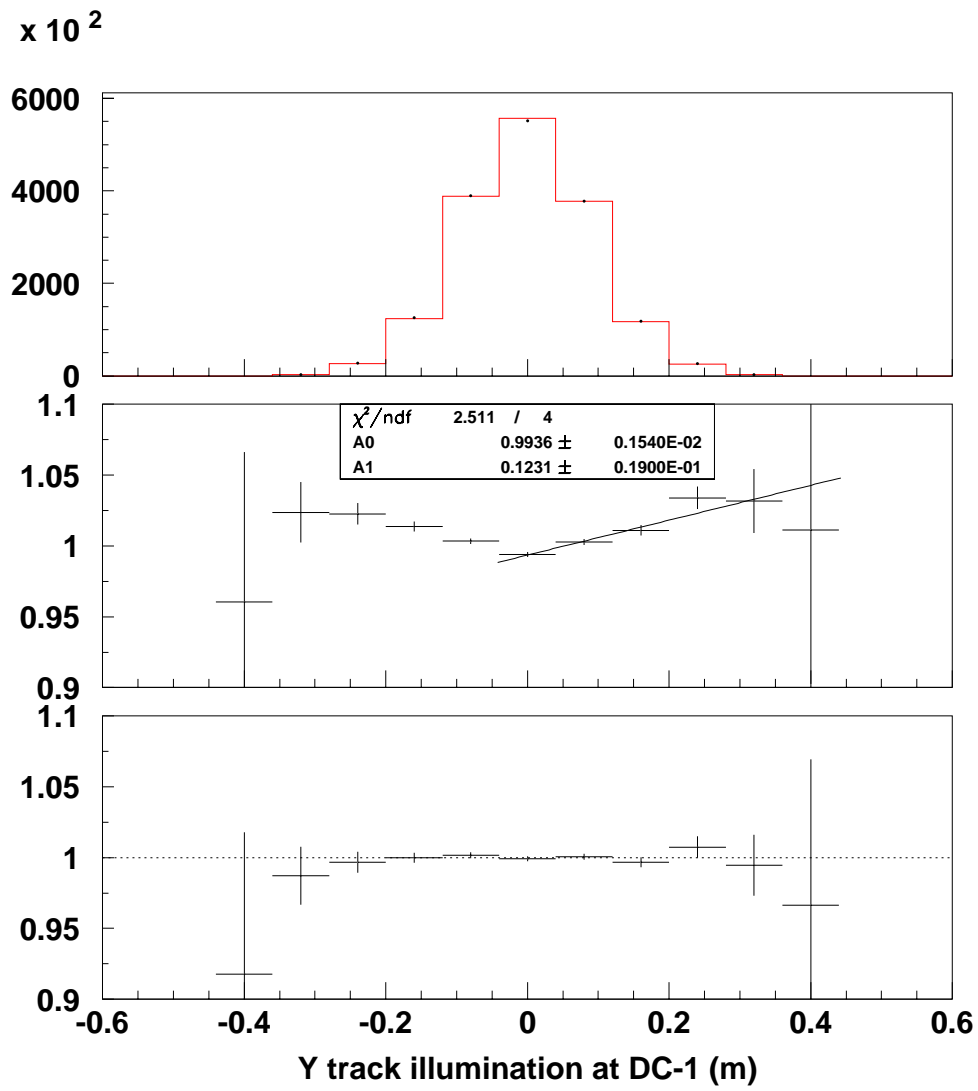
Figure 7.4: Drift chamber 1 illumination in the Y direction, data and Monte Carlo overlay. The center plot corresponds to the ratio and the bottom plot shows the effect of reweighting the Monte Carlo.

the energy slope for the nominal sample to be $(-9.02 \pm 0.57) \times 10^{-4}$ 1/GeV. If we do not apply a MIP energy cut, the energy slope is $(-8.45 \pm 0.65 \times 10^{-4}$ 1/GeV, which is consistent with the MIP cut value. Moreover, if we increase the track-photon separation cut to 35 cm (from the nominal 25 cm), we find that the energy slopes for MIP and non-MIP cases are $(-7.7 \pm 2.1) \times 10^{-4}$ 1/GeV and $(-5.6 \pm 2.7) \times 10^{-4}$ 1/GeV, which are consistent with each other and not far from the slope in $\pi^+ \pi^-$ events. This shows that there is no substantial energy slope problem in our measurement. Figure 7.5 shows the data and Monte Carlo overlay for energy. The systematics due to this energy slope is estimated by reweighting the Monte Carlo.

As we already discussed, there is a track momentum dependance of the MIP efficiency, which we have incorporated in the Monte Carlo. In spite of this, the data and Monte Carlo overlay shows a track momentum slope. This might be a bi-product of having a mismatch in the kaon energy spectrum. Indeed, if we reweight the Monte Carlo analysis by the energy slope, there is a considerable change in the momentum slope. A similar thing happens if we reweight the Monte Carlo by the track momentum slope[1]. Figures 7.6 and 7.7 show the effect of reweighting by kaon energy and track momentum, respectively.

The systematic associated with these slopes is shown in Figure 7.8. It is obtained by reweighting the Monte Carlo such that we eliminate the energy and track momentum slopes (separately). It is remarkable that the effect of reweighting the energy in the slope parameter g is in the *opposite* direction compared to the effect of reweighting by track momentum. This is, however, not completely unexpected, as the change in phase space produced by reweighting by each track momentum versus the change produced by applying a weight based on the total reconstructed energy of the event is quite different.

7.4   "Half" Tests

To check the stability of the resulting Dalitz parameters the input data was divided into statistically equivalent "halves" in various variables. The results of these tests and the systematics are shown in Figure 7.9. The meaning of the half-sample labels is as follows

- $\mathbf{E_K}\pm$ — $E_K > < 62.4$ GeV,

- $\mathbf{P_{trk,min}}\pm$ — $\min |P_{trk}| > < 16.0$ GeV,

---

[1]Since there are two tracks in each event, it is not obvious how to reweighting the Monte Carlo. We did so by reweighting by the product of the two slopes, considered independently. We checked this by reweighting via a two-entry reweight function, with an equivalent result.
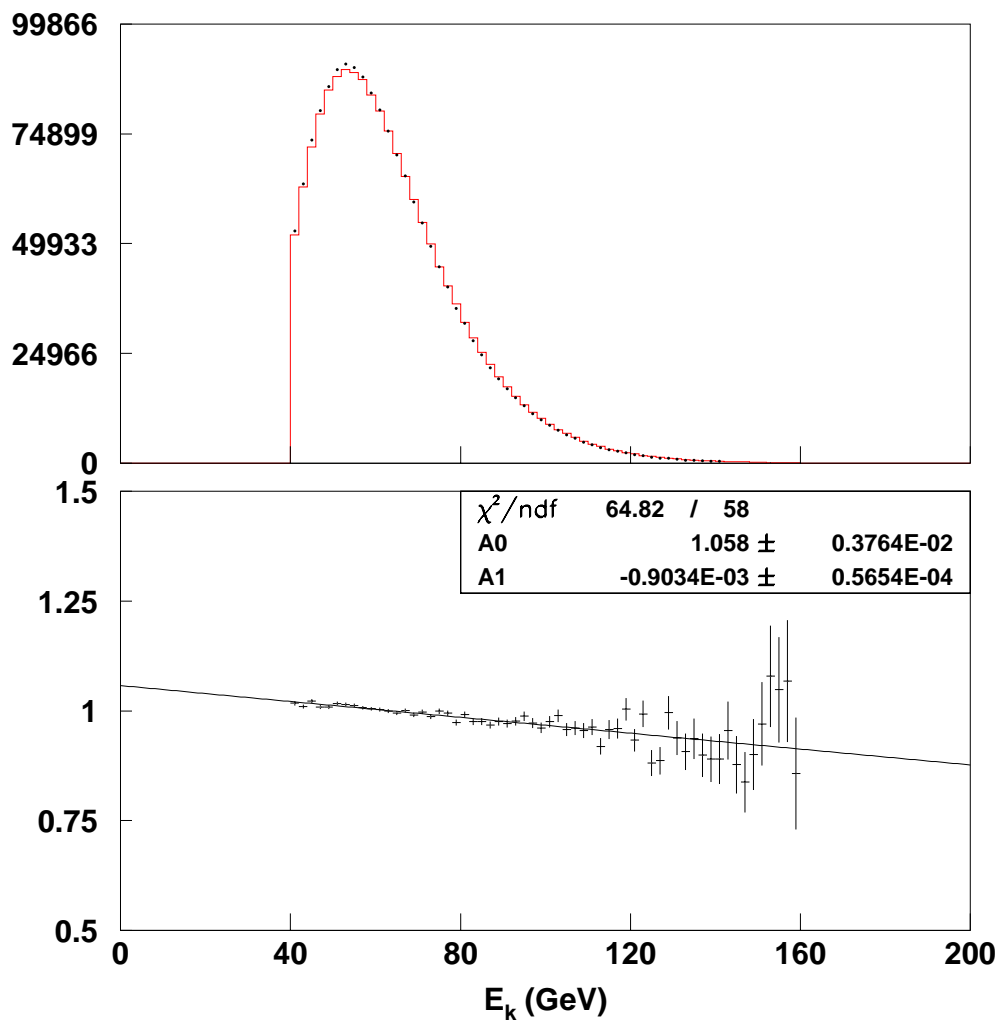
Figure 7.5: Kaon energy slope in $\pi^+\pi^-\pi^0$ MIP events. Data and Monte Carlo overlay.
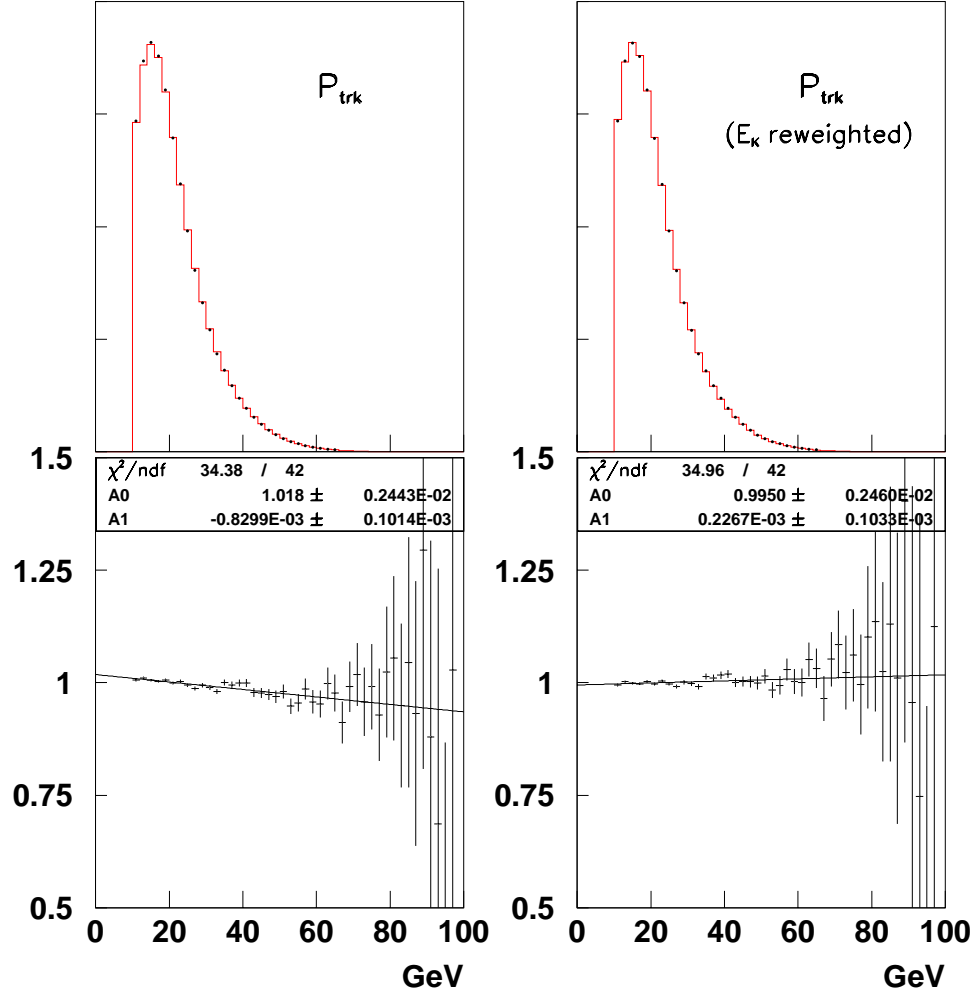
Figure 7.6: Track momentum distribution, reweighted by the Kaon energy slope.

- $\mathbf{P_{trk,max}}\pm$ — $\max |P_{trk}| > < 26.0$ GeV,

- $\mathbf{E_{\gamma}}\pm$ — $\min E\gamma > < 7.0$ GeV,

- $\mathbf{In-bends/Outbends}$ — Events with in-bend or out-bend tracks,
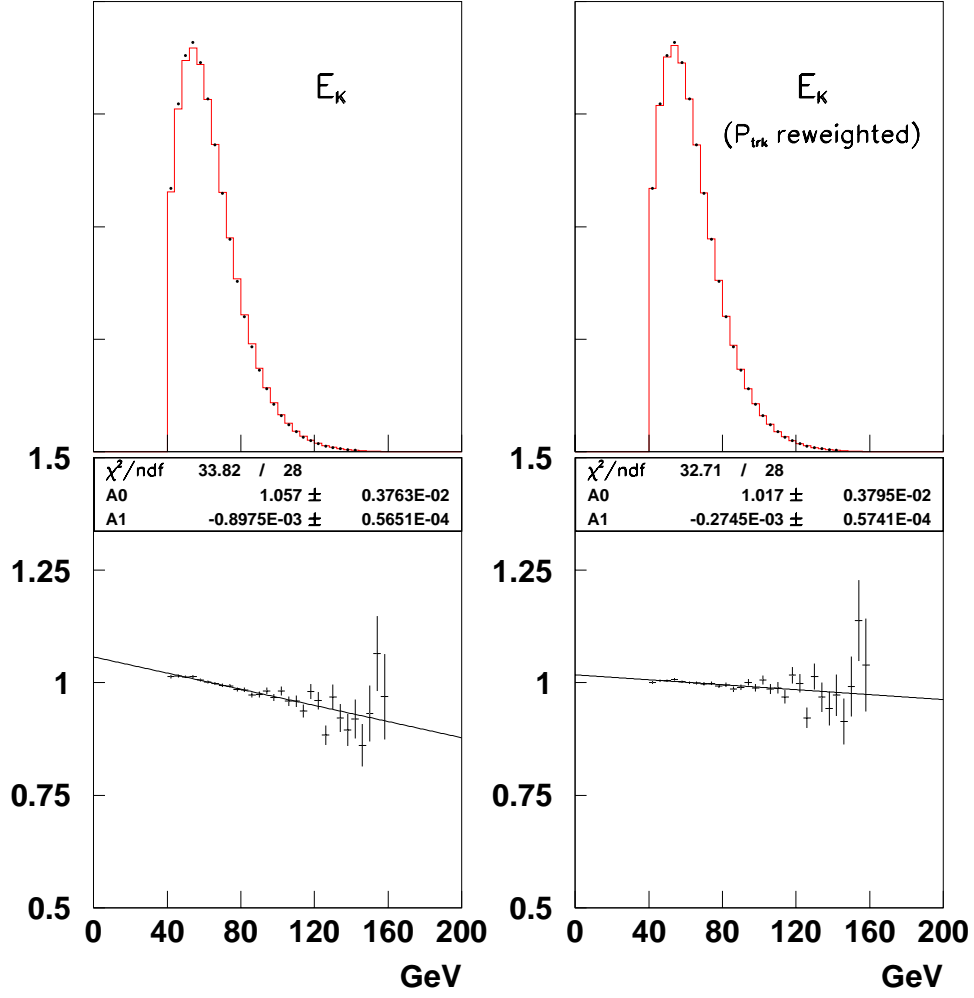
Figure 7.7: Kaon energy distribution, reweighted by the track momentum slope.

- $\mathbf{Z_{vtx}}\pm$ — $Z_{vtx} >< 133$ cm,

- $\mathbf{X_{vtx}}\pm$ — $X_{vtx} >< 0$,

- $\mathbf{Y_{vtx}}\pm$ — $Y_{vtx} >< 0$,
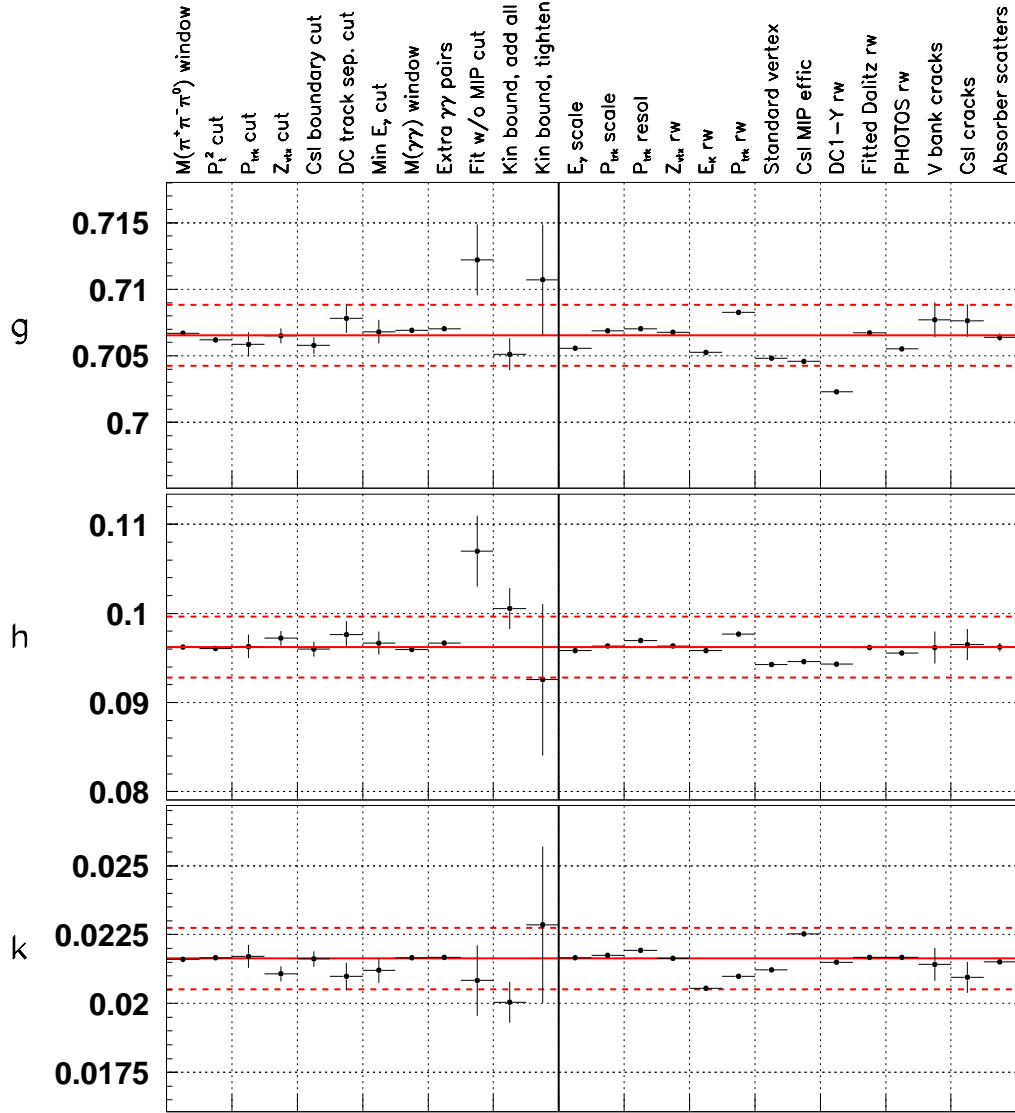
Figure 7.8: Systematic tests. Left: Cut systematics, which correspond to adding the events that failed the cut and refitting the Dalitz parameters to this new sample. Right: Other systematic effects, including reweighting various physics distributions to make data and Monte Carlo match, using the standard vertex in reconstruction, refitting after reweighting the Monte Carlo by the fitted Dalitz parameters (effectively the same as regenerating Monte Carlo with the new parameters). Lastly, we show the variations when we mask V bank and calorimeter cracks, and the effect of eliminating absorber scatters from the Monte Carlo simulation.

We also studied the variation of the fit parameters with the run periods. Note the variation in 97A, which is most likely correlated with the Y drift chamber illumination discrepancy we already mentioned.
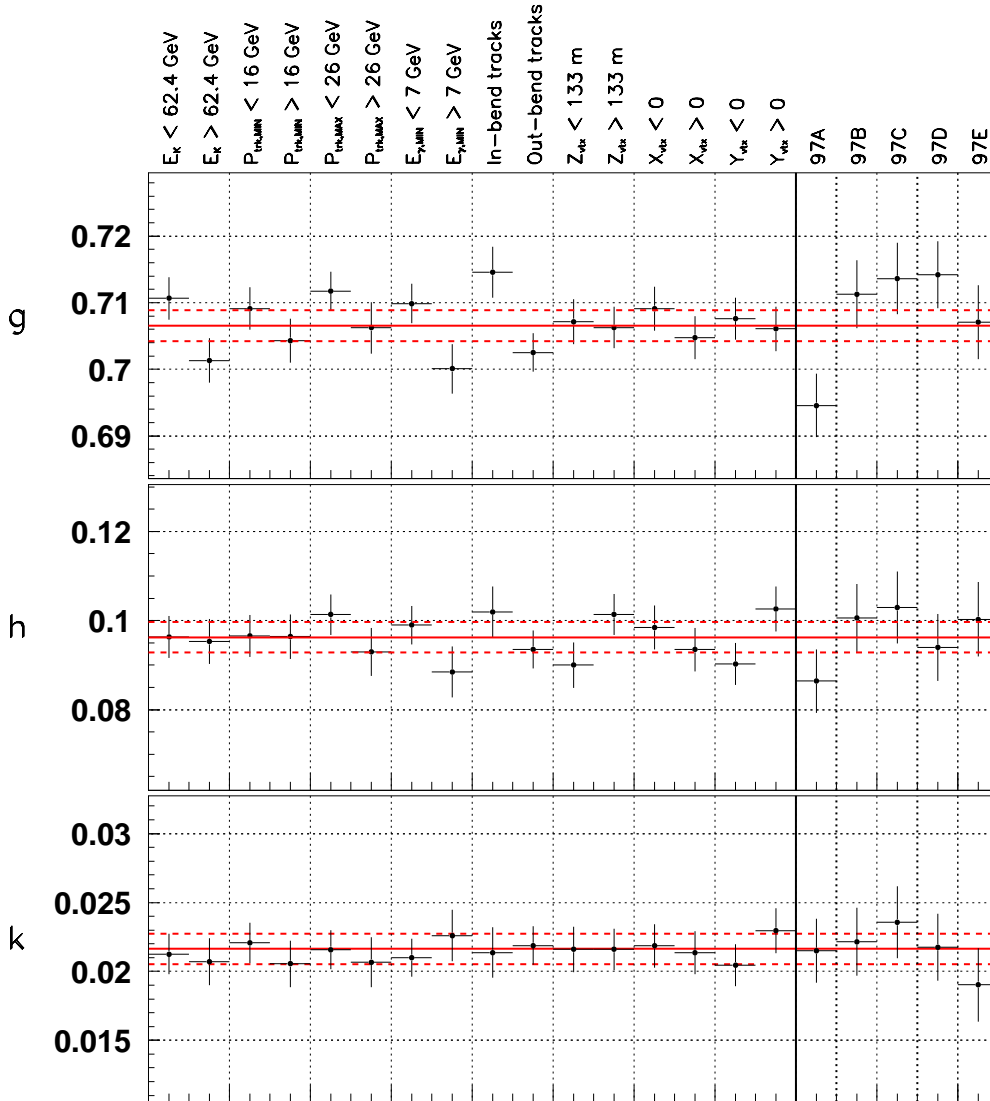
Figure 7.9: Half-sample and run periods studies. Left: Effect of dividing the data and Monte Carlo samples in half, for various physics distributions. Right: Fit for different run periods (97A is the official split, all others are such that the sample sizes are roughly the same.

7.5   Radiative Corrections

The QED radiative corrections to the $K_L \rightarrow \pi^+\pi^-\pi^0$ decay are small, as we have determined in a previous study. However, they have a direct effect on the charged invariant mass distribution, as the radiative photon takes some of the energy available to the final state pions. They also produce a (small) change in acceptance as the radiative photon could hit a veto detector or produce a bias in the reconstruction.

The influence of the radiative corrections was studied with an implementation of the PHOTOS [19] package into the Monte Carlo. PHOTOS is a calculation in a leading log approximation of a single (or double) bremsstrahlung process taking place in a decay chain. The virtual corrections to the Born level process are calculated numerically requiring cancellation of the infrared divergence for the total cross section. The infrared cut off parameter was set to 1 MeV. The program was used in single photon mode. The variable PARVAL of the radiative photon was set to 0 allowing the particle to be lost during the tracing through the detector.

To determine how well PHOTOS describes the radiative photon, we studied the energy of the radiative photon in the Kaon center of mass frame. Figure 7.12, top, shows the background subtracted data and generated PHOTOS distributions. Signal Mote Carlo is normalized to the $M(\pi^+\pi^-\pi^0$) mass peak. To determine the background we generated non-radiative Monte Carlo, and required an extra photon to be reconstructed. We then normalized it to the upper mass tail of the $M(\pi^+\pi^-\pi^0\gamma$) distribution, as shown in Figure 7.11. The portion of the background which gets into the signal region corresponds (mostly) to photons with $E_\gamma^{CM} <$ 0.01 GeV, as can be seen in Figure 7.12, where the shaded region represents the background. It is critical then that we get this position of the background right, as it affects the linear slope parameter g directly. Figure 7.12, bottom, shows the effect of normalizing the background with photons with $E_\gamma^{CM} <$ 0.005 GeV (left) and $E_\gamma^{CM} >$ 0.005 GeV (right). The normalization factors are 3.3 and 1.7, respectively. We will take the first case as nominal, as it is the one that most influences our signal region (because we apply a mass cut to reconstructed $\pi^+\pi^-\pi^0$ events), and the second case will be taken as a measure of the systematic uncertainty.

Figure 7.10 shows the invariant mass distribution for reconstructed $\pi^+\pi^-\pi^0$ events. Notice how the non-radiative Monte Carlo, the standard PHOTOS contribution, and our reweighted distribution compare. Note also that the reweighting has been done by studying the center of mass energy distribution of the radiative photon and not by just matching the lower mass tail distribution shown here.

There is an additional effect we need to study. Since the cross-section is not constant across the Dalitz plane, the level of radiation is different as well. PHOTOS assumes a constant matrix element across the entire $\pi^+\pi^-\pi^0$ phase space. This means that the migration in the Dalitz plane due to radiative effects is different in data and Monte Carlo, and could conceivably affect the Dalitz parameters. The most important variation in the cross-section across the Dalitz plane is due to the

slope parameter g. Since this parameter is associated with the Dalitz variable Y, it is possible to estimate the effect of the migration produced by radiative photons on the reconstructed Dalitz variables. The Dalitz variable Y is given by:

$$Y = \frac{S_3 - S_0}{m_{\pi^+}^2} = \frac{(P_K - P_{\pi^0})^2 - S_0}{m_{\pi^+}^2}, \tag{7.3}$$

and, if the event is non-radiative, it reduces to:

$$Y^{NR} = \frac{m_{\pi^+\pi^-}^2 - S_0}{m_{\pi^+}^2}. \tag{7.4}$$

To first order, we can calculate the effect of migration by reweighting the Monte Carlo events by

$$Weight = \frac{1 + g_{MC}Y}{1 + g_{MC}Y^{NR}}, \tag{7.5}$$

where g_{MC} is the Dalitz slope parameter used in the Monte Carlo generation and Y^{NR} is calculated as per Equation 7.4. The effect of such reweighting is very small, as shown in Figure 7.8.

7.6 Backgrounds

No background subtraction is done in this analysis. Since vacuum beam events are selected, the only possible backgrounds present would come from absorber scatters and collimator scatters. These two are simulated in the Monte Carlo, and the simulation is known to be good within 10%. Figure 7.13 shows the P_t^2 distribution, showing that data and Monte Carlo agree quite well. To evaluate the magnitude of the systematic introduced by the absorber collimator scattering backgrounds, we eliminated them from the Monte Carlo simulation and refitted the Dalitz parameters. The shift produced by the collimator scattering background is negligible. The shift in fitted parameters corresponding to absorber scatters was divided by 10, following the fact that we simulate them with a 10% accuracy. The effect is shown in Figure 7.8.

7.7 Additional Sources of Systematic Biases

The Dalitz measurement depends to first order on the precise modelling of our detector. Any discrepancies between data and the simulation will affect the measurement directly. It is then important to study all systematics due to scales and detector sizes and positions.
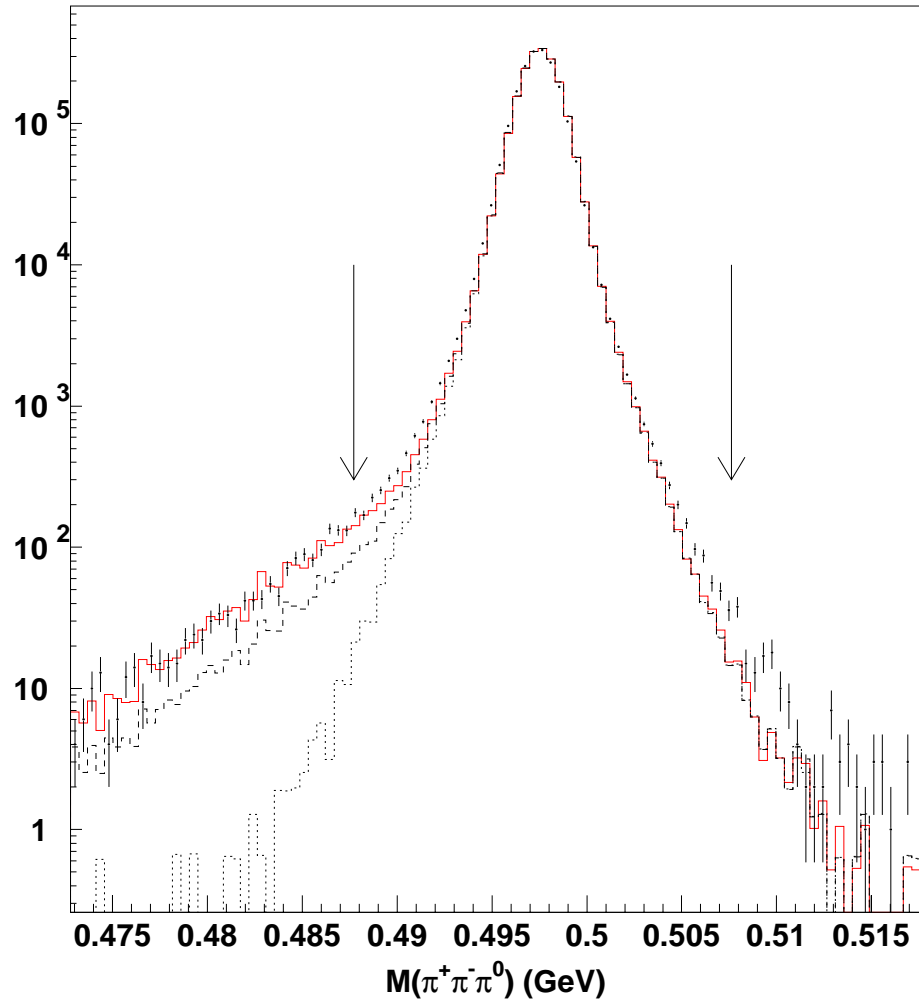
Figure 7.10: Low-mass radiative tail in data and Monte Carlo. This tail has contributions from radiative events in which the radiative photon was not reconstructed. Dots represent data. The dotted histogram is Monte Carlo with no radiative corrections, the dashed histogram corresponds to the standard amount of PHOTOS contribution, whereas the solid histogram corresponds to the reweighted PHOTOS contribution, as explained in the text.
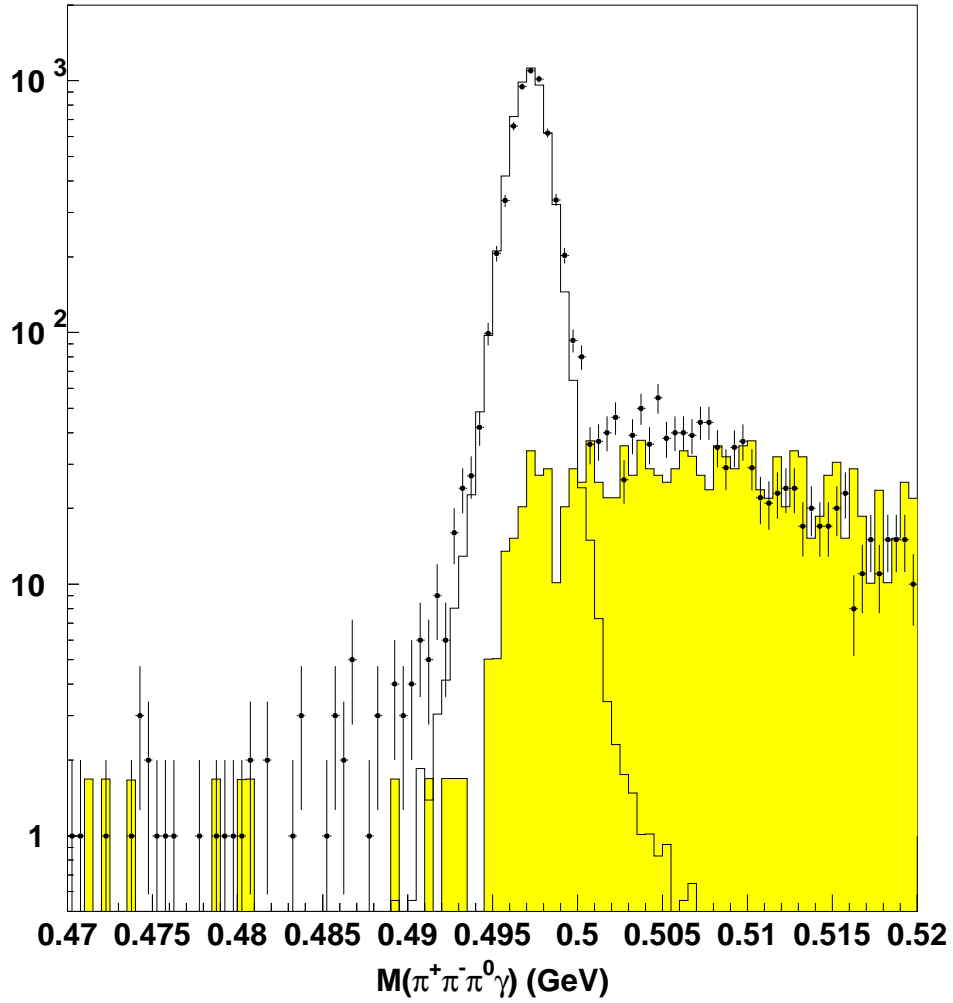
Figure 7.11: Invariant mass distribution for reconstructed $\pi^+\pi^-\pi^0\gamma$ events. The dots correspond to data and the full histogram to reconstructed $\pi^+\pi^-\pi^0\gamma$ Monte Carlo. The shaded region corresponds to background Monte Carlo, which is non-radiative Monte Carlo with a reconstructed accidental photon, and normalized to the upper mass tail. Note the background that creeps into the signal region: it corresponds to those photons with low center-of-mass energy (see Figure 7.12).
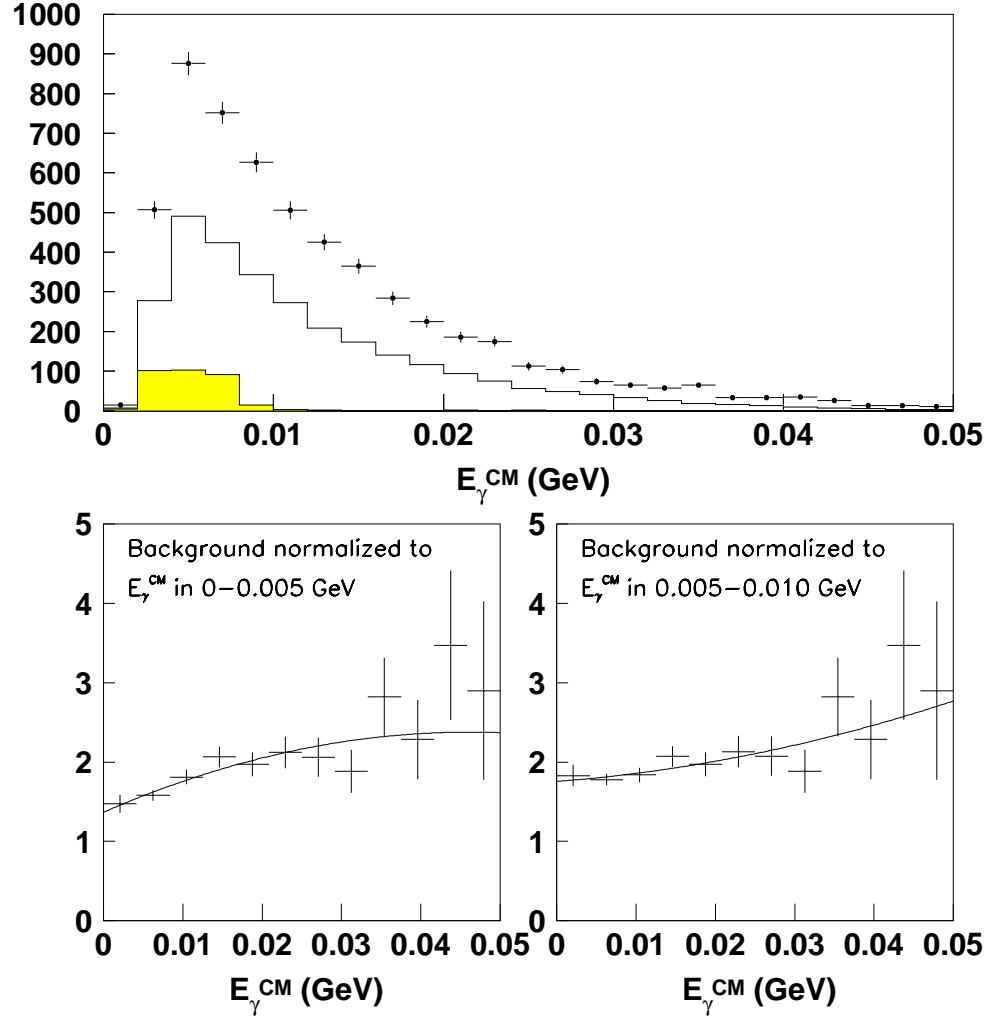
Figure 7.12: Data and PHOTOS contributions in the center of mass frame. Top: Radiative photon energy in the kaon center of mass frame. The dots are background subtracted data, the solid line is the standard PHOTOS radiative contribution, normalized to the $\pi^+\pi^-\pi^0$ signal region. The shaded region is the background contribution, normalized to the upper mass tail, as shown in Figure 7.11. Bottom: Ratio of data/PHOTOS, with background normalized with reconstructed photons with $E_\gamma^{CM} < 0.005$ GeV (left) and $E_\gamma^{CM} > 0.005$ GeV (right). The $E_\gamma^{CM} < 0.005$ GeV reweighting function will be taken as nominal, and the $E_\gamma^{CM} > 0.005$ GeV one will be used for systematics (see text for details).
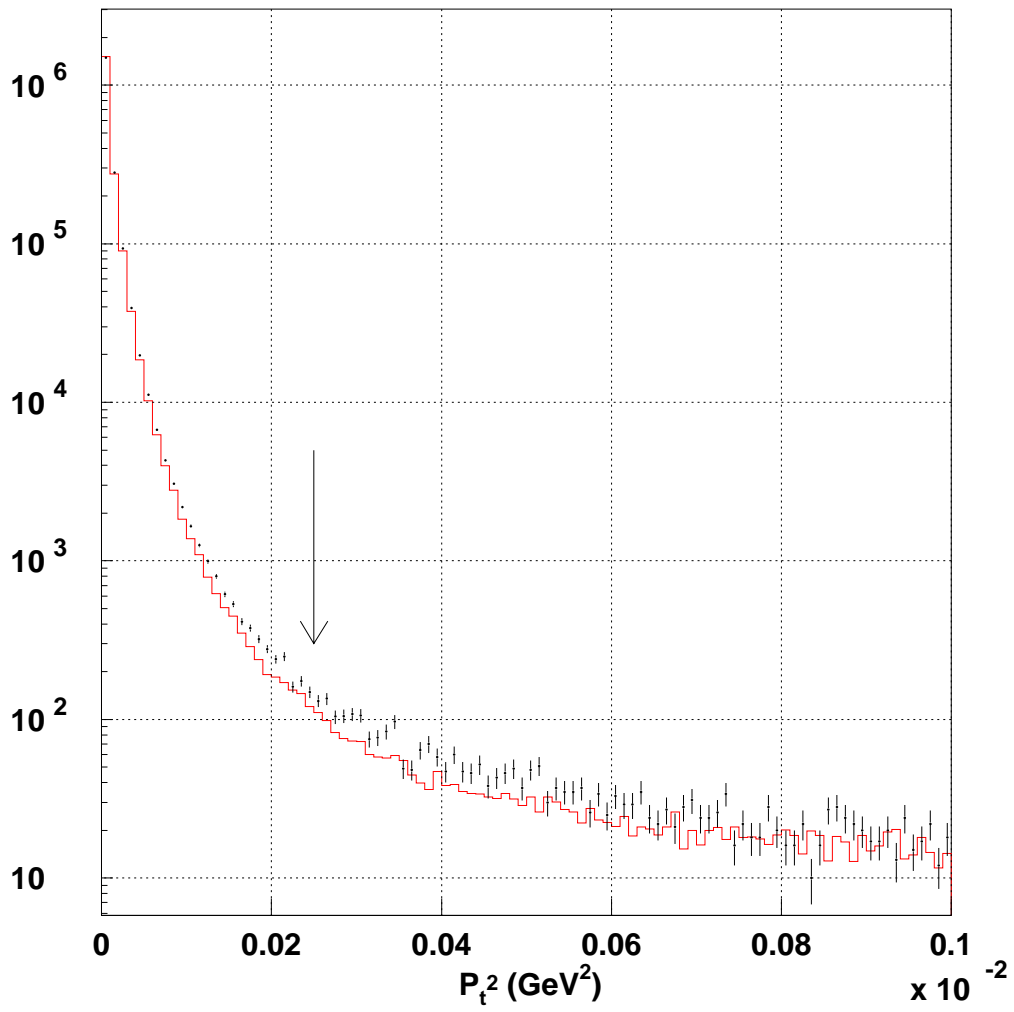
Figure 7.13: Total transverse momentum of the kaon in $\pi^+\pi^-\pi^0$ events. The arrow indicates the cut point.

7.7.1   Drift Chamber System Alignment

The drift chamber system was carefully calibrated using muon runs with no magnetic field applied. However, there are still some uncertainties regarding the position of the drift chambers, particularly the Z positions, as they come from surveys and cannot be determined from data. To evaluate these systematics, we considered possible errors in the determination of certain quantities. We modified certain geometrical parameters in drift chamber 2, leaving all other chambers untouched. The shifts we considered are

$$
\begin{array}{ll}
\delta X & 200\ \mu m \\
\delta Z & 4\ mm \\
\delta \theta & 50\ \mu rad \\
Non-orthogonality & 200\ \mu rad
\end{array}
\tag{7.6}
$$

None of these shifts produced a noticeable effect on the fitted Dalitz parameters. Additionally, we considered a shift in the X target position of $\delta X_t arget = 150\ \mu$m, which did not affect the fitted parameters in a noticeable way either.

7.7.2   Cracks in the Trigger Hodoscope Bank and the Calorimeter

The hodoscope bank is made up of scintillator paddles. There is a small gap between paddles, and a particle can go through it. If this is not simulated correctly, a bias can occur. We studied this bias by masking all the cracks out, i.e. eliminating all events that where within 2 mm of a crack. This did not cause a substantial bias in our measurement.

Similarly, the small gap between adjacent crystals in the calorimeter can cause a bias: a particle can sneak through a gap, effectively depositing *less* than the minimum 0.25 GeV energy in the calorimeter, resulting in the loss of this particle. To estimate the possible bias from this effect, we masked out all crystal cracks by requiring that tracks do not point anywhere closer than 2 mm from any cracks. Again, no substantial systematic arises from this analysis. Both these studies are shown in Figure 7.8.

7.8   Systematic Summary

We determined separate positive and negative systematic uncertainties for each of the Dalitz parameters. The value of the systematic uncertainty takes into account the statistical uncertainty. This is done by integrating a gaussian distribution with a width equivalent to the systematic study's width, and requiring that we integrated are, from the nominal value to the systematic study's value, be 67%. Finally, to evaluate the total error, we added the biggest of the positive and negative systematic uncertainty in quadrature with the statistical error.

CHAPTER 8
ANALYSIS OF OUR RESULT

We have measured the Dalitz parameters for the $K_L \to \pi^+\pi^-\pi^0$ decay. We will now show that the data fits the Dalitz distribution rather well, but it also seems to indicate that our sensitivity might show higher order terms present in the Dalitz cross-section.

8.1   Quality of Fit

Figure 8.1 shows the data and Monte Carlo overlay for invariant mass square of the $\pi^+\pi^-$ system, $M^2_{\pi^+\pi^-}$, which is proportional to the Y Dalitz variable. The Monte Carlo has been reweighted to the fitted Dalitz parameters. If the Dalitz functional form fits the data well, this distribution would be flat, and within statistics it is.

However, this plot shows a slight feature: a small dip below $0.31 GeV^2$, followed by a rise at the very end (notice that the kinematic boundary has already been cut away). Figure 8.2, top center, shows this feature in much better detail. Projecting all of the points onto the Y axis makes the effect less noticeable, as the outer bands in X more or less compensate for the effect. It is very interesting to explore the possible causes of this feature. It could of course be an acceptance problem, but it is nonetheless important to examine this possibility.

8.2   Higher Order Dalitz Parameters?

A possible reason for the feature we have just pointed out is that we are sensitive to higher orders in the expansion of the Dalitz cross-section. Looking at Figure 8.2, we cannot help but wonder about a term of the form $m Y^3$. If we only consider higher order terms that are non-CP violating, The Dalitz function, expanded to third order in the Dalitz variables X and Y would have the form

$$|\mathcal{M}|^2 = 1 + gY + hY^2 + kX^2 + mY^3 + nYX^2, \tag{8.1}$$

Table 8.1 shows the result of adding the Y^3 and YX^2 terms to the fit. The other parameters in the Y Dalitz dimension are affected by this addition in a considerable way. Notice the noticeable improvement in the fit χ^2 from 199.8/180 to 181.9/178. The systematics have been determined in the exact same way we determined them for the nominal analysis.
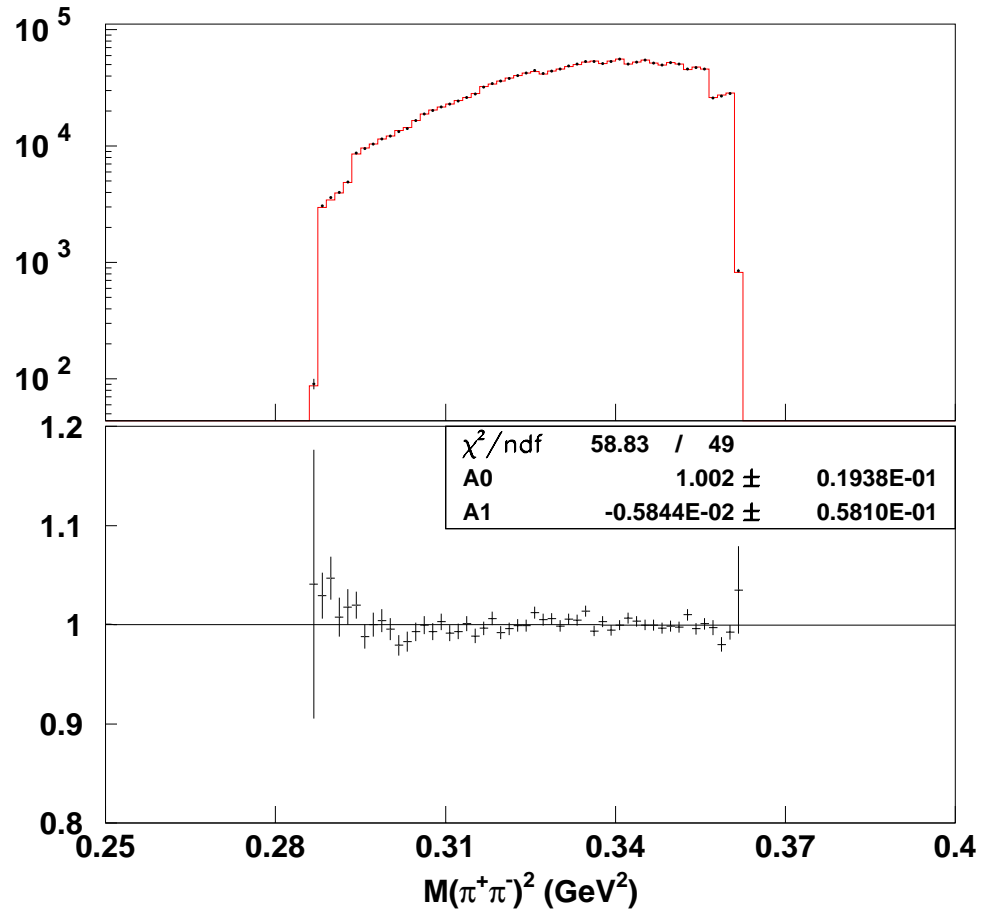
Figure 8.1: Invariant mass distribution for the $\pi^+\pi^-$ system. Top: data (dots) and Monte Carlo, reweighted to the fitted Dalitz parameters. Note that the steps in the distribution are due to the use of the mask to select the events we fit to in the Dalitz plot. Bottom: data/MC distribution.

Figure 8.3 shows the result of reweighting the Monte Carlo by the higher order Dalitz function with the newly fitted parameters. The feature we saw in Figure 8.2 is pretty much gone, and the fits to constants are much better.

Once the systematic errors are taken into account, the n parameter is perfectly consistent with zero, and the m parameter is roughly 1.5 standard deviations from zero. This can hardly be considered proof that we are sensitive to higher order terms, but it is nonetheless suggestive of higher order effects.

g	$0.7168 \pm 0.0057 \ (stat) + 0.0040 \ (syst) - 0.0099 \ (syst) = 0.7168 \pm 0.0114$
h	$0.1069 \pm 0.0045 \ (stat) + 0.0123 \ (syst) - 0.0042 \ (syst) = 0.1069 \pm 0.0131$
k	$0.0219 \pm 0.0011 \ (stat) + 0.0004 \ (syst) - 0.0024 \ (syst) = 0.0219 \pm 0.0027$
m	$-0.0172 \pm 0.0056 \ (stat) + 0.0088 \ (syst) - 0.0050 \ (syst) = -0.0172 \pm 0.0105$
n	$0.0036 \pm 0.0026 \ (stat) + 0.0068 \ (syst) - 0.0024 \ (syst) = 0.0036 \pm 0.0073$
χ^2	181.9 for 178 d.f.

Table 8.1: Higher order Dalitz parameter fit. We include the higher order terms in Equation 8.1. The total error has been calculated as the sum (in quadrature) of the statistical and the biggest of the positive or negative systematic errors.
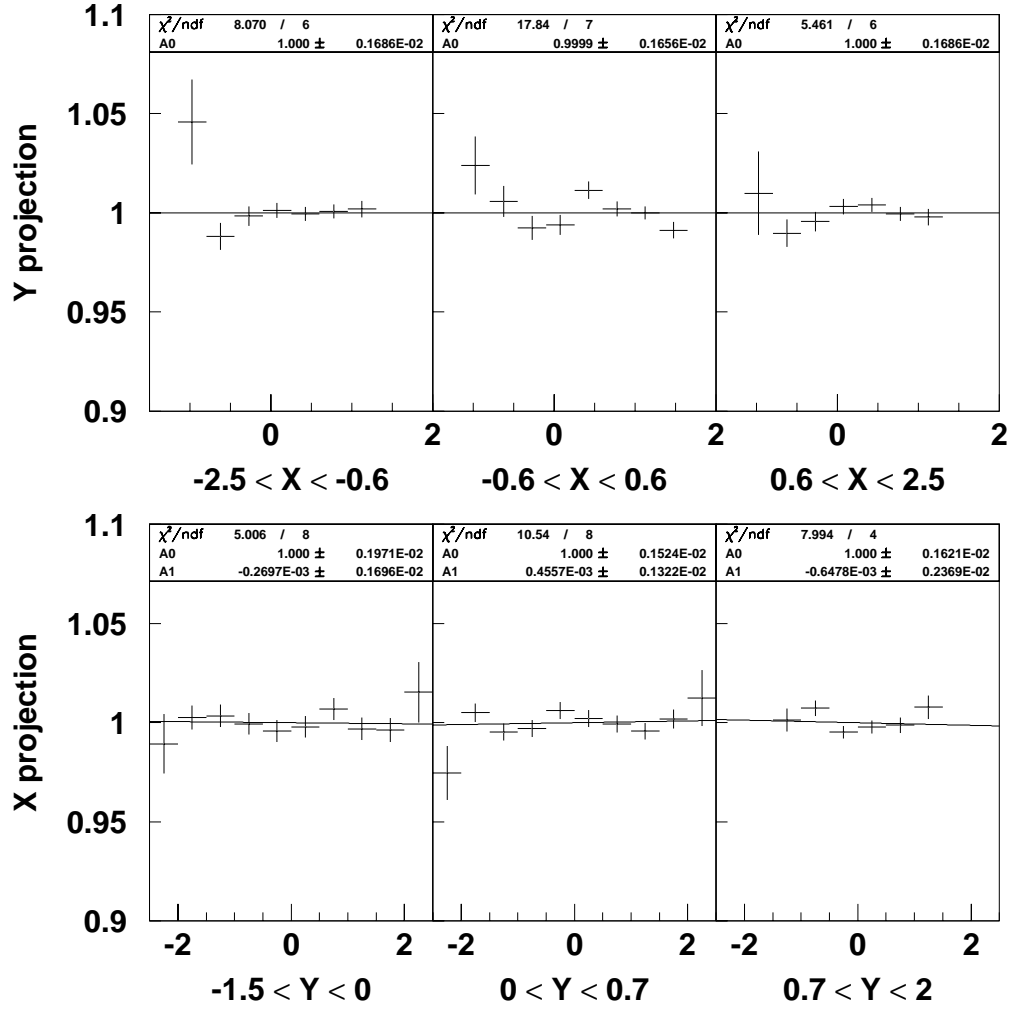
Figure 8.2: X and Y Dalitz variable data and Monte Carlo overlays. Top: Bottom: Y slices projected onto the X axis. The Monte Carlo is reweighted to the nominal fitted Dalitz parameters (g, h, k in Table 6.3). If the nominal fit function were perfect, these plots would be flat. However, there are features in the Y Dalitz projections, particularly i the middle plot. Notice the wiggle we see in the middle plot and how well it fits a 3rd order polynomial. Bottom: Same but the projections are now onto the X Dalitz variable, which are flat within statistics.

96
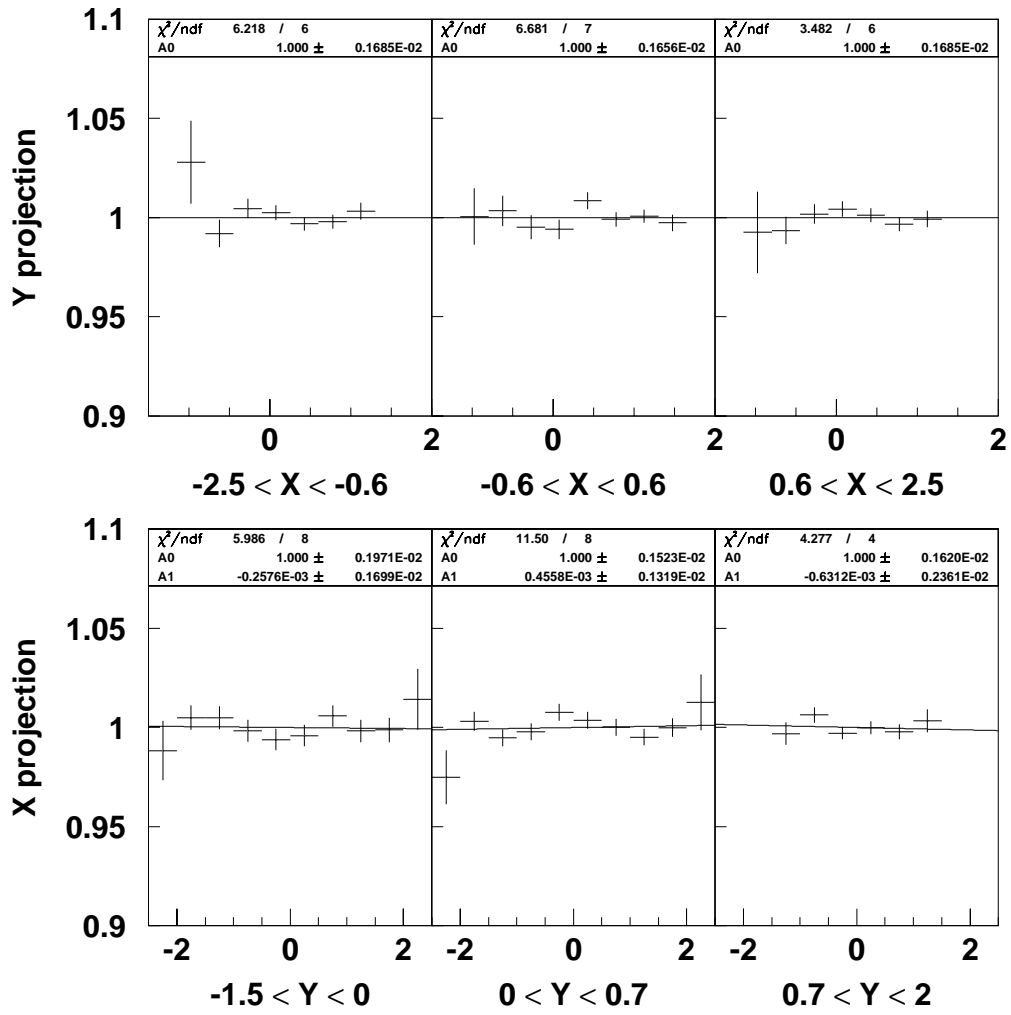
Figure 8.3: X and Y Dalitz variable data and Monte Carlo overlays, with higher order terms. The Monte Carlo has been reweighted by the higher-order fit distribution. Notice that the feature seen in Figure 8.2 is pretty much gone, and that the χ^2 is better.
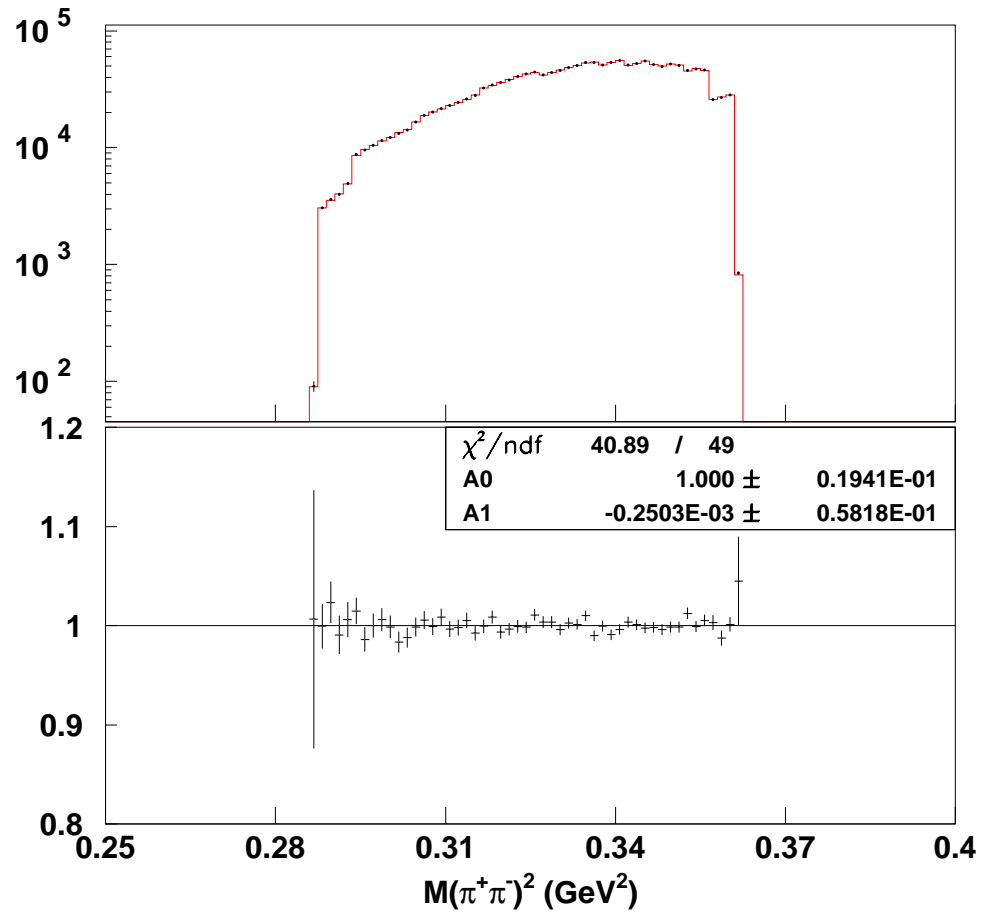
Figure 8.4: Invariant mass distribution for the $\pi^+\pi^-$ system, after fitting with the higher order function. Compare this to Figure 8.1, note that the feature mentioned in the text is gone, and that the χ^2 is much better.
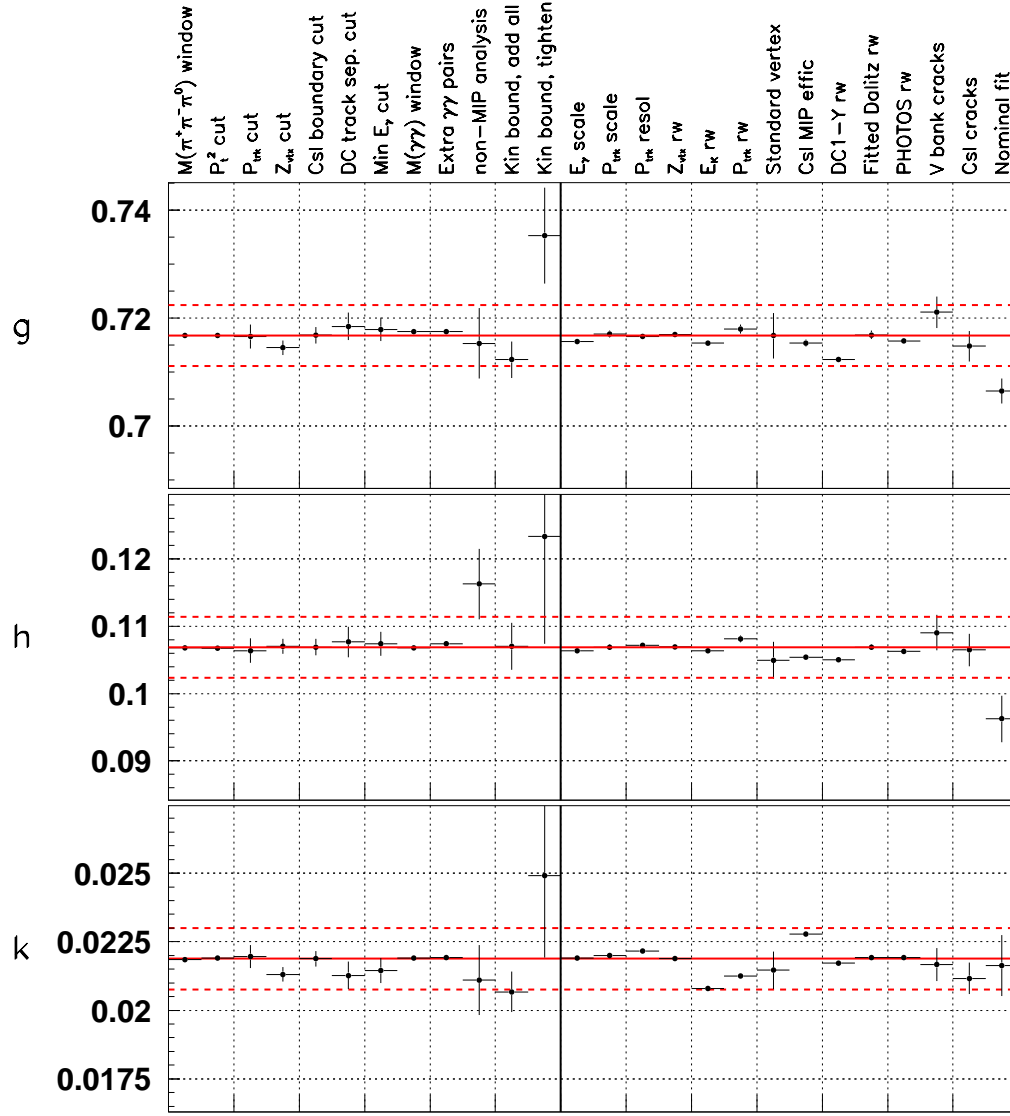
Figure 8.5: Systematic studies for higher order fit. Compare to Figure 7.8. Note that the error bars for g are bigger than the ones in the nominal fit by about a factor of two.
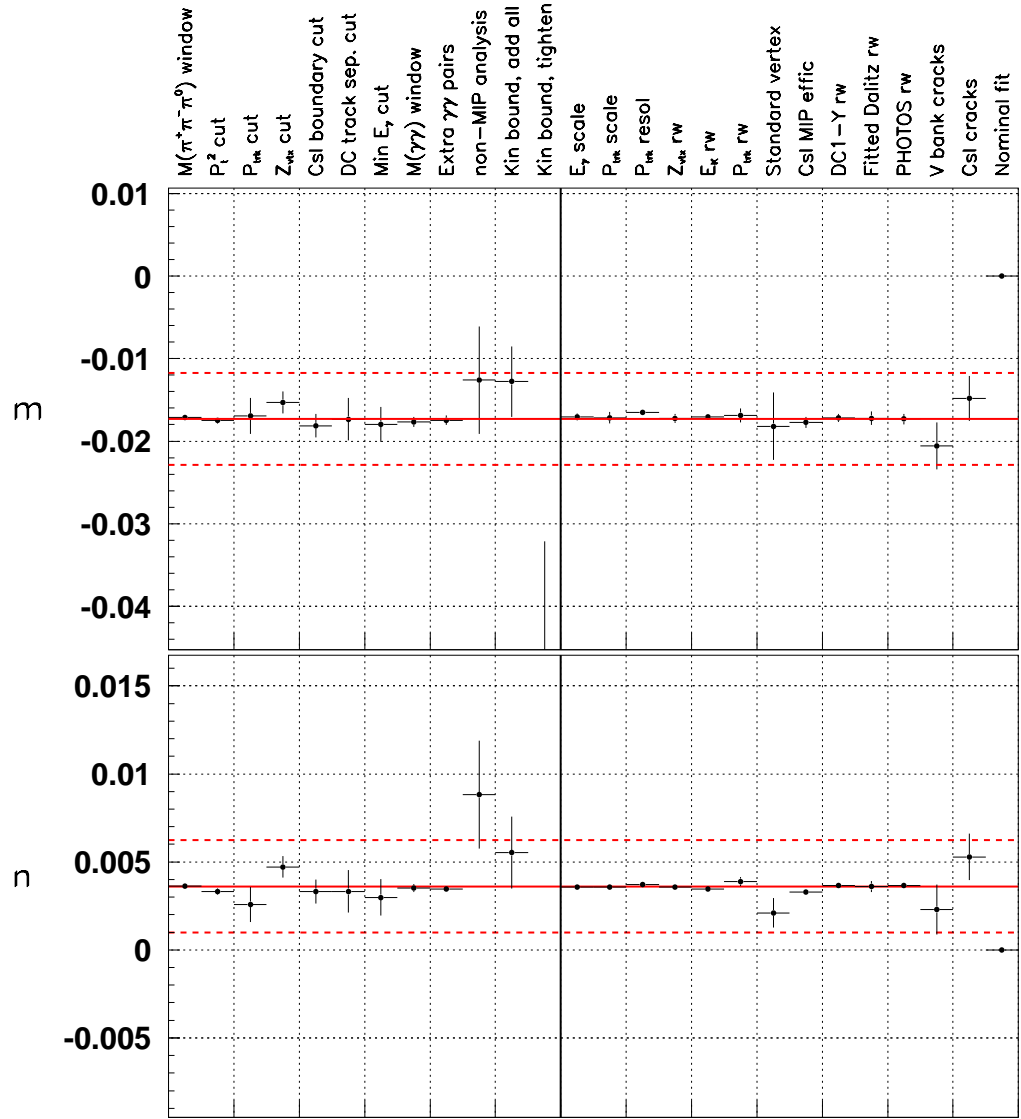
Figure 8.6: Systematic studies for m, n, for higher order fit.

CHAPTER 9
CONCLUSION

Using data from the 1997 KTeV experiment run, we have measured the Dalitz parameters for the $K_L \to \pi^+\pi^-\pi^0$ decay. We find the following values for the measured parameters

$$
\begin{aligned}
g &= 0.7065 \pm 0.0023 \ (stat) + 0.0074 \ (syst) - 0.0051 \ (syst) \ , \\
h &= 0.0962 \pm 0.0034 \ (stat) + 0.0130 \ (syst) - 0.0031 \ (syst) \ , \\
k &= 0.0216 \pm 0.0011 \ (stat) + 0.0004 \ (syst) - 0.0024 \ (syst) \ .
\end{aligned}
\tag{9.1}
$$

For the final result, we evaluated the systematic error for positive and negative deviations separately. Only those deviations that are statistically significant have been taken into account (see Figure 7.8). The final result is

$$
\begin{aligned}
g &= 0.7065 \pm 0.0077 \ , \\
h &= 0.096 \pm 0.013 \ , \\
k &= 0.0216 \pm 0.0026 \ .
\end{aligned}
\tag{9.2}
$$

For the slope parameter g, the leading positive systematic uncertainty comes from the analysis of the sample with no "Minimum Ionizing Particle" (MIP) energy cut, while the leading negative systematic uncertainty comes from the discrepancy in Y illumination at the drift chambers. In each case, the total error is calculated by taking the statistical error and the biggest of the two systematic uncertainties and adding them in quadrature. Figure 9.1 shows a history of the measurements of the Dalitz parameters. One should compare our result with the 1998 result from CPLEAR [12], which is based on 500K events. The difference in statistical error between their result and ours is consistent with our bigger 1.6 million events sample, but their quoted systematic errors are generally smaller.

9.1 Theoretical Implications

9.1.1 Isospin Symmetries

The form factors for various $K \to \pi$ decays can be related by the isospin symmetry of the 3π final state [5]. It may be possible to use Chiral Perturbation Theory to predict
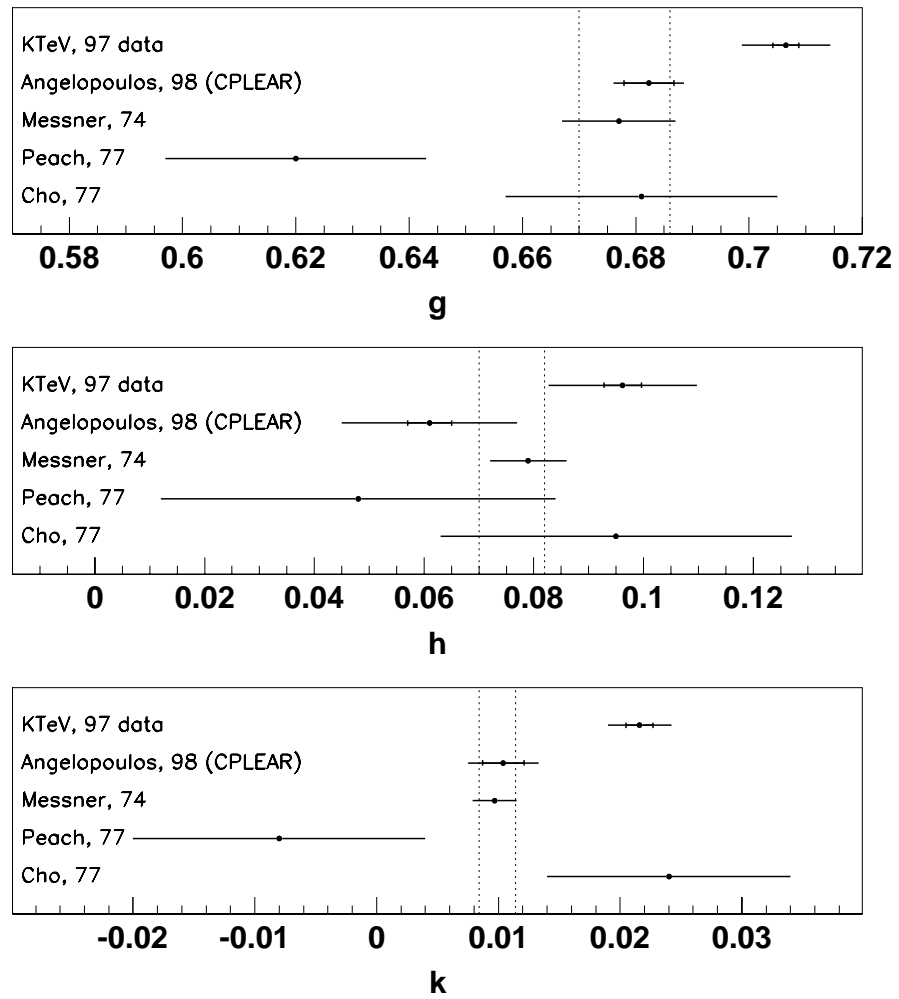
Figure 9.1: History of $K_L \to \pi^+\pi^-\pi^0$ Dalitz parameter measurements. The error bars indicate total errors, with small vertical bars indicating the statistical error in the two most recent measurements. The dotted lines indicate the error band according to PDG-2000 [8].

$\pi\pi$ phase shifts near threshold[1] [6]. This makes new and improved measurements of the form factors for kaons to 3π final states very important and useful. Consider the following quantities

$$R_{+-0} = h + 3k - \frac{g^2}{4cos^2\beta} \ , \qquad R_{000} = 2h_{000} \ . \tag{9.3}$$

where g, h, and k are the Dalitz parameters for $\pi^+\pi^-\pi^0$ decays, β is a final state strong interaction phase in $\pi^+\pi^-\pi^0$ decays, and h_{000} is the quadratic Dalitz slope in $\pi^0\pi^0\pi^0$ decays. Isospin symmetry predicts that

$$R_{+-0} = R_{000} \ . \tag{9.4}$$

Previous attempts at testing this relationship have assumed the phase shift β to be negligible and have compared the values for the R_{+-0} and R_{000}, obtained with the measurements available at the time [5] (PDG-1990 [25]). This had shown remarkably good agreement between R_{+-0} and R_{000}. Table 9.1 shows the values of the R_{+-0} and R_{000} parameters obtained for various experiments, assuming $\beta = 0$. For R_{000}, the values of h_{000} used are the ones corresponding to the E731 [26] and the NA48 [27] experiments[2]. If the $\beta = 0$ assumption is correct, the values in the left column should be the same as the ones in the right column.

Another approach is to use Equation 9.3 to *determine* the value of $cos^2\beta$

$$cos^2\beta \ = \frac{g^2}{4\left(h + 3k - 2h_{000}\right)}. \tag{9.5}$$

We can calculate the value of $cos^2\beta$ for the experiments considered in the measurement of the $\pi^+\pi^-\pi^0$ Dalitz parameters, taking the value of the quadratic $3\pi^0$ Dalitz slope, h_{000}, as the weighted average between the E731 result, $h_{000} = (-3.3 \pm 1.3) \ 10^{-3}$, and the NA48 result, $h_{000} = (-6.1 \pm 1) \ 10^{-3}$, that is:

$$\langle h_{000} \rangle = (-5.1 \pm 0.8) \ 10^{-3}. \tag{9.6}$$

It is important to point out that the value of $cos^2\beta$ is not very sensitive to the value of because this value is added together with $h + 3k$, which is about 30 times bigger than h_{000}.

Correlations between the g, h, and k parameters play an important role in the determination of the systematic error for $cos^2\beta$. If we take a look at the systematics for the Dalitz parameters, Figure 7.8, we see that the two main systematics in g and

---

[1]low-energy $\pi\pi$ states

[2]The E731 measurement is the only h_{000} measurement in PDG, the NA48 measurement has not been incorporated yet.

	R_{+-0}	R_{000}
PDG-94	-0.0064 ± 0.0095	-0.0066 ± 0.0026
CPLEAR-98	-0.0241 ± 0.0183	
NA48-2001		-0.0122 ± 0.002
KTeV-97 run	$+0.036 \pm 0.015$	

Table 9.1: R_{+-0} and R_{000} values calculated for various Dalitz measurements. Here we have assumed the strong interaction final state phase $\beta = 0$. If this assumption is correct, any of the values in the left column should be equal to the values in the right column (and equal among themselves, of course).

h drive these numbers in the same direction. Since they are in the numerator and denominator of Equation 9.5, the effect of a systematic, such as the analysis with no MIP energy cut, tends to cancel out. This is indeed very nice, as the systematic biases in the measurement of $cos^2\beta$ tend cancels out in the ratio of parameters, making this measurement less prone to acceptance problems. We evaluate the systematic errors in $cos^2\beta$ by calculating its value for each of the systematic studies, just as we did with the Dalitz parameters themselves, and we obtain [3]

$$
\begin{aligned}
cos^2\beta &= 0.729 \pm 0.026 \ (stat) + 0.026 \ (syst) - 0.038 \ (syst) \\
&= 0.729 \pm 0.046 \ , \\
\beta &= 31.4° \pm 3.0°.
\end{aligned}
\tag{9.7}
$$

Figure 9.2 shows the $cos^2\beta$ values for the different experiments. Note that CPLEAR gets a bigger error in this quantity than KTeV does [4]. This is due to the way the values of the actual parameters relate in the determination of $cos^2\beta$ and its error. Moreover, we do not know what the correlations for various systematic studies are. However, since CPLEAR's error for the h parameter is much bigger than the other two, the error would probably not change much should one consider the correlations.

Averaging all measurements, we get

$$
\begin{aligned}
cos^2\beta &= 0.798 \pm 0.038 \ , \\
\beta &= 26.7° \pm 2.7°, \\
\chi^2 &= 11.1 \ / \ 4 \ d.f.
\end{aligned}
\tag{9.8}
$$

---

[3]If we instead propagate from the total errors in g, h, and k, we obtain $cos^2\beta = 0.729 \pm 0.080$.

[4]From the CPLEAR Dalitz parameters, we get $cos^2\beta = 1.115 \pm 0.185$.

KTeV, 97 data

Angelopoulos, 98 (CPLEAR)

Messner, 74

Peach, 77

Cho, 77

$<\cos^2\beta> = 0.786 \pm 0.037$

$\chi^2 = 11.2 \, / \, 4$ d.f.

$\cos^2\beta$
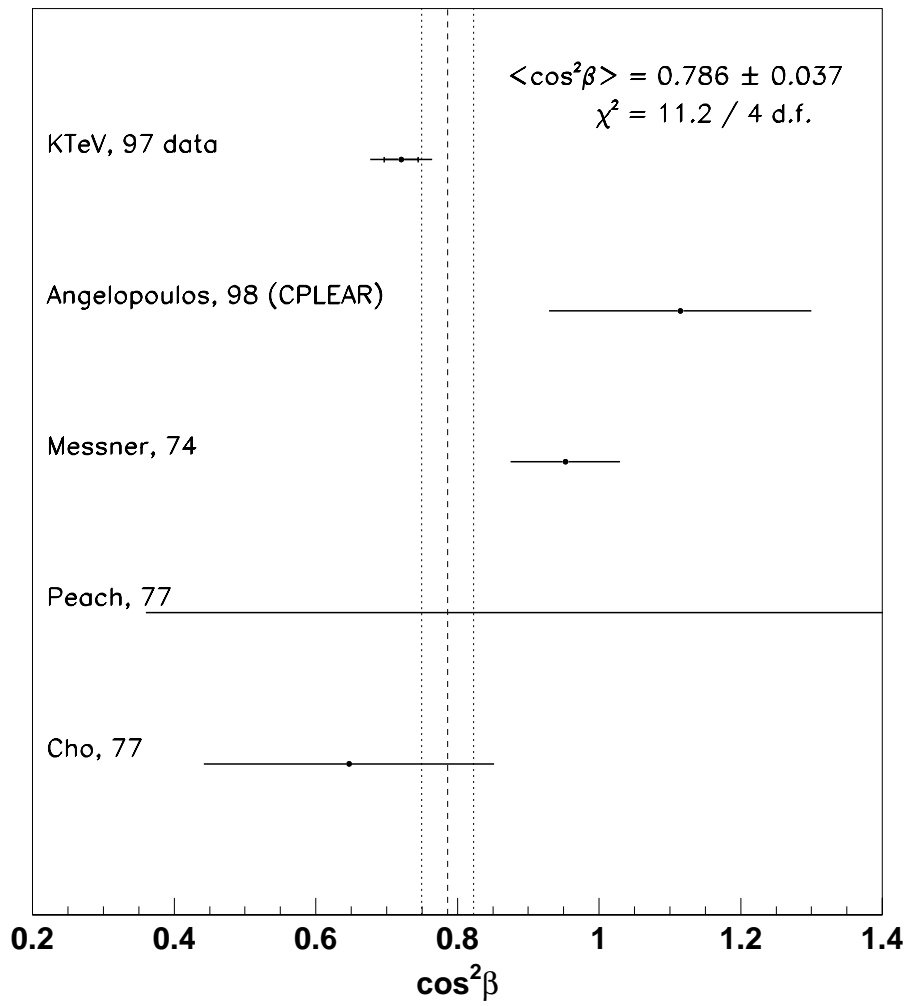
Figure 9.2: $cos^2\beta$ values, calculated for various Dalitz parameters measurements. The bands indicate the average and error (including the KTeV result). The smaller error bars in the KTeV result denote the statistical error, while the total error bar includes the systematic error.

9.1.2   Higher Order terms in the Dalitz Distribution

In Chapter 8 we took a look at the possibility that our data could show sensitivity to higher order terms in the Dalitz expansion in the X and Y Dalitz variables. Having found a value for the Y^3 parameter that is 1.5 standard deviations from zero, the evidence for higher order terms is suggestive rather than conclusive. It is, nonetheless, an interesting possibility.

9.2   Final Comments

We determined the Dalitz parameters using data from KTeV's 1997 run. Our systematic uncertainty could be improved if we understand the issues related to illumination discrepancies and the analysis with no MIP energy cut.

Our measurement of the Dalitz parameters, together with theoretical efforts to understand the $K_L \to 3\pi$ final state phases, might provide some interesting physics insight.

APPENDIX A
KAON PHENOMENOLOGY

To give a more complete picture of the $K_L \to \pi^+\pi^-\pi^0$ decay, we would like to describe the kaon system in some more detail. This will allow us to understand why the K_L is the main contribution to $\pi^+\pi^-\pi^0$ final states from neutral kaons.

A.1   Kaon Phenomenology

The formalism of neutral kaon decays into three mesons is covered in many articles [28] [5] [6], and we will not develop it here. We will highlight a few important concepts and their relationship to neutral kaon decays into a three-pion final state. Consider the eigenstates of the strong interaction Hamiltonian (H_S), K_0 and $\overline{K}_0$

$$|K_0\rangle = |d\,\overline{s}\rangle\,, \quad |\overline{K}_0\rangle = |\overline{d}\,s\rangle\,. \tag{A.1}$$

Under a CP transformation, these states transform into each other

$$CP\,|K_0\rangle = |\overline{K}_0\rangle\,, \quad CP\,|\overline{K}_0\rangle = |K_0\rangle\,. \tag{A.2}$$

The weak interaction Hamiltonian (H_W), however, mixes these two states. To find eigenstates of H_W, let us first define two CP eigenstates in terms of K_0 and $\overline{K}_0$

$$\begin{aligned}
|K_1\rangle &\equiv \tfrac{1}{\sqrt{2}}\left(|K_0\rangle + |\overline{K}_0\rangle\right) \quad (CP = +1), \\
|K_2\rangle &\equiv \tfrac{1}{\sqrt{2}}\left(|K_0\rangle - |\overline{K}_0\rangle\right) \quad (CP = -1).
\end{aligned} \tag{A.3}$$

These are still eigenstates of H_S because the strong interaction conserves CP (to the best of our knowledge anyway). If CP were conserved by H_W, these would have to be eigenstates of it as well.

Lets consider the lifetime of these eigenstates. If CP were a good symmetry of nature, K_1 would only decay to states with $CP = +1$, i.e. two-pion states, whereas K_2 would only decay to states with $CP = -1$, i.e. a three-pion or a semileptonic state. This would result in a big difference in lifetimes, as the phase space available for a decay into two mesons is much larger than the one available for a three meson final state. This is indeed the case: short-lived and a long-lived kaons have been identified. It is then natural to associate these states with K_1 and K_2, respectively.

However, in 1964 Cronin, Fitch and their collaborators [29] observed that it is possible for a long-lived kaon to decay into a two-pion final state, effectively violating CP symmetry. This means that CP is not a symmetry of H_W, which in turn means that the eigenstates are not CP invariant but rather are a mix of the two states K_1 and K_2. Since the number of events observed violating CP is small, the eigenstates of H_W have to be K_1 (K_2) with a small mixture of K_2 (K_1). Defining K_S as the short-lived of the two neutral kaons, and K_L as the long-lived one, the (non-CP invariant) eigenstates of H_W are

$$
\begin{aligned}
|K_S\rangle &= \tfrac{1}{\sqrt{1+|\epsilon|^2}} \left(|K_1\rangle + \epsilon |K_2\rangle \right) \\
&= \tfrac{1}{\sqrt{2(1+|\epsilon|^2)}} \left[(1+\epsilon) |K_0\rangle + (1-\epsilon) |\overline{K}_0\rangle \right] \qquad \text{(A.4)} \\
|K_L\rangle &= \tfrac{1}{\sqrt{1+|\epsilon|^2}} \left(|K_2\rangle + \epsilon |K_1\rangle \right) \\
&= \tfrac{1}{\sqrt{2(1+|\epsilon|^2)}} \left[(1+\epsilon) |K_0\rangle - (1-\epsilon) |\overline{K}_0\rangle \right] \qquad \text{(A.5)}
\end{aligned}
$$

where the ϵ parameter represents the mixing of the two CP states, and is of order 2×10^{-3}. Note that these states are still eigenstates of H_S. The important issue we want to focus on is that K_S (K_L) are "almost" CP +1 (-1) states, as ϵ is a very small number.

A.2 $\quad K_L \to \pi^+\pi^-\pi^0$

The first question we can ask is: Why consider only the K_L decays to $\pi^+\pi^-\pi^0$? The short answer is that K_S decays to three pions are either CP or kinematically suppressed. There are two contributions to the CP eigenvalue of the final state. First is the angular momentum. The kaon is a scalar particle, so the total angular momentum of the final state has to be zero. The pions are also scalar particles, but there is an orbital contribution to the total angular momentum. Since the total angular momentum is zero, the relative angular momentum between the $\pi^+\pi^-$ has cancel the orbital angular momentum between the $\pi^+\pi^-$ system and the π^0 . Say l is the value of this angular momentum. The eigenvalue of the C operation on the $\pi^+\pi^-\pi^0$ state is $(-1)^l$, coming from the interchange of the charged pions. On the other hand, the eigenvalue of the P operation is the product of the intrinsic parities of the particles (-1^3) and the total angular momentum of the system (which is zero). So CP has an eigenvalue of $(-1)^{l+1}$. Now, since the sum of the pion masses is close to the kaon mass, the states with angular momentum $l > 1$ are kinematically suppressed. For $l = 0$, the $K_S \to \pi^+\pi^-\pi^0$ decays are CP suppressed. For $l = 1$, $K_S \to \pi^+\pi^-\pi^0$ is not CP-suppressed but is kinematically suppressed. This shows that the K_S contribution to the $\pi^+\pi^-\pi^0$ final state is strongly suppressed. Experimentally, the $K_L \to \pi^+\pi^-\pi^0$ branching ratio is roughly 13% whereas the $K_S \to \pi^+\pi^-\pi^0$ is about 4×10^{-7}. For this reason, we will only

consider K_L decays in the measurement of the Dalitz parameters, we do not have enough K_S events to determine the CP violating component of the decay.

APPENDIX B
DATA CRUNCH

In this appendix we will give some details about the steps required to obtain the final $\pi^+\pi^-\pi^0$ sample for the Dalitz measurement.

B.1 Crunch from split tapes: First stage

We crunched over the entire 1997 $\pi^+\pi^-\pi^0$ split tapes (KZP057 - KZP182), obtaining a set of 20 output tapes (KQH270 - KQH289). There were no kinematic cuts applied here except for a track-photon separation of $25cm$. The Veto cuts applied are as follows:

```
IOPTREG            = 3,
USE_INTIME         = T,
USE_MACOR          = T,
USE_RCSRC          = T,
USE_SASRC          = F,
USE_MASRC          = F,
USE_CASRC          = F,
USE_BA1SRC         = F,
USE_BA3SRC         = F,
USE_REGSRC         = F,
USE_DUMSRC         = 7*F,
USE_RCNGH          = F,
USE_SANGH          = F,
USE_MANGH          = F,
USE_CANGH          = F,
USE_BA1NGH         = F,
USE_BA3NGH         = F,
USE_DUMNGH         = 8*F,
USE_INPRS_DC4      = T,
USE_96PRL          = F,
EVTO_RC_CUT        = 1.0000000E+08,
EVTO_SA_CUT        = 1.0000000E+08,
EVTO_MA_CUT        = 1.0000000E+08,
EVTO_CA_CUT        = 1.0000000E+08,
```

```
EVTO_BA1_CUT        = 1.0000000E+08,
EVTO_BA3_CUT        = 1.0000000E+08,
EVTO_REG_CUT        = 1.0000000E+08,
EVTO_REGPB_CUT      = 1.0000000E+08,
EVTO_XCLUS_CUT      = 1.0000000E+08,
VTO_NTRK_CUT        = 10000.00,
VTO_NVVSRC_CUT      = 10000.00,
VTO_INPRS_TOT_CUT   = 10000.00,
VTO_INPRS_234_CUT   = 10000.00,
VTO_NXCLIN_CUT      = 10000.00,
ITHRESH_XRC         = 0
```

For the Fiducial cuts, we have:

```
Mask clearance                  :        0.0030000
V0 clearance                    :        0.0020000
V1 clearance                    :        0.0020000
CA clearance                    :        0.0020000
CSI outside edge clearance  :        0.0290000
CIA clearance                   :    -10000.0000000
Track Sep (m)                   :    -10000.0000000
Track Sep (Cells)               :    -10000.0000000
Track Sep (Wire centered cells):   -999.0000000
Minimum beam distance (cells):    -999.0000000
Maximum beam distance (cells):   9999.0000000
Min Ch 1 X edge dist  (cells):         14
Min Ch 1 Y edge dist  (cells):         46
Min Ch 2 X edge dist  (cells):         40
Min Ch 2 Y edge dist  (cells):         40
Min Ch 3 X edge dist  (cells):         62
Min Ch 3 Y edge dist  (cells):         26
Min Ch 4 X edge dist  (cells):         50
Min Ch 4 Y edge dist  (cells):         20
```

B.1.1   Special selection: Second stage

After the first crunch from the split tapes, we generated a second stage tape (KQH398) with the following selection:

- Both tracks have $E_{trk,CsI} < 1$ GeV (our nominal sample); or

- Events pass a $5\times$ prescale (for systematic studies).

Each of these two conditions was tagged using IEVTAG(4) bits (20 and 21, respectively). These bits are normally used only in Monte Carlo, so it is safe to use them

for tagging purposes. All other cuts, including Veto and Fiducial cuts, were the same as in the crunch from the split tapes. From this tape we generated the ntuples that we used for the final analysis.

B.1.2 Ntuple generation

From tape KQH398, we generated ntuples. The Veto cuts applied during ntuple generation were:

```
 IOPTREG =              3,
 USE_INTIME      = T,
 USE_MACOR       = T,
 USE_RCSRC       = T,
 USE_SASRC       = F,
 USE_MASRC       = T,
 USE_CASRC       = F,
 USE_BA1SRC      = F,
 USE_BA3SRC      = F,
 USE_HASRC       = F,
 USE_REGSRC      = F,
 USE_DUMSRC      = 7*F,
 USE_RCNGH       = F,
 USE_SANGH       = F,
 USE_MANGH       = F,
 USE_CANGH       = F,
 USE_BA1NGH      = F,
 USE_BA3NGH      = F,
 USE_DUMNGH      = 9*F,
 USE_INPRS_DC4   = T,
 USE_96PRL       = F,
 EVTO_RC_CUT     =  1.0000000E+09,
 EVTO_SA_CUT     =  0.3000000    ,
 EVTO_MA_CUT     =  0.1000000    ,
 EVTO_CA_CUT     =   1000000.    ,
 EVTO_BA1_CUT    =   1000000.    ,
 EVTO_BA3_CUT    =  1.0000000E+08,
 EVTO_HA_CUT     =  1.0000000E+08,
 EVTO_REG_CUT    =   2.000000    ,
 EVTO_REGPB_CUT  =  0.7000000    ,
 EVTO_XCLUS_CUT  =   1.000000    ,
 VTO_NTRK_CUT    =   10000.00    ,
 VTO_NVVSRC_CUT  =   10000.00    ,
 VTO_INPRS_TOT_CUT      =    10000.00    ,
```

```
VTO_INPRS_234_CUT         =     10000.00      ,
VTO_NXCLIN_CUT   =    10000.00      ,
ITHRESH_XRC      =             0,
IHASRC  =             0
```

whereas the Fiducial cuts were:

```
Mask clearence                 :        0.0030000
V0 clearence                   :        0.0020000
V1 clearence                   :        0.0020000
CA clearence                   :        0.0020000
CSI outside edge clearence  :        0.0290000
CIA clearence                  :   -10000.0000000
Track Sep (m)                  :   -10000.0000000
Track Sep (Cells)              :   -10000.0000000
Track Sep (Wire centered cells):        3.0000000
Minimum beam distance (cells):        0.0000000
Maximum beam distance (cells):    9999.0000000
Min Ch 1 X edge dist  (cells):          14
Min Ch 1 Y edge dist  (cells):          46
Min Ch 2 X edge dist  (cells):          40
Min Ch 2 Y edge dist  (cells):          40
Min Ch 3 X edge dist  (cells):          62
Min Ch 3 Y edge dist  (cells):          26
Min Ch 4 X edge dist  (cells):          50
Min Ch 4 Y edge dist  (cells):          20
```

The resulting ntuples were used for the analysis. Notice the cell separation cut and some of the other cuts, which in the ntuple stage have been tightened. In these cases, the tightened cut did *not* reject events, but rather tagged them. We used these tags to study systematics such as the cell separation cut.

As for Monte Carlo, the same Veto and Fiducial cuts were applied during the generation crunch as in the first stage of the data crunching (no track-photon separation was applied though). The last stage, the generation of ntuples, used the same Veto and Fiducial cuts as the corresponding stage in the data handling.

APPENDIX C
MASS CONSTRAINTS IN VERTEX RECONSTRUCTION

In this appendix we will explain the details of vertex optimization in $\pi^+\pi^-\pi^0$ events using mass constraints.

Once we have identified a good event, it is possible to use mass constraints to improve the determination of kinematic variables. This is particularly useful when determining the vertex position in the decay region. To illustrate this, lets first consider $\pi^+\pi^-$ decays. In this case, it is possible to determine the Z position of the vertex if we know the momentum and position of the tracks at the vacuum window and impose the mass constraint

$$M_K^2 = (P_1 + P_2)^2 = 2m_{\pi^+}^2 + m_{\pi^+}^2\left(\frac{p_1}{p_2} + \frac{p_1}{p_2}\right) + 2p_1p_2\left(1 - cos\theta\right) + O\left(\left(\frac{m}{p}\right)^4\right) \quad \text{(C.1)}$$

where θ is the opening angle between the pions. Using the above equation, we can solve for the angle θ. However, this angle is also related to the distance between the tracks at the vacuum, R_{12}, and the distance from the vacuum window to the vertex, Z_{V-W}:

$$\theta \approx \frac{R_{12}}{Z_{V-W}} \ . \quad \text{(C.2)}$$

If we use the tracking information to find the position of the tracks at the vacuum window, we can calculate the distance to the vertex.

In $\pi^+\pi^-\pi^0$ events, it is possible to use a similar mass constraint requirement. Figure C.1 shows the positions and angles of particles in the decay volume. The mass constraint in Equation C.1 takes the form

$$
\begin{aligned}
M_K^2 &= (P_1 + P_2 + P_2)^2 \\
&= 2m_{\pi^+}^2 + m_{\pi^0}^2 + +m_{\pi^+}^2\left(\frac{p_1}{p_2} + \frac{p_2}{p_1}\right) + m_{\pi^+}^2\left(\frac{p_3}{p_1} + \frac{p_3}{p_2}\right) + m_{\pi^0}^2\left(\frac{p_1}{p_3} + \frac{p_2}{p_3}\right) \\
&\quad + 2\left[p_1p_2\left(1 - cos\theta_{12}\right) + p_1p_3\left(1 - cos\theta_{13}\right) + p_2p_3\left(1 - cos\theta_{23}\right)\right] + O\left(\left(\frac{m}{p}\right)^4\right) \ .
\end{aligned}
$$
$$\text{(C.3)}$$

We also have

$$R_{ij} \approx Z_{V-W} \times \theta_{ij} \ , \quad \text{(C.4)}$$
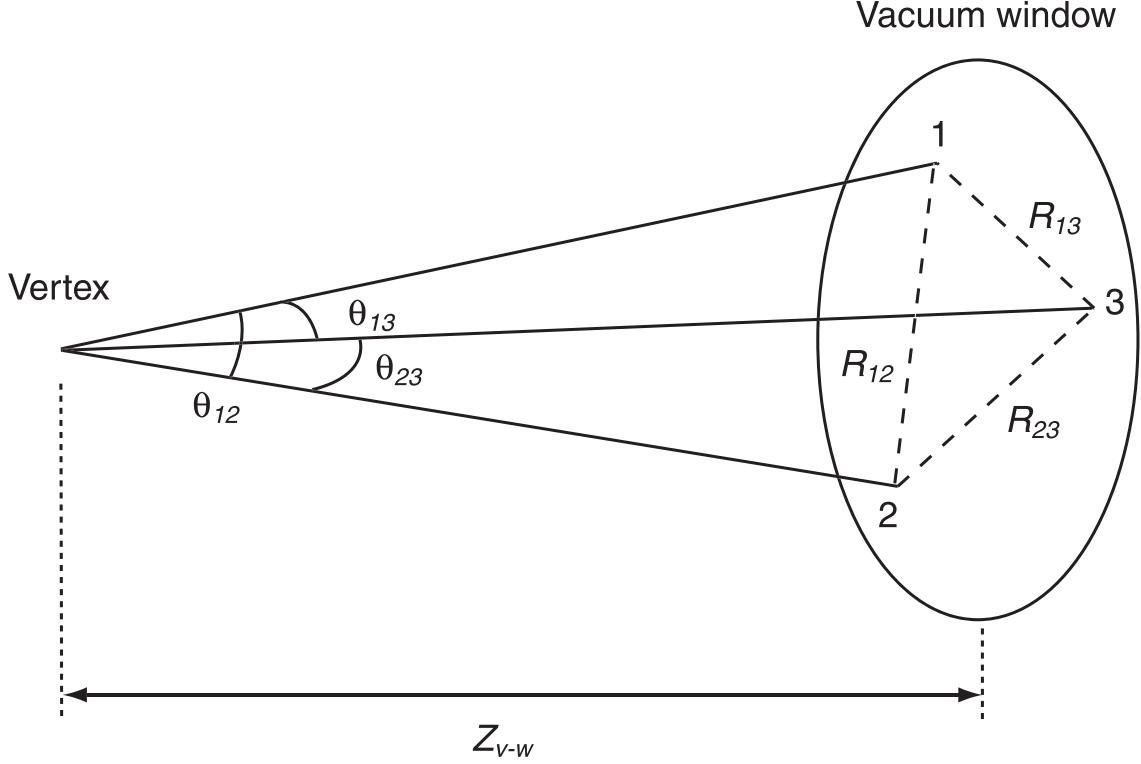
and we can make the approximation

Figure C.1: Positions, angles, and distances of particles between the vertex position and the vacuum window. The indices $1, 2, 3$ correspond to pi^+, pi^-, pi^0, respectively.

$$\theta_{ij}^2 \approx 2\left(1 - cos(\theta_{ij})\right) \ . \tag{C.5}$$

Multiplying R_{ij} by $p_i p_j$ and adding, we get

$$\begin{aligned} R_{12}^2 p_1 p_2 + R_{13}^2 p_1 p_3 + R_{23}^2 p_2 p_3 = \\ Z_{V-W}^2 \times 2\left[p_1 p_2\left(1 - cos\theta_{12}\right) + p_1 p_3\left(1 - cos\theta_{13}\right) + p_2 p_3\left(1 - cos\theta_{23}\right)\right] \ . \end{aligned} \tag{C.6}$$

The second term on the r.h.s. of the expression above can be obtained from Equation C.3. Once this is done, we can solve for Z_{V-W}^2 in Equation C.6, obtaining the distance from the vertex to the vacuum window. There is a caveat: the point at which the π^0 intersects the vacuum window is determined using the position of the vertex itself, so the solution to the problem is not so straightforward. The procedure is as follows

1. Start from the standard vertex;

2. Calculate the position of the π^0 at the vacuum window;

3. Calculate the new vertex position using the mass constraint;

4. If the new and old vertex positions differ by more than 1 mm, go back to Step 2 and iterate.

This procedure converges very fast, rendering a very significant improvement in resolution. This can be seen both when comparing reconstructed and generated Monte Carlo distributions, as shown in Figure 6.4, and when comparing the "missing particle momentum" resolution between data and Monte Carlo, as illustrated by Figure 6.8.

There are a few reasons why this is a better way to determine the Z vertex:

- For small opening angles, the standard vertex, calculated by track extrapolation, has a bigger uncertainty. This is especially important at the upstream end of the decay region;

- Tracks can scatter at the vacuum window. Our method is impervious to this problem;

One important difference between this method of obtaining the vertex position is that the mass constraint requires an accurate charge momentum measurement. If there is a problem with momentum reconstruction, such as a scale problem, the vertex position calculated from the mass constraint can be biased. However, by the same token one can argue that even if there is a problem with momentum reconstruction, imposing a mass constraint renders the most physical reconstructed kinematic quantities. The effect of using the standard vertex position reconstruction instead of this mass-constrained version has been included in the systematic studies.

APPENDIX D
MEASUREMENT OF THE BRANCHING RATIO AND FORM FACTORS FOR THE $K_L \to \pi^+\pi^-\pi^0\gamma$ DECAY

In this appendix we will describe the first measurement of the branching ratio of the $K_L \to \pi^+\pi^-\pi^0\gamma$ decay. The analysis is based on the same data used for the Dalitz measurement, where we used the MIP $K_L \to \pi^+\pi^-\pi^0$ sample as a normalization mode. We calculate the acceptance using the radiative corrections given by the PHOTOS [19] package in the Monte Carlo simulation.

The motivation for this measurement is a theoretical paper published in 1996 [7] which calculated the $K_L \to \pi^+\pi^-\pi^0\gamma$ branching ratio using Chiral Perturbation Theory. The measured form factors and branching ratio are in good agreement with this theoretical prediction. PHOTOS, on the other hand, predicts too few radiative events. This issue will be discussed in detail.

D.1 Data Selection

We applied mostly the same selection cuts to the $\pi^+\pi^-\pi^0$ and $\pi^+\pi^-\pi^0\gamma$ samples as applied in the Dalitz analysis. Those cuts that are different are listed in Table D.1. To identify $\pi^+\pi^-\pi^0\gamma$ events, we required an extra in-time cluster with a good shape and timing χ^2 and minimum energy of $E_{min} > 0.5$ GeV. We also required this cluster to be separated from the other reconstructed particles in the calorimeter, as well as the calorimeter edges. We have a total of 2586 events that passed all selection cuts.

Shape χ^2 for all γ clusters	< 20
Timing χ^2 for all γ clusters	< 5
Minimal extra cluster energy, lab	$E_{\gamma,min}^{lab} > 0.5$ GeV
Minimal extra cluster energy, CM	$E_{\gamma,min}^{CM} > 0.010$ GeV
Extra cluster/track separation	0.1m
Invariant mass of $\pi^+\pi^-\pi^0\gamma$	$0.49 < M_{\pi^+\pi^-\pi^0\,\gamma} < 0.502$
Invariant mass of $\pi^+\pi^-\pi^0$	$M_{\pi^+\pi^-\pi^0} < 0.495$ or $0.500 < M_{\pi^+\pi^-\pi^0}$

Table D.1: Special selection cuts for the radiative measurement.

D.2 Monte Carlo Simulation

The Monte Carlo simulation was based on KTEVMC version 5.04. We used the LPIMIP option to suppress simulation of pion showers instead of the standard procedure used in the Dalitz measurement.

To simulate radiative $K_L \to \pi^+\pi^-\pi^0\gamma$ events we used the PHOTOS [19] package. The latter includes the calculation of bremsstrahlung contribution in Leading Log Approximation. We used an infrared cutoff of 10 KeV. The Monte Carlo sample statistics is about ten times the data.

We used the $\pi^+\pi^-\pi^0$ Monte Carlo simulation for normalization and estimation of the background due to accidental clusters. In this normalization sample, the LPIMIP option was also used to avoid generation of pion showers.

D.2.1 PHOTOS reweighting

We found that the PHOTOS simulation predicts too few radiative events, as can be seen in Figure D.1. In this plot the normalization is given by the mass sideband in $K_L \to \pi^+\pi^-\pi^0$, which is used for background subtraction. As can be seen here, the data exceeds the PHOTOS prediction by approximately a factor of two (for $E_\gamma^{CM} > 0.01 GeV$).

Apart from the normalization problem, PHOTOS describes the data reasonably well, as shown by the distributions in Figure D.2. To correct for the normalization mismatch, the Monte Carlo simulation has been scaled to match the data.

D.3 Background Estimation

We select radiative events by requiring that the additional photon, together with the other particles in the event, form a good invariant mass for the originating kaon. The main background is given by accidental clusters, which increase the total invariant mass of the $\pi^+\pi^-\pi^0\gamma$ system by approximately their energy in the kaon center of mass frame, E_γ^{CM}. The extra cluster also leads to a p_t^2 imbalance. Given the excellent invariant mass resolution for $\pi^+\pi^-\pi^0$ events of the KTeV detector, it is easy to obtain a very clean $\pi^+\pi^-\pi^0\gamma$ sample at relatively low E_γ^{CM}.

We used non-radiative $\pi^+\pi^-\pi^0$ Monte Carlo simulation with accidental clusters from accidental overlays to estimate the background. We found that the timing χ^2 distribution is poorly reproduced while the energy of the extra cluster is sufficiently well described (see Figure D.3). Therefore we relaxed the timing χ^2 cut for the simulation and rely on the mass sideband for normalization.

Figure D.4 shows the invariant mass distribution for $\pi^+\pi^-\pi^0\gamma$ events, in bins of E_γ^{CM}. In this plot we relaxed the requirement that the $\pi^+\pi^-\pi^0$ invariant mass be outside a region around the kaon mass, i.e. $M_{\pi^+\pi^-\pi^0} < 0.495$ or $0.500 <$
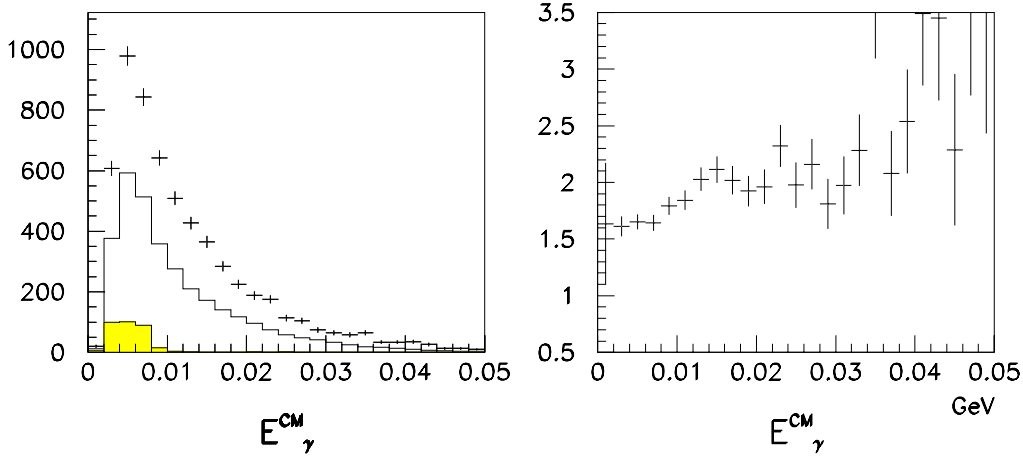
Figure D.1: Energy distribution of radiative photon in the center of mass. Left: center of mass energy distribution of the radiative photon for data (dots) background Monte Carlo simulation (shaded histogram) and sum of PHOTOS radiative Monte Carlo simulation and background (open histogram). The PHOTOS prediction is normalized using non-radiative events. Right: ratio of data to Monte Carlo simulation distributions.

$M_{\pi^+\pi^-\pi^0}$. One can see here that the background and signal separate very cleanly for $E_\gamma^{CM} > 0.01$ GeV.

D.4   Angular distribution of the radiated photon

We studied the angular distribution of the radiative photon with respect to the $\pi^+\pi^-$ direction, in the $\pi^+\pi^-$ center-of-mass frame. The photon is radiated by the $\pi^+\pi^-$ through bremsstrahlung, the direct emission part is known to be very small. For this reason one would expect the angular distribution to be very similar to the bremsstrahlung angular distribution for $K_S \rightarrow \pi^+\pi^-$, which is known exactly, and is given by:

$$Brems = \frac{1}{p_\gamma^2}x^2(1+x^2)\frac{sin^2\theta_\gamma^{+-}}{(1+x^2sin^2\theta_\gamma^{+-})^2} \tag{D.1}$$

where p_γ is the momentum of the radiative photon; x is proportional the momentum with which the charged pions are separating, i.e.:
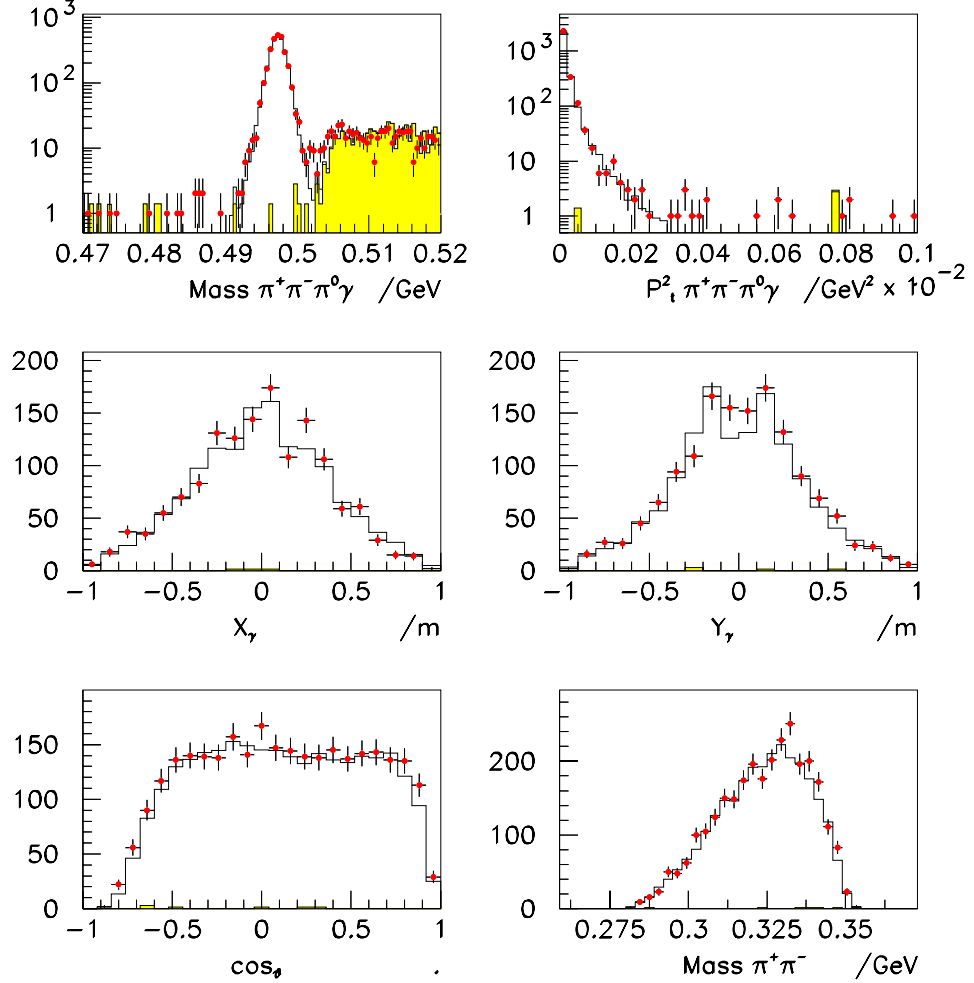
Figure D.2: Radiative sample control plots. Dots represent data, the shaded histogram represents background Monte Carlo simulation and the open histogram represents signal plus background Monte Carlo simulation. The background is normalized to the $\pi^+\pi^-\pi^0\gamma$ invariant mass side band, see section D.3. The signal Monte Carlo is scaled to match the data. From left to right, top to bottom the plots show invariant mass distribution of $\pi^+\pi^-\pi^0\gamma$ particles, total transverse momentum squared p_t^2, X and Y illumination of photons at the calorimeter, cosine of the photon angle with respect to the kaon direction in the kaon rest frame $\cos\theta$ and invariant mass distributions of charged pions.
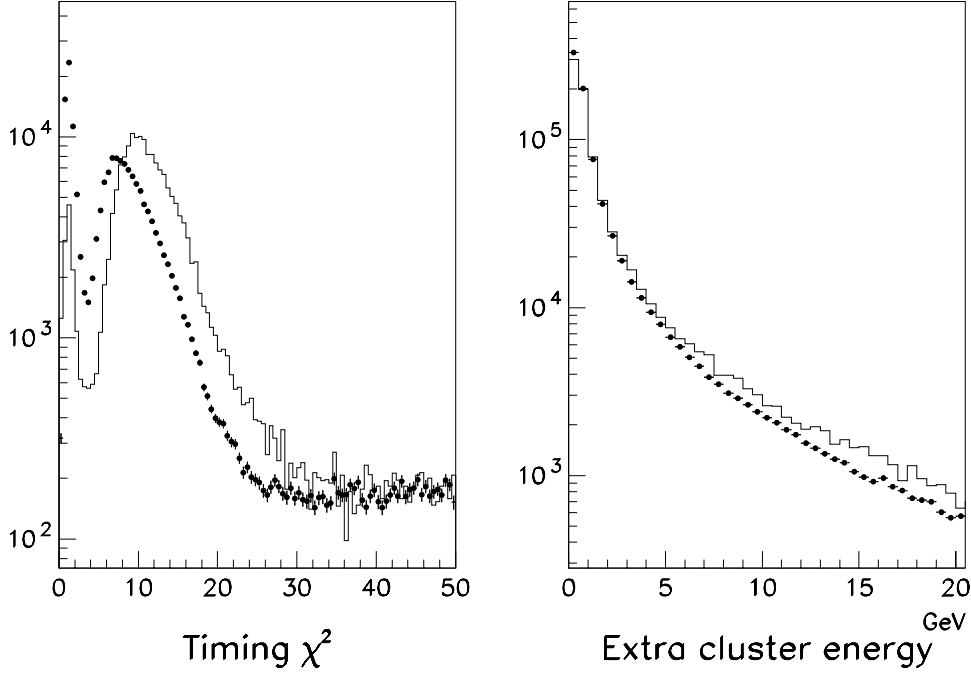
Figure D.3: Timing χ^2 and extra cluster energy distributions. Data (dots) and background Monte Carlo simulation (open histogram) distributions (left panel) and for the energy (right panel) of the extra cluster.

$$x = \frac{|\vec{p}_{\pi^+} - \vec{p}_{\pi^-}|}{2m_{\pi^+}};$$ (D.2)

and θ_γ^{+-} is the angle between the radiative photon and the $\pi^+\pi^-$ direction. The momentum of the radiative photon is not only a function of x but also depends on the momentum of the π^0.

Now, if we look at this formula we see that, for very small x, the distribution is very close to dipolar. This is what one would expect from the classical electromagnetic radiation of a dipole. However, for bigger values of x, the non-trivial part of the denominator starts to kick in, favoring photon emission along the direction of the outgoing pions. This is just a relativistic effect at high separation momentum and can be derived from the Feynman propagator itself. Figure D.5 shows the bremsstrahlung distribution fits to the data. We conclude that we understand the radiative photon and it's angular distribution.
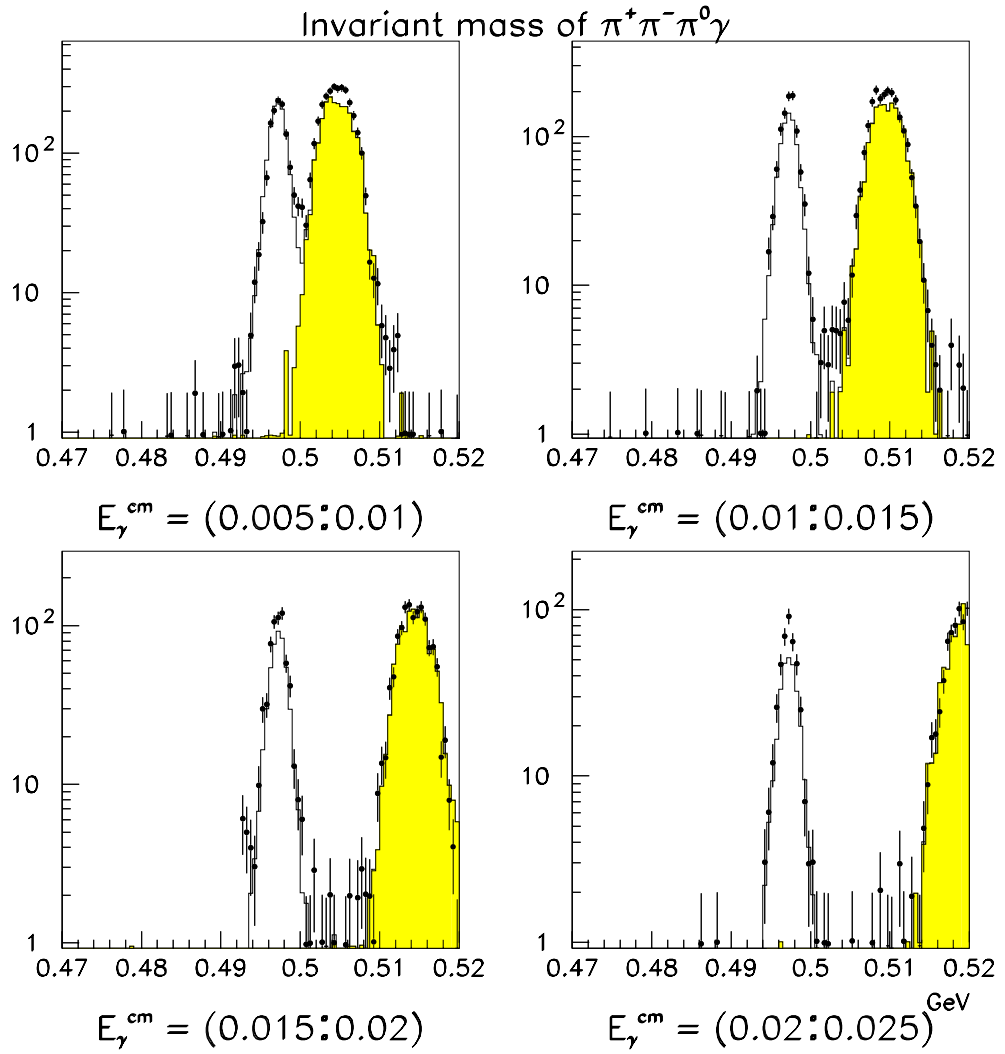
Figure D.4: Invariant mass distribution of $\pi^+\pi^-\pi^0\gamma$ as a function of photon energy E_γ^{CM}. Dots are data, open (gray) histogram shows Monte Carlo simulation of radiative (non-radiative) $\pi^+\pi^-\pi^0$ events. One can clearly see how the background cleanly separates for higher energy photons.
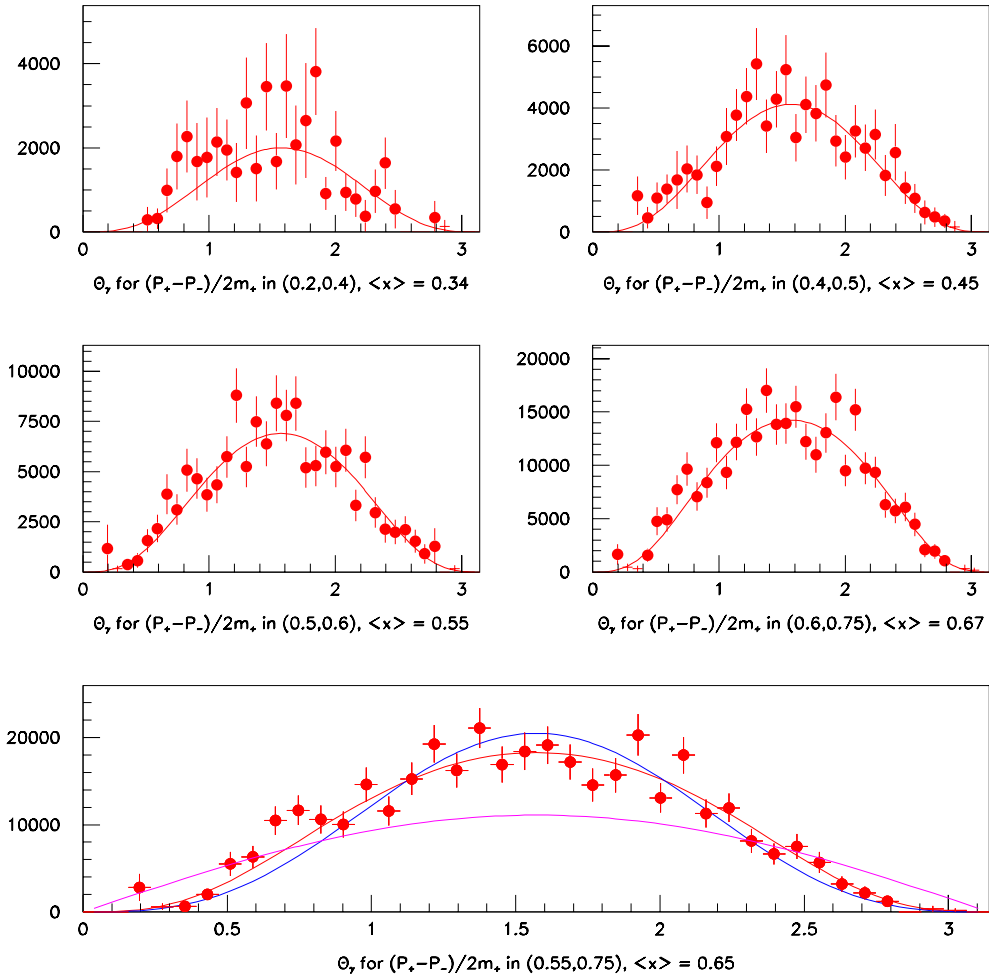
Figure D.5: Angular distribution of the radiative photon in the $\pi^+\pi^-$ center-of-mass frame. As can be seen in these plots, the theoretical bremsstrahlung distribution describes the process quite well. In particular, take a look at the last plot. The fits you see correspond, from top to bottom at $\theta_\gamma^{+-} = 0$, to: a pure dipole distribution ($sin^2(x)$, $\chi_\nu^2 = 2.2$); our bremsstrahlung function ($\chi_\nu^2 = 1.26$); and a homogeneous photon distribution ($\chi_\nu^2 = 10.7$). Note that the "fattening" that the bremsstrahlung distribution predicts for high separation momentum between the pions matches that of our data.

D.5 Form Factor Measurement

To measure the branching ration of $K \to \pi^+\pi^-\pi^0 \gamma$ decays we used the following equation:

$$Br\left(\pi^+\pi^-\pi^0 \gamma\right) = \frac{N(\pi^+\pi^-\pi^0 \gamma)}{N(\pi^+\pi^-\pi^0)} \times \frac{Acc_{\pi^+\pi^-\pi^0}}{Acc_{\pi^+\pi^-\pi^0 \gamma}} \times Br\left(\pi^+\pi^-\pi^0 \right), \qquad (D.3)$$

where $N(\pi^+\pi^-\pi^0 \gamma), N(\pi^+\pi^-\pi^0)$ are number of $\pi^+\pi^-\pi^0\gamma$ and $\pi^+\pi^-\pi^0$ events reconstructed, respectively; and $Acc_{\pi^+\pi^-\pi^0}$, $Acc_{\pi^+\pi^-\pi^0\gamma}$ are the respective acceptances for these modes, estimated using Monte Carlo simulation.

In general, given a simulation which describes the energy spectrum of the decaying kaons, E_K, the acceptance $Acc_{\pi^+\pi^-\pi^0}$ is a function of two Dalitz variables
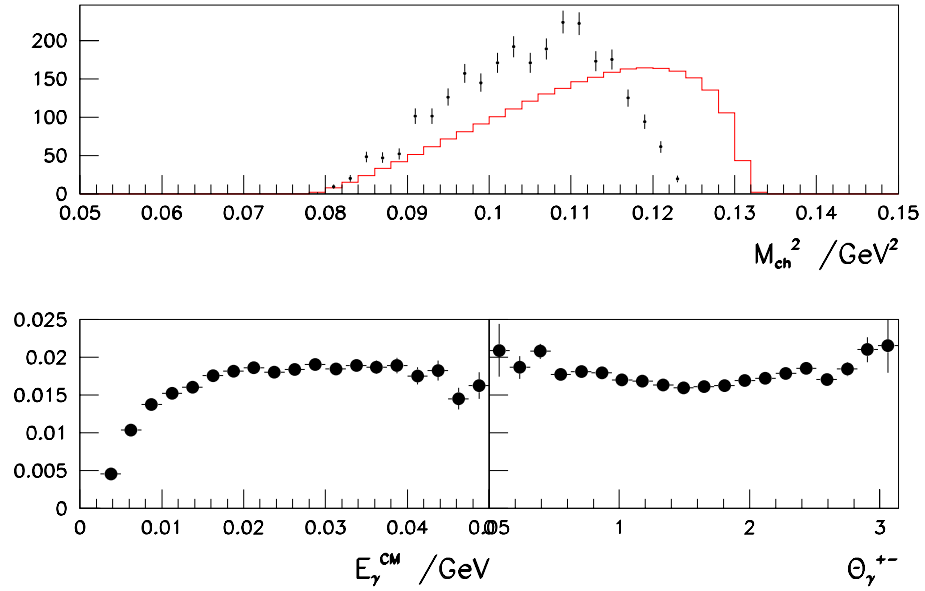

Figure D.6: Acceptance for radiative events. Top: invariant mass distribution of charged pions for radiative (dots, $E_\gamma^{CM} > 0.01$ GeV) and non-radiative (histogram) $\pi^+\pi^-\pi^0$ events (data). Bottom: Acceptance for reconstruction of $\pi^+\pi^-\pi^0\gamma$ events as a function of E_γ^{CM} and θ_γ^{+-}.

while $Acc_{\pi^+\pi^-\pi^0\gamma}$ depends on five kinematic variables. On the other hand, in the limit $E_\gamma^{CM} \to 0$, $Acc_{\pi^+\pi^-\pi^0\gamma}$ can be factorized as:

$$\lim_{E_\gamma^{cm} \to 0} Acc_{\pi^+\pi^-\pi^0\gamma} = Acc_{\pi^+\pi^-\pi^0} \times Acc_\gamma \tag{D.4}$$

where Acc_γ depends solely on the acceptance for reconstructing an extra photon in the KTeV detector. For finite E_γ^{CM} there are additional corrections, primarily due to the change in the charged pions' invariant mass distribution. This is illustrated in Figure D.6 (left) where the invariant mass distribution of charged pions for radiative and non-radiative $\pi^+\pi^-\pi^0$ events are compared. The change in shape is due to a different kinematic limit on M_{ch} imposed by the energy taken by the radiative photon.

Lets now concentrate on studying the radiative photon acceptance. The variables that are best suited for this study are the radiative photon's kinematic variables. We will use the energy of the photon in the kaon rest frame, E_γ^{CM}, and it's angle with respect to the $\pi^+\pi^-$ direction, θ_γ^{+-} (in the $\pi^+\pi^-$ center-of-mass frame). Figure D.6 shows the acceptance in these variables. As can be seen, the angular acceptance averages out quite nicely. There is no rescaling in these plots. We rely on the PHOTOS simulation for the other parameters that come into the acceptance calculation. We have cross-checked PHOTOS using overlays of photon illumination, photon direction in the kaon rest frame, and invariant mass distributions of charged pions, see Figure D.2. Given the statistics of the data sample, data and Monte Carlo simulation agree well.

As previously mentioned, there is a mismatch in the number of events generated by PHOTOS and those we see in data (see Figure D.1). There should be no bias in our calculations due to this mismatch, as both PHOTOS and reconstructed Monte Carlo would be affected equally. To verify that this is the case we reweighted our generated PHOTOS and the reconstructed Monte Carlo in E_γ^{CM} bins, obtaining a perfectly flat photon energy overlay between data and Monte Carlo. We have included this effect in our systematic error calculations.

Figure D.7 (left) shows the measured $\pi^+\pi^-\pi^0\gamma$ form factor. There's very good agreement between our measurement and the theoretical prediction [7]. The right plot shows data divided by the $O(p^2)$ QED prediction compared to the effect of the next to leading order corrections. The current data precision does not allow one to distinguish between the $O(p^2)$ and $O(p^4)$ calculations.

Combining the data from different E_γ^{CM} bands, we measure a branching ratio for the $K_L \to \pi^+\pi^-\pi^0\gamma$ decay of $1.35 \pm 0.03(stat)) \times 10^{-3} \times Br(K_L \to \pi^+\pi^-\pi^0)$ which agrees very well with the theoretical prediction.
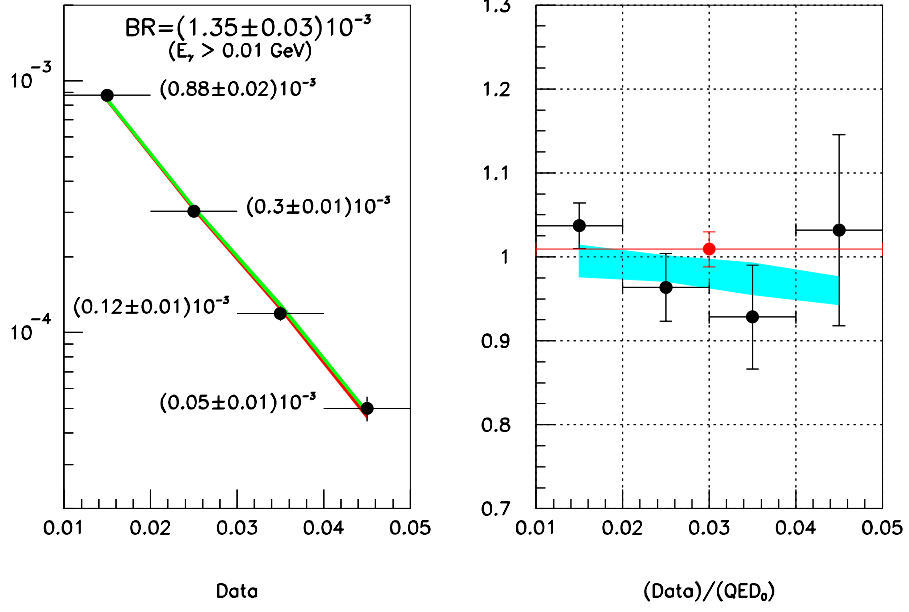
Figure D.7: Measurement of $\pi^+\pi^-\pi^0\ \gamma$ form factor. Left: relative branching ratio of $\pi^+\pi^-\pi^0\ \gamma$ to $\pi^+\pi^-\pi^0$. Data (dots) is compared to the QED calculation (solid band). Error bands correspond to statistical errors only. Right: data divided by $O(p^2)$ QED prediction. The solid band shows ratio of $O(p^4)$ to $O(p^2)$ QED predictions [7]. Notice that since the branching ratio decays exponentially, the value and error bands do not really belong in the middle of the bins. However, the theoretical values and error shown by the band are also bin-centered as they were calculated in the same bin sizes.

D.6   Systematic Uncertainty

The systematic uncertainties in the branching ratio of the $K_L \rightarrow \pi^+\pi^-\pi^0\gamma$ decay are due to imperfect cancellation of acceptances for radiative and non-radiative $\pi^+\pi^-\pi^0$ events [1]. Acc_γ does not cancel in the $E_\gamma^{CM} \rightarrow 0$ limit. Therefore we studied the uncertainties due to the photon energy scale, photon position reconstruction, minimum photon energy cut and photon identification cuts (shape and timing χ^2) in detail.

To estimate the photon energy scale uncertainty we used the invariant mass distribution of photon clusters from π^0 decays, see Figure D.8. We fitted the data

---

[1]In contrast with the Dalitz measurement, which depends on acceptance to first order
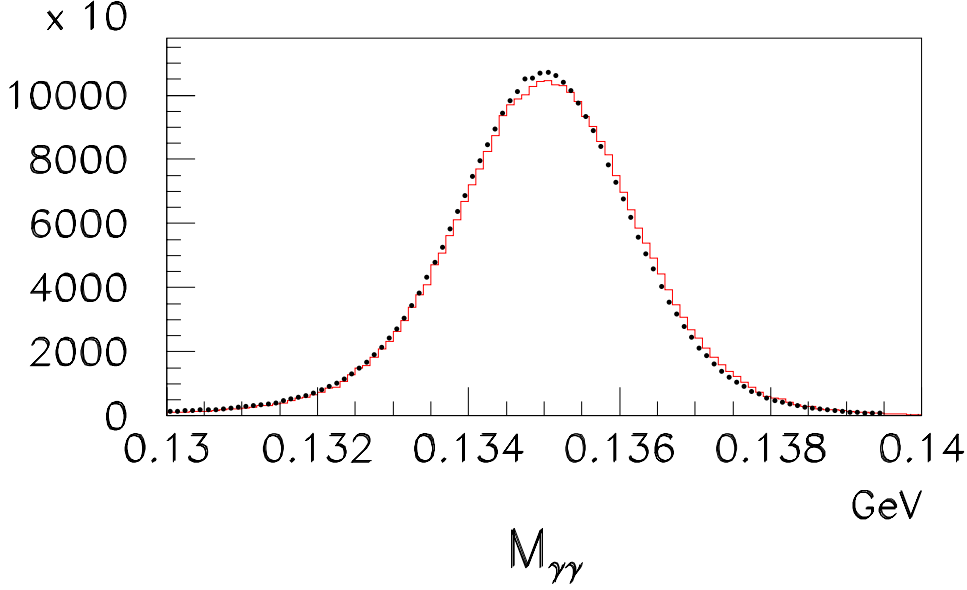
Figure D.8: Invariant mass distribution of two photons from the π^0 decay. Dots show the data, histogram corresponds to Monte Carlo simulation. Difference between peak position corresponds to energy scale mismatch of 0.03%.

and Monte Carlo distribution around the peak region and found an offset consistent with a 0.03% energy scale mismatch. To cover resolution and energy nonlinearity effects, we estimate the energy scale uncertainty to be bellow 0.1%. Such a variation of the scale changes the branching ratio by 0.08%.

To estimate the systematic uncertainty due to position reconstruction of the photon, we moved the cluster center of gravity by 2 mm in X and Y, and changed the size of the calorimeter by 1 mm, as limited by survey measurements. The variation of the branching ratio due to this distortions is 0.15%.

The effect of minimum photon energy cut, the nominal cut being at $E_\gamma > 0.5$ GeV, was studied by varying it in the $0.35 - 0.75$ GeV region. As a systematic error we assign the largest change in the branching ratio, which turns out to be 0.82%. This error also covers any possible inefficiency of the clustering algorithm.

We studied the efficiency of the shape and timing χ^2 requirements ("photon identification cuts") using photon clusters from π^0 decays. In the case of the nominal shape $\chi^2 < 20$ cut, the inefficiency never exceeds a 0.5% level. The timing χ^2 inefficiency is uniform in photon energy and is also about 0.5%. We found virtually

no inefficiency in the case of the default Monte Carlo simulation. We corrected the simulation for this efficiency difference. To check the validity of this efficiency estimation procedure, we lowered shape χ^2 cut down to 5. In that case we found about 94% efficiency for $E_\gamma < 1$ GeV for data, which should be compared to about 98% efficiency for Monte Carlo, giving a correction of about 4%. Yet, we found only a 0.45% change in the branching ratio due to this, so we assign this value as a systematic error in this case.

Figure D.9 shows the resulting $Br(\pi^+\pi^-\pi^0 \gamma)/Br(\pi^+\pi^-\pi^0)$ obtained from data for different run periods and also for data sets broken into approximate halves. One can see that the result fluctuates in accordance with statistical errors. The
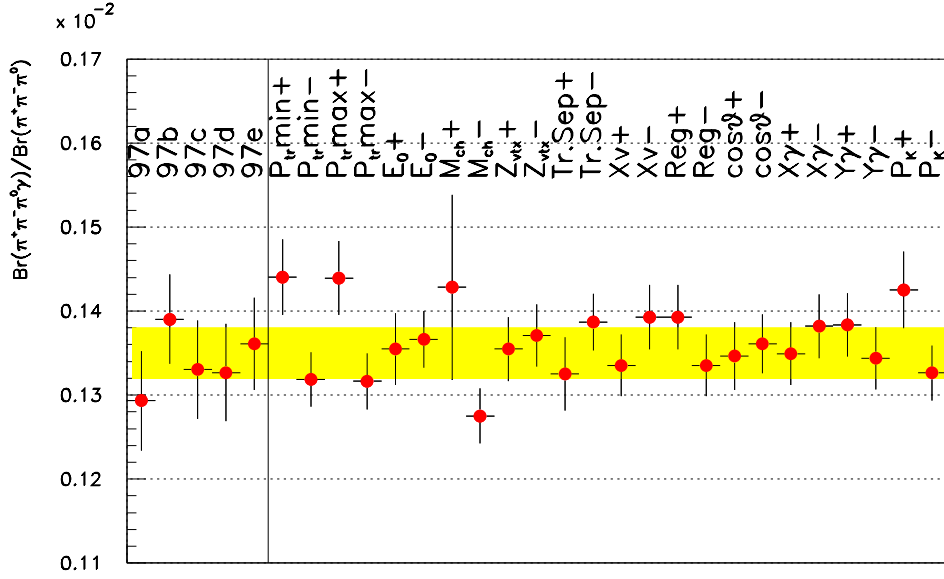

Figure D.9: Half-sample studies. Variation of $Br(\pi^+\pi^-\pi^0 \gamma, E_\gamma^{CM} > 10 \text{ MeV})/Br(\pi^+\pi^-\pi^0)$ for data broken into different subsamples. The shaded band shows the nominal result with it's statistical uncertainty. The first five points show results for five different run periods. The remaining points represent results for data broken in approximate halves for: maximum of the charged pion momentum, minimum of the charged pion momentum, π^0 energy, invariant mass of charged pions, vertex Z position, track separation, vertex X position, regenerator position, cos of the photon direction in the kaon rest frame, X and Y photon position at CsI, kaon momentum.

$\chi^2/(n.d.f - 1)$ for half-studies is 19/23. We assigned a systematic error of 1.0%, based on difference between the RMS of the distribution for all 24 tests compared to one expected from statistical error.

Next comes the systematic error due to acceptance calculations. We observe slopes in data and Mote Carlo simulations in $\pi^+\pi^-\pi^0$ events for variables such as: kaon energy; Z-position of the vertex; and charged invariant mass. To correct for these discrepancies, one can reweight the $\pi^+\pi^-\pi^0$ Monte Carlo distributions. Using these reweighting slopes, we calculated their effect on $Br(\pi^+\pi^-\pi^0\gamma)/Br(\pi^+\pi^-\pi^0)$ (independently), and we observe a total systematic bias of 0.4%. As for systematics in the $\pi^+\pi^-\pi^0\gamma$ acceptance, we studied the fluctuations introduced by binning in both θ_γ^{+-} and E_γ^{CM} and by reweighting the E_γ^{CM} distribution, obtaining a total systematic uncertainty of 0.45%.

We also studied dependence of the branching ratio calculation on the Dalitz parameters of the $K_L \to \pi^+\pi^-\pi^0$ decay by changing them in the Monte Carlo simulation. We used two sets of Dalitz parameters for this study: the new PDG-2000 values [8] and those obtained in the main Dalitz analysis. The change in the branching ratio in these cases is bound by 0.15%.

Finally, to estimate the uncertainty due to background, we compared the branching ratio calculation with and without background subtraction. Due to the very low background level, the result changes only by 0.15%.

To estimate total systematic uncertainty we added contributions from all different sources in quadrature. The overall systematic uncertainty comes out to be 1.64%.

The systematic uncertainties for each for the form factors where determined in the same manner. We are not including those results in this appendix.

D.7   Conclusion

We performed a first measurement of branching ratio for the process $K_L \to \pi^+\pi^-\pi^0\ \gamma$. We found that

$$Br(K_L \to \pi^+\pi^-\pi^0\ \gamma, E_\gamma > 10\ MeV) = \\ (1.35 \pm 0.03(stat) \pm 0.02(syst)) \times 10^{-3} \times Br(K_L \to \pi^+\pi^-\pi^0\ ) \tag{D.5}$$

or, in terms of absolute branching ratio:

$$Br(K_L \to \pi^+\pi^-\pi^0\ \gamma, E_\gamma > 10\ MeV) = \\ (1.66 \pm 0.03(stat) \pm 0.03(syst) \pm 0.03(norm)) \times 10^{-4} \tag{D.6}$$

which is in a good agreement with standard model calculation [7]:

$$Br_{theor}(K_L \to \pi^+\pi^-\pi^0\ \gamma, E_\gamma > 10\ MeV) = (1.65 \pm 0.03) \times 10^{-4} \tag{D.7}$$

Photon energy scale ($\Delta E/E \sim 0.001$)	0.08%
Photon position reconstruction ($\Delta R/R \sim 0.001$)	0.15%
Minimal photon energy cut ($0.35 - 0.75$ GeV)	0.82%
Photon identification cuts	0.45%
Acceptance calculation	0.41%
"Half"-sample study	1.0%
Kaon energy reweighting	0.4%
Z vertex reweighting	0.002%
$M_{\pi^+\pi^-}$ reweighting	0.6%
PHOTOS γ energy reweighting	0.45%
Dalitz parameter change	0.15%
Background subtraction	0.15%
Total	1.64%

Table D.2: Systematic uncertainties for the radiative branching ratio measurement.

E_γ^{CM} (MeV)	Statistical	Systematic
10-20	2.5%	1.8%
20-30	4%	1.9%
30-40	6.7%	2.5%
40-50	10%	6.7%
10-50	2%	1.64%

Table D.3: Statistical and systematic uncertainties for the radiative form factors.

APPENDIX E
POST-COMPLETION: MIP DISCREPANCY RESOLVED

This appendix was added after the completion of the thesis.

We have found the reason for the discrepancy in the Dalitz parameters determined from the samples with and without a MIP cut. Figure 7.8 shows a substantial discrepancy between these two determinations, particularly in the g Dalitz parameter.

When reconstructing events, a separation of at least 25 cm is required between the photon clusters and the tracks at the calorimeter. The extra $\gamma\gamma$ pair cut did not require this for the extra cluster. A showering pion can create a slew of extra clusters around the track position at the calorimeter. Since the MIP sample did not have big charged pion clusters, it was not affected by this cut noticeably.

To resolve this problem, we require that the extra photon clusters considered for the extra pair cut be separated by at least 25 cm from the charged tracks at the calorimeter. With this additional requirement, both results agree perfectly, and the systematic is somewhat reduced. Figure E.1 shows the systematic studies with the correct extra pair cut. Figure E.2 shows the result of the parameters, as compared to the other measurements.

The fitted Dalitz parameters are now

$$
\begin{aligned}
g &= 0.7070 \pm 0.0023\ (stat) + 0.0034\ (syst) - 0.0050\ (syst) &= 0.7070 \pm 0.0055 \\
h &= 0.0966 \pm 0.0034\ (stat) + 0.0043\ (syst) - 0.0030\ (syst) &= 0.0966 \pm 0.0055 \\
k &= 0.0217 \pm 0.0011\ (stat) + 0.0004\ (syst) - 0.0024\ (syst) &= 0.0217 \pm 0.0027
\end{aligned}
\tag{E.1}
$$
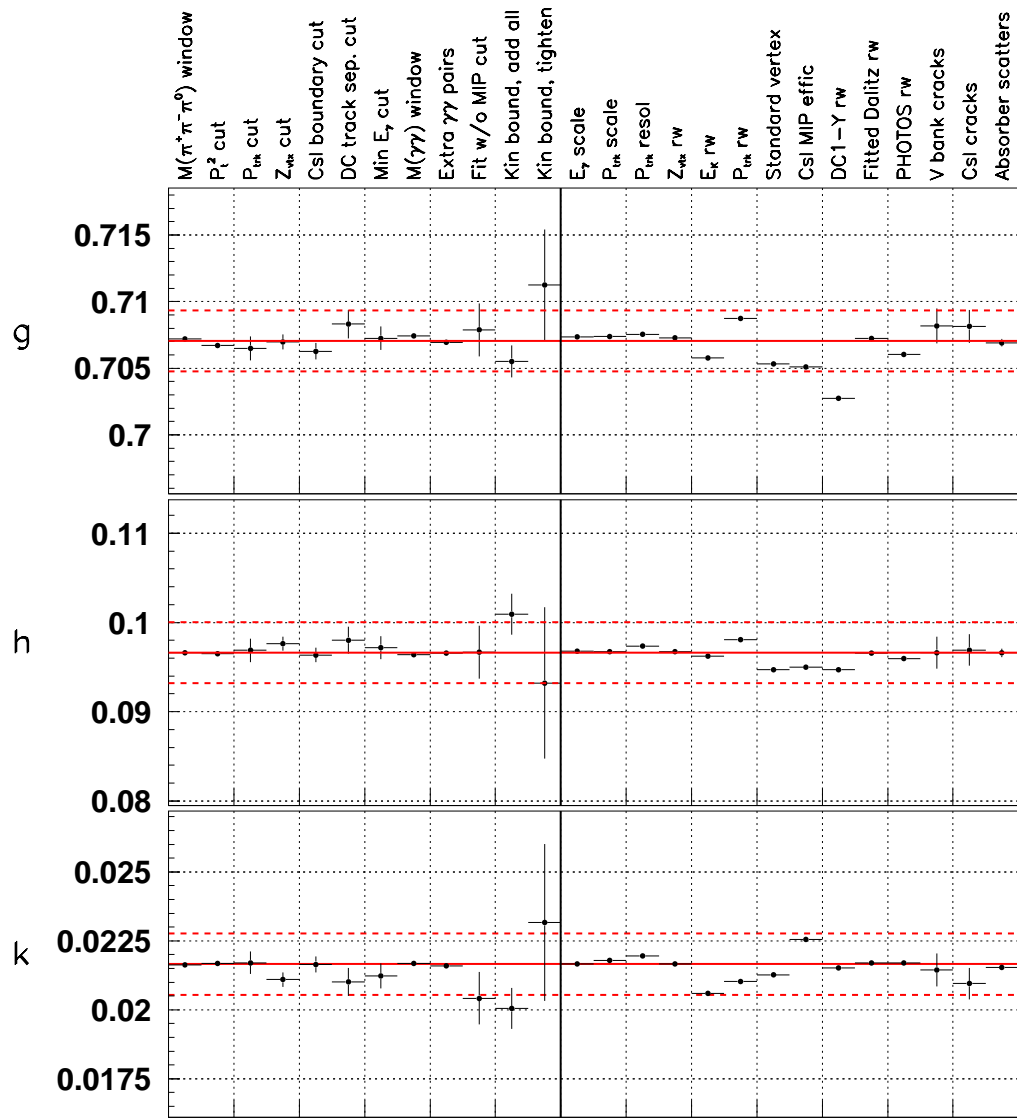
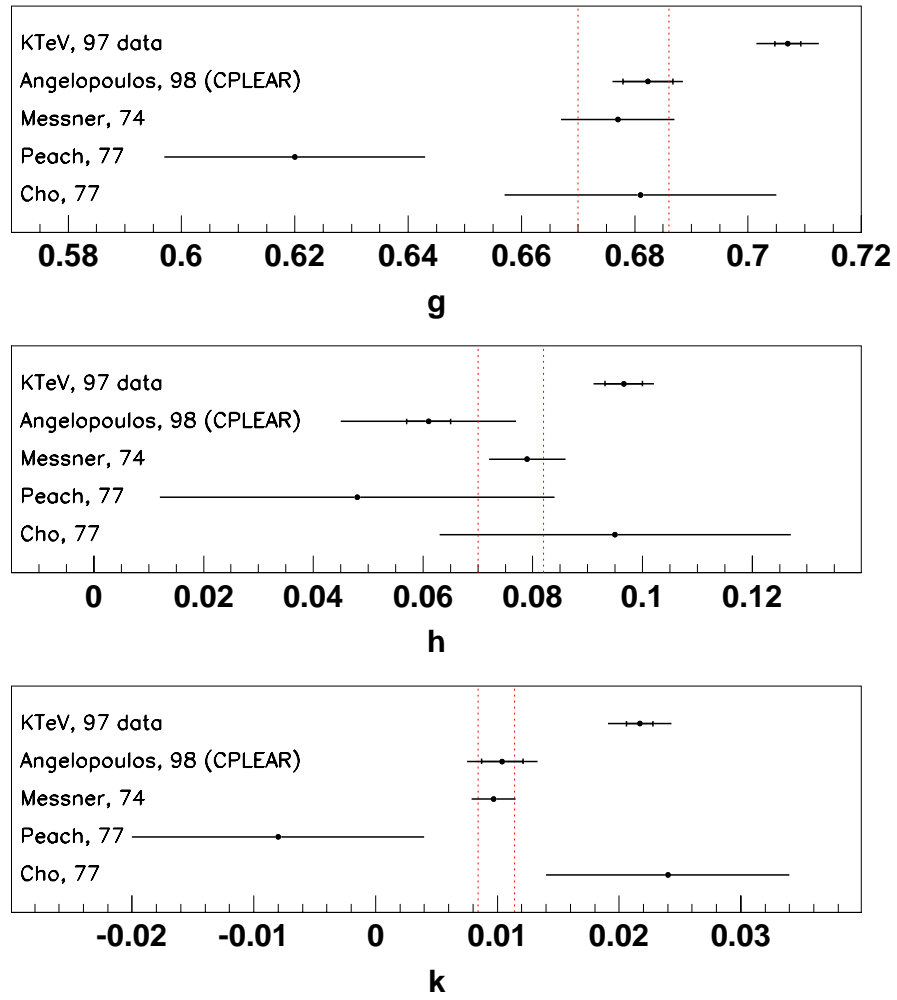Figure E.1: Systematic tests. The MIP discrepancy has been fixed, compare to Figure 9.1.

Figure E.2: History of $K_L \to \pi^+\pi^-\pi^0$ Dalitz parameter measurements. The MIP discrepancy has been fixed, compare to Figure 9.1.

REFERENCES

[1] M. Gell-Mann and A. Pais, *Phys. Rev.* **97**, 1387 (1955).

[2] S. Weinberg, 1960.

[3] D. Luers et al. , *Phys. Rev.* **133B**, 1276 (1964).

[4] C. Zemach, 1964.

[5] A. A. Belkov et al. , hep-ph/9311295, 1993.

[6] G. D'Ambrosio et al. , and ibid. D **51** , 3975(E) (1995), 1994.

[7] G. D'Ambrosio et al. , 1997.

[8] D.E. Groom et al. , *Eur. Phys. Jour.* **C15**, 1+ (2000).

[9] Y. Cho et al. , *Phys. Rev.* **D15**, 587 (1977).

[10] R. Messner et al. , *Phys. Rev. Lett.* **33**, 1458 (1974).

[11] K.J. Peach et al. , *Nucl. Phys.* **B127**, 399 (1977).

[12] A. Angelopoulos et al. , *Eur. Phys. Jour.* **C3**, 389 (1998).

[13] K. Arisaka *et al.*, *KTeV Design Report*, Technical Report FN-580, Fermilab, 1992.

[14] V. Bocean *et al.*, "KTeV Beam Systems Design Report", Technical Report TM-2023, Fermilab, 1997.

[15] T. Kobilarcik, "Results of Stability Study for the KTeV Beam", Technical Report TM-2037, Fermilab, 1997.

[16] J. Whitmore, *Nucl. Instrum. Methods Phys. Res., Sect. A* **409**, 687 (1998).

[17] E. D. Zimmerman, Ph.D. thesis (The University of Chicago, March, 1999).

[18] R. A. Briere, Ph.D. thesis (The University of Chicago, June, 1995).

[19] E. Barberio and Z. Was, 1994.

[20] A. J. Malensek, 1981. Fermilab Reports FN-341, FN-341A (errata).

[21] H. W. Atherton *et al.*, 1980. CERN preprint 80:07.

134

[22] Particle Data Group, L. Montanet *et al.*, *Phys. Rev. D* **50**, 1173 (1994).

[23] J. A. Graham, A threshold-based model for the high-sod effect in ktevmc, Technical Report KTEV-0765, KTeV internal, 1997.

[24] R. Brun *et al.*, 1994. computer code GEANT 3.21, CERN, Geneva.

[25] Particle Data Group , *Phys. Lett. B* **239**, 1 (1990).

[26] S. V. Somalwar et al. , *Phys. Rev. Lett.* **68**, 2580 (1992).

[27] A. Lai *et al.* Measurement of the quadratic slope parameter in the k(l) -¿ 3pi0 decay dalitz plot. *Phys. Lett.*, B515:261, 2001.

[28] J. Kambor et al. , 1991.

[29] J. H. Christenson, J. W. Cronin, V. L. Fitch, and R. Turlay, *Phys. Rev. Lett.* **13**, 138 (1964).